UNIVERSITY OF LIVERPOOL

UNIVERSITY OF LIVERPOOL

DOCTORAL THESIS

Addressing Uncertainty in Earthquake Magnitudes Commonly Used in Modern Seismic Hazard Assessment

Thesis submitted in accordance with the requirements of the University of Liverpool for the degree of Doctor of Philosophy

by

James Holt

September 2019

Declaration of Authorship

I declare this thesis titled, "***Addressing Uncertainty in Earthquake Magnitudes Commonly Used in Modern Seismic Hazard Assessment***" and the work presented in it are my own work. The material contained in the thesis has not been presented, either wholly or in part, for any other degree or qualification.

Signed: _____

James Holt

20th September 2019

Table of Contents

Abstract

Earthquake magnitudes are central to seismic hazard assessment filtering in as one of the primary characteristics of earthquakes to which we can develop spatio-temporal relationships as well as scaling relationships. As such it is critical to constrain earthquake magnitudes and report accurate uncertainty and find strategies to reduce it. To that end, we explore methods to either report accurate uncertainty or directly improve magnitude determination by using high quality seismic data from three regions (Utah, USA, Yellowstone National Park, USA and Continental Japan).

Our first study is focussed on Utah, USA in cooperation with the University of Utah Seismograph stations (UUSS). Here we develop the capability to estimate the moment magnitude (M_W), commonly used in modern seismic hazard assessment (SHA) studies, applying a spectral method (Edwards et al., 2010) to small and moderate-sized earthquakes. Using our improved methodology, we produce a new M_W catalogue containing > 200 M_W estimates ($1.5 < M_W < 4.0$). Furthermore, with our expanded M_W dataset for the Utah region we find bilinear relationships for M_W as a function of both M_L and coda-duration magnitude (M_C), thus providing an improvement to those derived previously for the region (Arabasz et al., 2016). The slope of the M_L - M_W relationship is 2/3 for $M_L < 3$, consistent with theory and other similar experimental studies.

Our second study, also ran in cooperation with UUSS, is directed toward reducing uncertainty in local magnitude (M_L) calculation, for earthquakes recorded in Yellowstone National Park, USA. A non-parametric inversion (Savage and Anderson, 1995) is used to derive a new distance correction for Yellowstone, along with a new set of station corrections. We find Yellowstone has a unique and complex local attenuation structure. Additionally, the new calculated M_L, using our new distance correction and station corrections, provides improved agreement with the moment magnitude (M_W) estimates ($3.1 < M_W < 4.5$) than the previous scale. Furthermore, we find evidence that the old station corrections traded off with the old distance correction (Richter, 1958).

In our final study we explore the role of scenario-dependent site amplification on local magnitude (M_L) on a single-station basis. In order to isolate the effect of the near-surface amplification on M_L, relative differences between station-specific M_L at the surface and borehole ($\Delta M_{L,STN}$) are studied for 34 sites from the KiK-Net network, Japan. We find strong moment magnitude (**M**) dependent, scenario specific, $\Delta M_{L,STN}$ trends. To further our understanding, we developed stochastic models to simulate the response and understand this variability. Simulated data, $\Delta M_{L,STN}(\mathbf{M})$, based on the available site response information are shown to closely match the empirical $\Delta M_{L,STN}$ trends. We conclude by recommending how these models may be used as station corrections to reduce uncertainty and bias in the determination of M_L.

List of Figures

Chapter 1: Introduction

Chapter 2: Moment Magnitude Calculation of Small to Moderate-Size Earthquakes in Utah

Chapter 3: A New Local Magnitude Scale for Yellowstone National Park, USA

Chapter 4: Scenario-Dependent Site Effects for the Determination of Unbiased Local Magnitude

Appendix A

Appendix B

Appendix C

List of Tables

List of Abbreviations

1D-SHTF - 1D Shear-Wave (horizontal) Transfer Function
AGU - American Geophysical Union
ANSS - Advanced National Seismic System
BH - Broadband and High Gain (SEED convention)
BSSA - Bulletin of the Seismological Society of America
EIDA - European Integrated Data Archive
FAS - Fourier Amplitude Spectrum of Acceleration
G-R - Gutenberg-Richter
GMPE - Ground Motion Prediction Equation
H - Hinge Point
H/V - Horizontal-to-Vertical Ratio
HB87 - Hutton and Boore (1987)
HH - High Broadband and High Gain (SEED convention)
IASPEI - International Association of Seismology and Physics of the Earth's Interior
IRIS - Incorporated Research Institutions for Seismology
ISB - Intermountain Seismic Belt
LPSP - Long Period Spectral Plateau
MT - Moment Tensor
NGA - Next Generation of Ground-Motion Attenuation Models
NIED - National Research Institute for Earth Science and Disaster Resilience
ORFEUS - Observatories & Research Facilities for European Seismology
PDF - Probability Density Function
PSHA - Probabilistic Seismic Hazard Analysis
QWL - Quarter Wavelength Amplification
R58 - Richter (1958)
RMSE - Root Mean Square Error
S/B - Surface-to-Borehole Ratio
SED - Swiss Seismological Service
SHA - Seismic Hazard Assessment
SLU - Saint Louis University
SSA - Seismological Society of America
UGS - Utah Geological Survey
USGS - United States Geological Survey
UUSS - University of Utah Seismograph Stations
WA - Wood-Anderson
WGUEP - Working Group on Utah Earthquake Probabilities
WOR - Weighted Orthogonal Regression
WUS - Western United States
WY - Yellowstone Network (SEED convention)
YS - Yellowstone
YVO - Yellowstone Volcano Observatory

Acknowledgements

So here we are, 4 years, 2 continents and 1 marriage later. It is absolutely incredible to think about how long this journey has been and what has happened in the meantime. This PhD, however, has been a constant in my life… that is, a constant rollercoaster. I'm writing this mainly to serve as a reminder to myself, if I look back on this in the future, that the pay-off will come. Just stick with it, whatever you are doing and remember what you did to get here.

To my wife, I just want to thank you from the bottom of my heart for being there for me no matter what. Especially as we both know … I can … SOMETIMES … be a teeny tiny bit grumpy (probably why we were made for each other). But when I felt like things weren't ever going my way, you were there to steer me in the right direction and even if it took me a while to listen, I always did in the end (happy wife happy life). Thank you for being there for me during a difficult transition. Moving away from home is a bit like being born new again, it takes time (and patience) to re-learn what you think you should already know. I couldn't have done this without you by my side when I needed you the most. You didn't just provide me moral support, but hours and hours of discussion and ideas and the late, late nights and far too early mornings. Helping me with GMT and the catalogues and inversion theory and the list goes on and on. And all of those things when you were busier than I was. You are truly an exceptional human and I am proud to call you my wife. One thing is certain, without you this thesis would not be anywhere close to the same, and it is all the better for it. Now we just need to get you your PhD and publish our first Holt and Holt paper.

To my family, thank you for always believing in me and what I was doing. There are so many times you encouraged me to keep pushing and keep on going. Your faith never wavered in me and I wouldn't be here without you. I think all of you knew I would get here, and I was probably the only one who didn't. I know I always lived up to your expectations and that's because I know you would've support me no matter what. You wouldn't let me leave because I needed to live up to my own expectations. I guess you know me better than I know myself, go figure!

Now onto my Liverpool chapter;

Firstly, to Ben I thank you for putting up with my crazy sudden life transitions. I don't think either of us could have predicted how this PhD would have ended up, but you met with me and listened to me waffle on about it all regardless. I thank you for giving me the support to get me going in my career and giving me a solid foundation to allow me to grow as a researcher.

To Silvio, I can thank you for just about every decision I ever made during my undergrad which lead me to this point. You encouraged me to do a PhD because you

saw potential in me that I never knew was there. Our weekly meetings and hours of discussion about b-values (yeah right) and all of your advice. I honestly do not think I would have ever even thought about doing this without you. You gave me that final push to apply when others tried to persuade me against it. My life simply would not be the same, so I thank you for being a great lecturer, role model and friend at such a critical part of my career and personal development. But also, thank you for being there during my PhD too, especially when I fell on really hard times. I haven't forgotten and I owe you many a beer.

To all of my friends in the department, Anthony L, Paul, Becky, Julia, John, Mike, Joe^2 (G&A), Tom, Christina, Amy, Simon, Oliver, Minxuan, Antoine, Beth, Elliot, Suraya, Lidong, Pablo, Yael, Louise, Josh, Jenny and Michael;

Stephan – for being the big (and tall) brother I never had, you knew I was a crazy person but were still my friend through it all. Congratulations on your successful PhD viva, Dr. Toby.

Sergio – we had our differences, but you were my big (and less tall) brother from a whole other continent. One day I will learn Spanish, but for now I will eat all the completos I can, because they're damn delicious.

Anthony, Caroline, Megan, Tom C and Olly – You've been there through it all, undergrad PhD and beyond. We spent so many fun nights together with the gang and my experience wouldn't have been the same without you. We were the best of friends even though we would wind each other up something wicked! I have had the pleasure to watch you all grow as people and into adults (with real jobs – what?!) over the past few years and it brings me great joy. I hope we remain close friends forever.

If I have missed anyone, it was not intentional. I wrote this a few hours before I submitted…

Finally, onto my Utah chapter:

I can't thank everyone at the UUSS enough, to Keith, Jim, Relu for listening me ramble on and on about science, every week and never getting bored. Thank you for taking me in as one of your own students and for all of your mentorship, guidance and support. You didn't have to do this, but you did it anyway. I have been able to become the seismologist I always wanted to be. You have taught me SO MUCH and right when I needed you most. Certainly, without your support I would not have been able to do this.

Chapter 1: Introduction

Techniques used in modern seismic hazard assessment (SHA) are progressing at an ever-increasing rate. For example, Douglas and Edwards (2016) explain that the number and complexity of Ground Motion Prediction Equations (GMPEs) alone have increased exponentially, likely owing to an explosion of available data (e.g. NGA project, OFEUS - EIDA to name just a few), open source software and rapid advancements of computational power to process big data. As advancements are made it is becoming more and more critical to constrain earthquake magnitudes and report accurate uncertainty. In this thesis we work with commonly used earthquake magnitude scales, discuss where they are most important and address areas of uncertainty as well as derive uncertainty which may be used in future hazard assessments.

1.1 Aims and Objectives

With this work we aim to improve current magnitude-related seismic hazard products by developing novel approaches to quantify uncertainty and attempt to move it to manageable epistemic uncertainty where possible. Our broader aims can be summarised as the following:

a1. Discuss potential sources of uncertainty in magnitudes commonly used in SHA

a2. Quantify and report uncertainty on our scientific outputs to improve magnitude-related products used for SHA

a3. Develop strategies to directly address sources of error introduced by, potentially, inaccurate assumptions used to calculate earthquake magnitudes commonly used in SHA

1.2 Foreword

In the current chapter, I first address some basic concepts and discuss how earthquake magnitudes are important to SHA to add further context to this work. To enhance our understanding, I have adapted some figures from scientific work published in journals by the Seismological Society of America (SSA) and American Geophysical Union

(AGU). All adapted figures have been reproduced in full compliance with guidelines provided by each publisher[1] and the appropriate references are specified in figure captions. Chapters 2 through 4 are modified from and are in the format of peer-reviewed journal papers. Therefore, it was necessary to include some repetition of basic concepts so each chapter can be read independently. Chapters 2 through 4 each have a preface that briefly explain some background. Each then has individual abstract, introduction, methods, results, discussion and conclusion sections. Finally, in Chapter 5 we provide an executive summary of findings, how each chapter fits within the larger scope of the thesis, and how they address the goals and objectives.

[1] SSA - https://www.seismosoc.org/publications/permissions/ (last accessed 16/09/19) and AGU - https://publications.agu.org/author-resource-center/usage-permissions/ (last accessed 16/09/19).

1.3 Local Magnitude

Earthquake magnitude provides a simple yet intuitive measure of the relative sizes of earthquakes. The most ubiquitous scale was dubbed local magnitude (M_L), sometimes referred to as the 'Richter Scale'. The M_L scale (Richter, 1935) is given by:

$$M_L = \log_{10} A - \log_{10} A_0 \,, \tag{1.1}$$

where A is the zero-to-peak (or half peak-to-peak) maximum horizontal displacement[2] in millimetres (mm) as measured on a Wood-Anderson (WA) torsion seismometer and $-\log_{10}(A_0)$ is a reference correction term that accounts for the combined effects of geometric and anelastic attenuation. The WA torsion seismometer became popular around 1925 after Anderson and Wood (1925) published information about the instrument in the Bulletin of the Seismological Society of America (BSSA). It was quickly adopted in California (Uhrhammer and Collins, 1990) as the de facto seismometer of choice for many years. Some WA instruments were even operational until the 1990's, roughly when broadband seismometers became more common. Therefore, WA seismometers were central to Richter's M_L scale because they recorded most of the Californian seismic data available at the time. The standard WA instrument

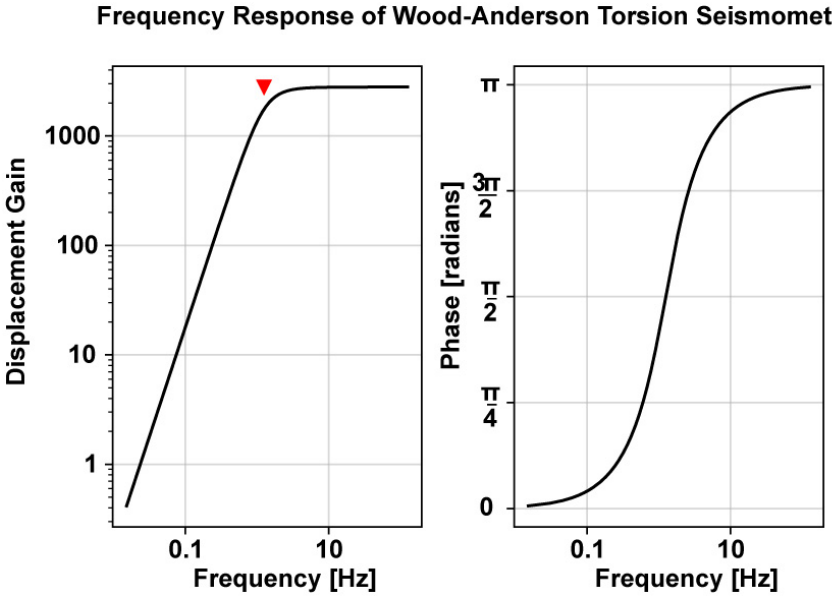

Figure 1.1 – Amplitude (left) and phase (right) response of a Wood-Anderson Torsion Seismometer (Wood-Anderson, 1925). The red inverted triangle marks the location of the corner frequency at f = 1.25 Hz, gain = 2800.

[2] WA seismometers only had NS, EW components.

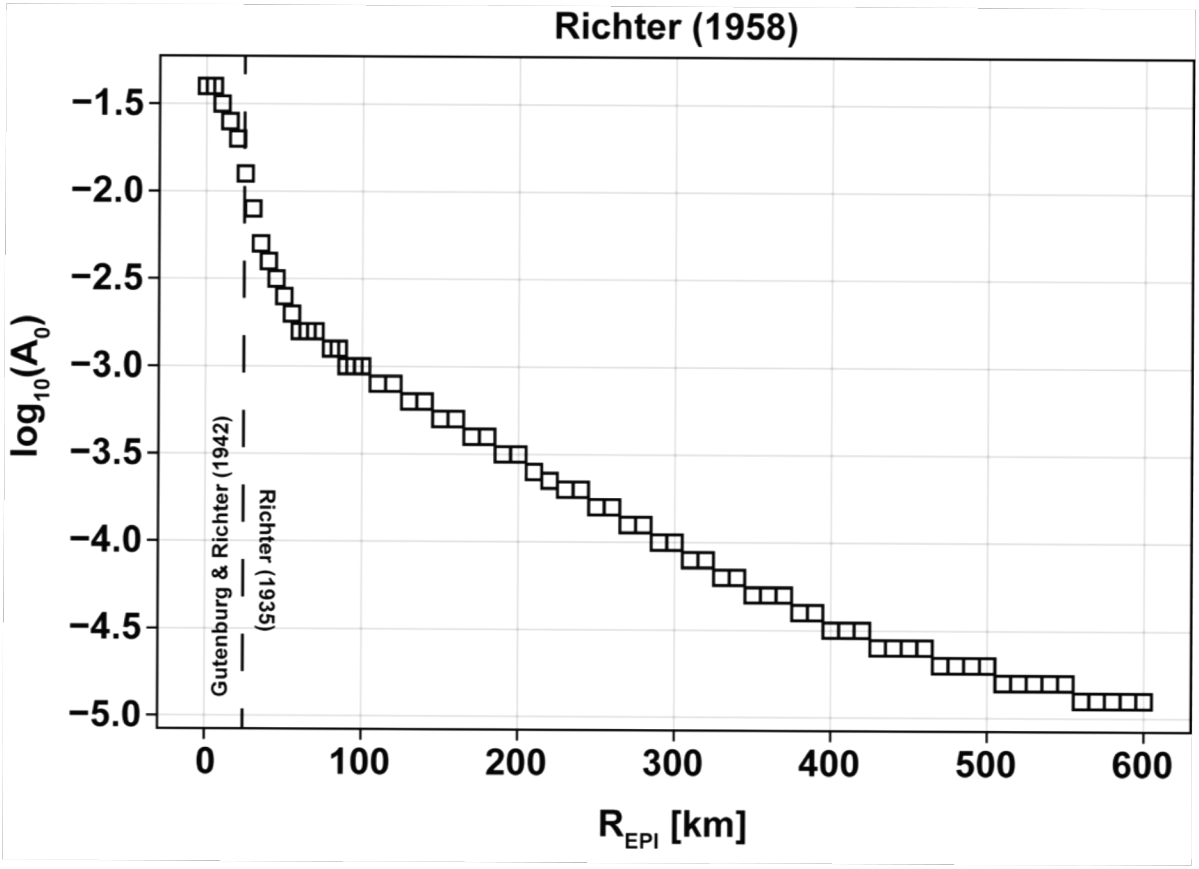

Figure 1.2 – Richter (1958) inferred attenuation correction. The dashed line represents the limit of Richter (1935) ($R_{EPI} > 30$) and Gutenberg and Richter (1942) ($R_{EPI} < 30$).

is a short-period seismometer with static magnification (V) = 2800[3], free period (T_0) = 0.8 s and critical damping (ζ) = 0.8. The response of the WA seismometer behaves similar to a high pass filter with corner frequency (f_c) ~ 1.25 Hz (Figure 1.1). The response of the WA causes the M_L scale to saturate at M_L ~ 6 to 7. This is because long-period seismic energy is dominant in large earthquakes (related to the increase in duration with increasing magnitude) which is diminished by the WA response (Shearer, 2009). Also, as earthquakes increase in size the radiated S-waves become less representative of the whole slip, owing to finite fault effects. S-waves radiate from (what can be approximated as) many small sub-faults over the entire rupture, making the relationship between *A* and source size complex. Today, the WA response is simulated via convolution of the theoretical standard WA response with instrument-

[3] Urhammer and Collins (1990) suggest that the magnification of the instrument (V) should be 2080 and not 2800 as was originally thought. Alsaker et al. (1991) found differences on the order of ~ 0.17 magnitude units when they adopted the change for synthesis of WA records.

corrected broadband records (Kanamori and Jennings, 1978; Uhrhammer and Collins, 1990).

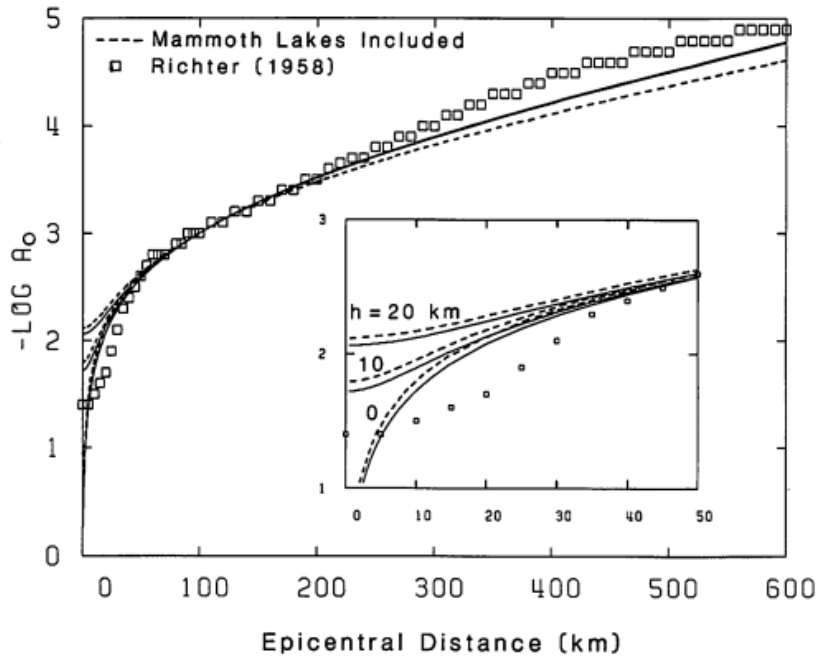

Figure 1.3- The figure compares the Richter (1958) attenuation curve with Hutton and Boore (1987). In inset figure shows a close up of the difference between the curves near-field. Modified from Hutton and Boore, The ML scale in Southern California, Bulletin of the Seismological Society of America [BSSA], 77(6), p2074-2094, 1987, doi: N/A, © Seismological Society of America.

M_L is determined by taking the difference between $\log_{10}(A)$ and $\log_{10}(A_0)$ as a function of distance for a single station estimate, or (more commonly) a 'network' average over two or more stations (Hutton and Boore, 1987). Richter provided the original reference curve for California, $-\log_{10}(A_0)$, as a function of epicentral distance (R_{EPI}) in his well-known 1935 publication and subsequent 1958 publication (Figure 1.2) (Richter, 1935, 1958). The scale was conditioned such that a peak WA displacement of 1 mm at 100 km, would give an M_L of 3. Gutenberg and Richter (1942) attempted to calculate $-\log_{10}(A_0)$ for near-field measurements (R_{EPI} < 30 km) where data was extremely limited. This was included in the attenuation table published in Richter (1958)[4]. Hutton and Boore, (1987) re-evaluated the attenuation correction with a simple parametric model (Figure 1.3) and noted that local magnitude scales designed

[4] This is the table generally used by seismic networks that either adopted the Richter scale or (more commonly) anchored a new attenuation correction (e.g. Bakun and Joyner,1984; Hutton and Boore, 1987).

for other regions should anchor their scale at $-\log_{10}(A_0) = 2$ at 17 km rather than at $-\log_{10}(A_0) = 3$ at 100 km. Their reasoning is twofold: (i) to allow more freedom to match regional attenuation at longer propagation distances and (ii) because they suggest that Richter (1958) incorrectly assumed a $1/R^2$ ($R_{EPI} < 30$ km) geometric spreading and their average focal depth was too deep. However, Pechmann et al. (2007) argued that Richter (1958) mentions no assumption about geometric spreading; adding that it was justified empirically and, no matter the case, much faster than 1/R geometric spreading at close proximity to the source is not unreasonable (e.g. Frankel et al., 1990). Furthermore, Alsaker et al. (1991) found that using the Hutton and Boore (1987) anchor introduced an apparent difference of attenuation in the Norwegian attenuation correction. They recommended that the anchor should be chosen with care and ensure it reflects observed attenuation of the desired region, at an appropriate distance range. They chose to anchor their scale at 60 km where Hutton and Boore (1987) and Richter (1958) agreed and where they had sufficient data to make that judgement. Thus far, only a handful of networks have adopted Hutton and Boore's suggested anchor (e.g. Langston et al., 1998; Keir et al., 2006), which is likely due to most networks around the time of the study lacking sufficient near-field data at 17 km to justify using it.

Although Hutton and Boore (1987) attempted to address near-field attenuation, studies have shown that ΔM_L values measured between stations within 10 km of the event tend to be > 0 on average, suggesting the reference attenuation correction is invalid for $0 < R < 10$ km (e.g. Kradolfer, 1984; Edwards et al., 2015; Butcher et al., 2017). To address this, Luckett et al. (2018) modified their local magnitude equation to include an additional near-source term, which they derived empirically. Luckett et al. (2018) suggested that this behaviour might be because Sg energy in close proximity to the source (< 10 km) is not the largest arrival, therefore the peak WA amplitudes are not Sg. In general, attenuation corrections derived for M_L are technically only valid for Sg attenuation, so this is a viable reason for the discrepancy. Regardless, most networks simply ignore near-field measurements entirely, citing that the seismic radiation field is more complex. This does, however, limit the sensitivity of the network for small magnitude events ($M_L < 2$) where measurements at $R_{EPI} > 10$ to 20 km are often overshadowed by noise (Edwards et al., 2015).

Principally, an M_L scale provides a simple empirical relation for measured ground displacement, such that 'clouds' of data[5] may be averaged to calculate M_L (Boore, 1989). The International Association of Seismology and Physics of the Earth's Interior (IASPEI) recommend independently treating each horizontal component at any particular station as separate datum for the calculation (Bormann and Dewey, 2012), but some networks take an average between NS and EW displacement at any point in the trace (e.g. Pechmann et al., 2007). Implicitly, the M_L equation given by Equation 1.1 assumes that scatter within the cloud is aleatory. However, this is not case because M_L may be influenced by repeatable site effects. Richter (1958) acknowledged this and revised Equation 1.1 to include station corrections (S):

$$M_L = \log_{10} A - \log_{10} A_0 + S \tag{1.2}$$

The station correction term attempts to account for systematic and repeatable bias introduced on a per-station (or instrument) basis, broadly caused by local geological factors, such as site amplification (Havskov and Ottemöller, 2010). One can invert for S, along with the attenuation correction and M_L values of the events, by solving a linear system of equations in the form **d** = **Gm** (e.g. Savage and Anderson, 1995; Bindi et al., 2005; Miao and Langston, 2007; Illsley-Kemp et al., 2017). Dominantly, two main methodologies for regional M_L calibration have been adopted. The first (and most common) is the 'parametric model' e.g. Bakun and Joyner (1984) or Hutton and Boore (1987) (Figure 1.3) and the general equation to be minimised is given by Equation 1.3[6]:

$$\log_{10} A_{i,j} = -n\log_{10}\left(\frac{r_{i,j}}{R_{REF}}\right) - K\left(r_{i,j} - R_{REF}\right) - M_{L,REF} + M_{L,i} - S_j \tag{1.3}$$

$$-\log_{10} A_0 = -n\log_{10}\left(\frac{r_{i,j}}{R_{REF}}\right) - K\left(r_{i,j} - R_{REF}\right) + M_{L,REF} \tag{1.4}$$

[5]Recorded over multiple stations sufficiently separated by distance and in azimuth from the earthquake epicentre / hypocentre to average out irregular radiation effects (Richter, 1958).

[6] IASPEI recommend using n=1.11, K=0.00189, $M_{L,REF}$= 2.09 and r = hypocentral distance for areas suspected to have similar attenuation to Southern California (Bormann and Dewey, 2012). $M_{L,REF}$ was changed to 2.09 from 3 to account for V = 2080 (see footnote 3).

where $A_{i,j}$ are the WA amplitudes for earthquake i recorded at station j, $r_{i,j}$ is the source to station distance[7], $M_{L,i}$ is the magnitude and S_j is the station correction. Finally, $M_{L,REF}$ / R_{REF} is the reference magnitude / distance (3 and 100 km), respectively, and n / K are model coefficients to be determined (related to geometric spreading and anelastic attenuation). Together the coefficients define the attenuation correction as shown in Equation 1.4. Since the model given by Equation 1.4 has a well-defined and smooth functional form, it can be determined with few measurements at a cost of model complexity (Langston et al., 1998).

It is possible to include extra complexity to the parametric model and this was shown by Bindi et al. (2019). They traded $-\mathrm{n}\log_{10}\left(\frac{r_{i,j}}{R_{REF}}\right)$ with a piecewise linear model (e.g. Atkinson and Merau, 1992) with three linear segments and two breakpoints. Additionally, they added complexity to the $K\left(r_{i,j} - R_{REF}\right)$ term in a similar fashion, allowing for additional freedom at larger distances. The piecewise model facilitates capturing a more complex regional attenuation than is afforded by Equation 1.4. However, to help constrain the model, $M_{L,i}$ was not a free parameter. Bindi et al. (2019) used the second method for regional M_L calibration, the 'non-parametric model', to calculate $M_{L,i}$ and constrain the parametric inversion. The non-parametric model (Savage and Anderson, 1995) is described by Equation 1.5:

$$\log_{10} A_{i,j} = -a_n \log_{10} A_0 - a_{n+1} \log_{10} A_0 + b_i M_{L,i} - c_j S_j \tag{1.5}$$

$$a_n = \frac{R_n - r_{i,j}}{R_{n+1} - R_n} \tag{1.6}$$

Here, a_n is a coefficient of linear interpolation to node n at distance R_n and $a_{n+1} = 1 - a_n$. Finally, b_i and c_j are dummy variables that are equal to 1 or 0 depending on if the event - station pair exists or does not exist. The linear system is then solved subject to the constraints of $-\log_{10} A_0\,(R_{REF}) = \log_{10} A_{REF} - M_{L,REF}$ (where A_{REF}

[7] Can be any distance measure but usually epicentral distance or hypocentral distance.

is some reference WA displacement[8]) and $\sum_j S_j = 0$. The main strength of this method is that there is no assumed functional form of the attenuation correction. Instead, it is solved at each nodal point by linear interpolation from data. The model can therefore accommodate arbitrarily complex attenuation (i.e. significant variations in attenuation with distance; e.g. Lolli et al., 2015). Furthermore, providing constraints means that the inverted attenuation model is distinct from the station corrections and magnitudes. The pitfall of the technique comes with significant added computational cost because minimum dimensions of the problem in matrix format are $i * j * n \times i + j + n$ for the **G** matrix and $i * j * n$ for the **d** matrix. The computational cost quickly increases with more nodal points (which are required to better resolve the attenuation function), increased station coverage and/or a large number of earthquakes. Moreover, with the method as it stands interpretation of the underlying physical phenomenon is limited as geometrical spreading and anelastic attenuation are not separated.

1.4 Moment Magnitude

We begin by defining some terminology which will be used throughout this section for clarity. Moment magnitude represented by M_W (Kanamori, 1977) is exclusively referenced here only where seismic moment (M_0) is derived from moment tensor solutions, or from the long period spectral displacement level. We use **M** to generally represent moment magnitude where M_0 is derived via other methods e.g. scaling relationships. It is distinct from M_W in its applicability across a broad range of moment magnitudes since **M** was derived by combining the equations for surface-wave magnitude (M_S), M_L and M_W (Hanks and Kanamori, 1979)[9]. **M** is then given by Equation 1.7 (Hanks and Kanamori, 1979)[10]:

$$\mathbf{M} = \frac{2}{3}\log_{10}(M_0) - 6.03 \tag{1.7}$$

$$M_0 = \mu S \bar{d} \tag{1.8}$$

---

[8] Usually $-\log_{10} A_0(100\ km) = 3$ or $-\log_{10} A_0(17\ km) = 2$.

[9] This is explicitly stated because there is debate about how one should represent moment magnitude and I, the author, believe that **M** should be generally used to represent moment magnitude over the broad range of methods that estimate M_0 and M_W where a physical model is used. This sentiment is inferred from Hanks and Kanamori (1979) and Hanks and Boore (1984).

[10] In this paper the equation assumes M_0 is in dyne cm. Here, I give the equivalent relation in SI units of Newton meters (N·m) where 1 N·m = 1×10^7 dyne·cm

where M_0 (Equation 1.8) is given in SI units (N·m) and is a measure of the radiation of seismic energy caused by deformation at the source. Seismic moment is then expressed in terms of the shear modulus (μ, Pa), total rupture area (S, m^2) and the average displacement / slip ($\bar{d}$, m) along the fault plane. Although **M** is technically just a representation of M_0 (which is directly related to source properties of the earthquake), **M** is generally used in place of M_0 because it is a more convenient and natural scale (Kanamori, 1983). There are two principle benefits of **M**; the first is that it is directly linked to physical source properties through M_0, which means it can be inferred also

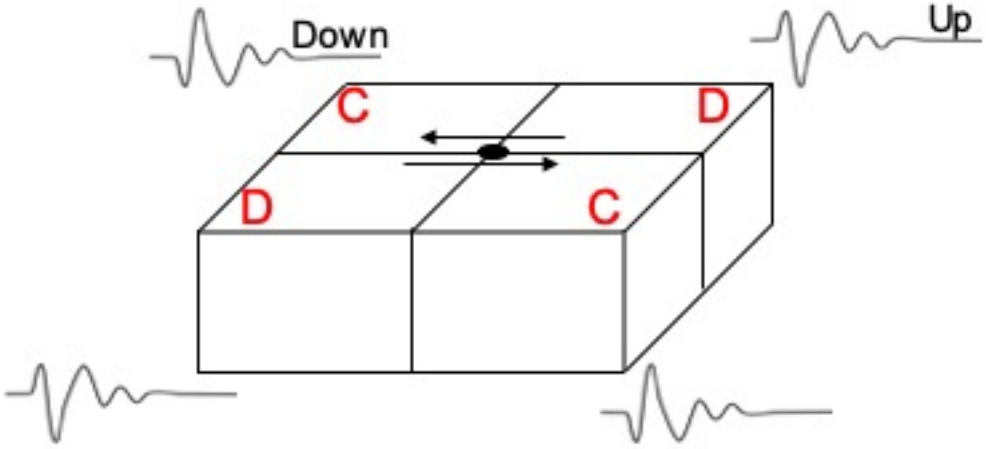

Figure 1.4 – Simple representation of a rupturing fault split into four quadrants, C represents a compressional quadrant and D represents a dilatational quadrant. The fault is left-lateral, and the black circle is the centroid projected to the surface. Two waveforms have been labelled Up or Down depending on if the first motion is downward or upward from the center line.

for historical seismicity from estimated rupture sizes. The second is that, unlike other magnitude ordinates, it does not saturate (Kanamori, 1977). It is for that reason it is used as a base of comparison for other magnitude scales and is generally desirable. Since determination of M_0 depend on physics-based models (rather than simple empirical relations; Kanamori, 1983) they can be difficult to obtain. A number of strategies have been developed, the most universal being M_0 estimation via moment tensor solutions. However, to understand moment tensors in the context of an

earthquake, it is useful to first understand the basic mechanisms of faulting and how seismic waves propagate from the source.

Figure 1.4 is a simple representation of a rupturing fault. It shows that the polarity of seismic waves that propagate from the fault depend on the force experienced in any given quadrant centred about the epicentre of the earthquake, separated by the 'nodal' planes. If there are enough records, it is possible to plot where the P- wave polarities are 'up' or 'down' on a focal sphere to determine the approximate orientation of the nodal planes – these are known as focal mechanisms (e.g. Johnson and Molnar, 1972) (Figure 1.5).

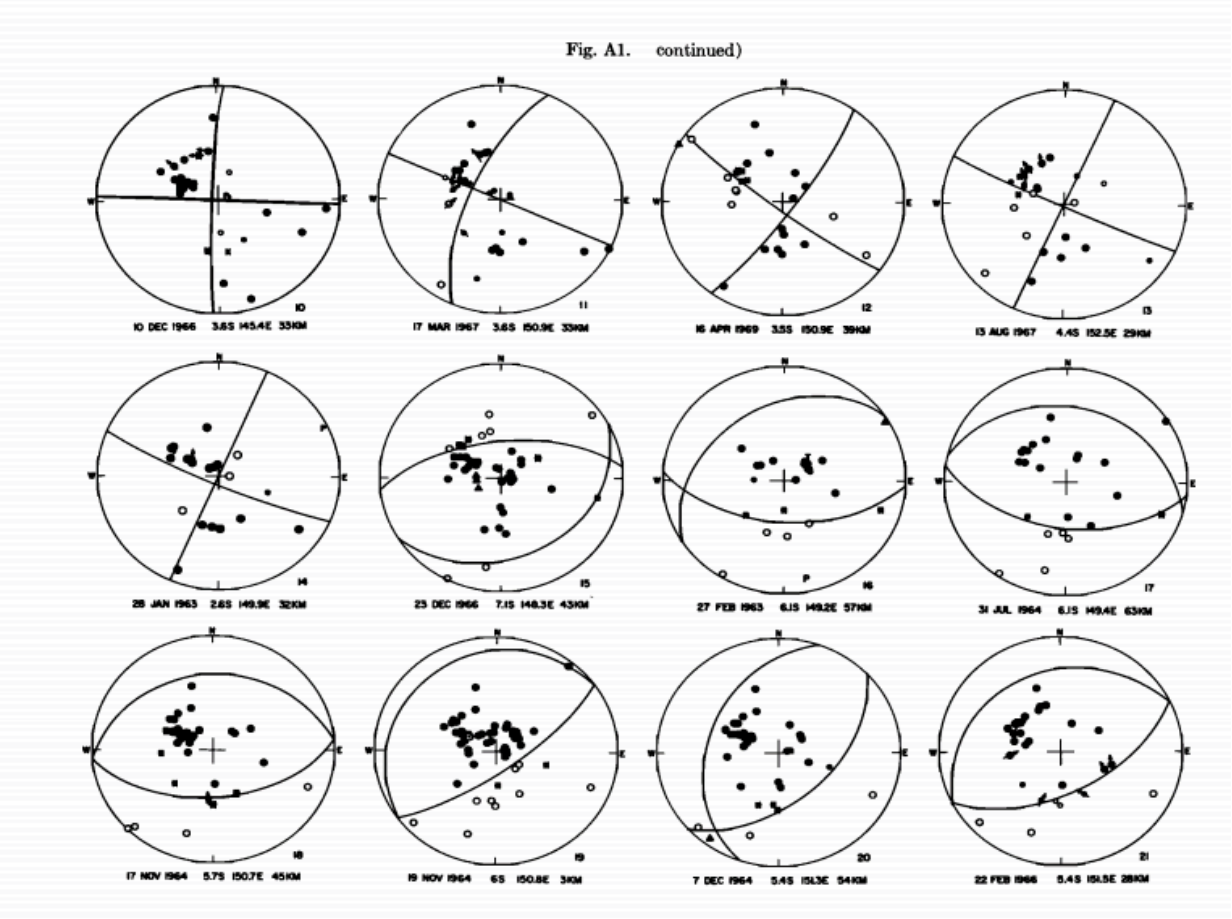

Figure 1.5 – A selection of focal mechanisms (aka beachball plots) (modified from Fig A1, Johnson and Molnar, 1972, Focal mechanisms and plate tectonics of the southwest Pacific, Journal of Geophysical Research [JGR], Volume 77, Issue 66, p5000-5032, https://doi.org/10.1029/JB077i026p05000, © American Geophysical Union) for earthquakes in the Pacific Ocean. The compressional ('up') motions are represented by solid circles and the empty circles represent the dilatational ('down') motions. Focal mechanisms usually are colour coded, compressional quadrants are coloured black and dilatational quadrants are white.

The focal mechanism is an incomplete summary of the forces at the seismic source. It is possible to more completely model earthquake source mechanisms using moment tensors (Gilbert, 1970). Moment tensors represent the forces at a seismic source (assuming a point-source definition) in terms of equal and opposite force couples (scaled by M_0). It is a 3 x 3 symmetric tensor (MT, Stein and Wysession, 2003):

$$MT = \begin{pmatrix} M_{xx} & M_{xy} & M_{xz} \\ M_{yx} & M_{yy} & M_{yz} \\ M_{zx} & M_{zy} & M_{zz} \end{pmatrix} \tag{1.9}$$

where the diagonal elements represent linear vector dipoles and the off-diagonal elements represent the force couples (Dahm and Krüger, 2014) (see Figure 1.6 for a diagram of all force couples). The shearing motion of an earthquake is often described as a 'double-couple', meaning forces are equal and opposite with no net torque (Eyre and Van Der Baan, 2015), Take for example, Equation 1.10 (Stein and Wysession, 2003):

$$MT = M_0 \begin{pmatrix} 0 & 1 & 0 \\ 1 & 0 & 0 \\ 0 & 0 & 0 \end{pmatrix} \tag{1.10}$$

This is the moment tensor representation of a pure left-lateral strike-slip (vertical dip) fault oriented in the same coordinate system (displacement in y plane) as Equation 1.9, and M_0 is the scalar seismic moment. M_0 may then be obtained from the MT via decomposition[11].

[11] I do not provide an in-depth review of this topic since it is extensive and beyond the scope of this thesis. I simply provide context as to how M_0 is related to a moment tensor for a shear faulting earthquake. For a comprehensive and in-depth review of moment tensors I recommend the following texts (Jost and Herrmann, 1989; Stein and Wysession, 2003; Udías et al., 2014).

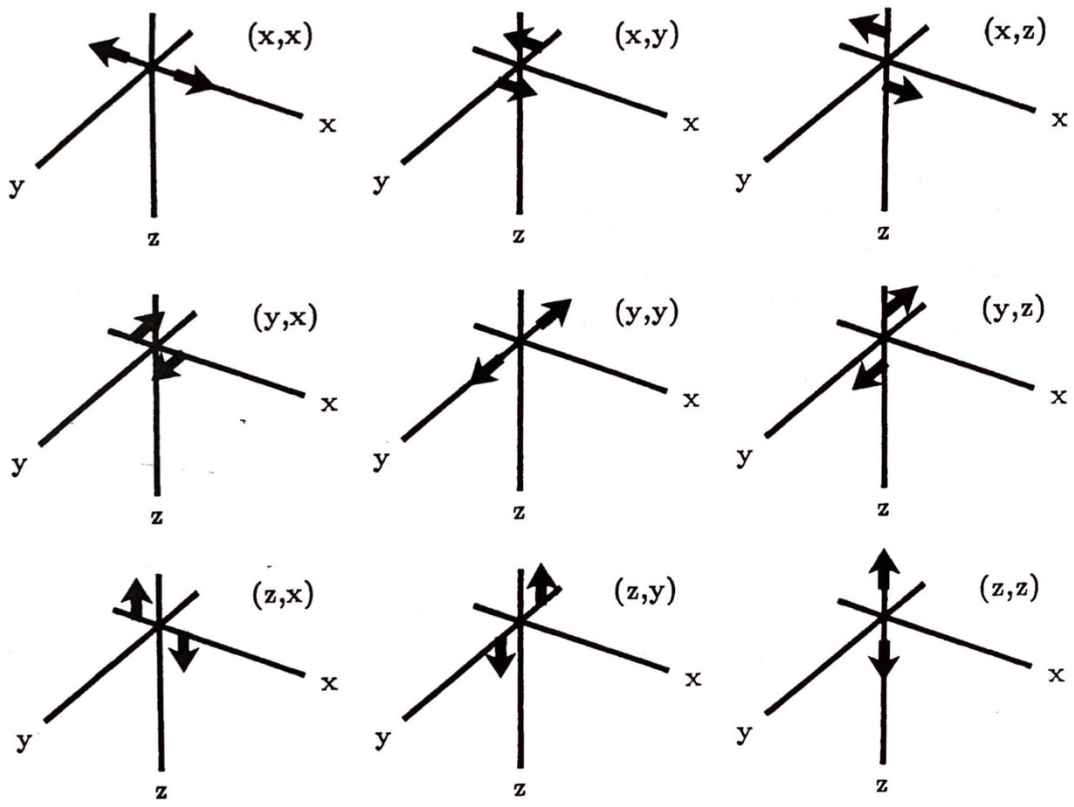

Figure 1.6 – Illustration of a set of orthogonal force couples that make up a moment tensor in 3D space for an arbitrary point source (modified from Fig.2, Jost and Herrmann, A Student's Guide to and Review of Moment Tensors, Seismological Research Letters [SRL], Volume 60, No.2, p37-57, 1989, https://doi.org/10.1785/gssrl.60.2.37, © Seismological Society of America).

For real earthquakes the moment tensor may be related to a seismic record by Equation 1.11:

$$u(t)_i = \sum_{j=1}^{6} G(t)_{ij} m_j \tag{1.11}$$

Here, u(t) is the recorded ground displacement over time (t), $G(t)_{ij}$ is the Green's function (representing the contribution of the path between the source and site) of seismogram, *i*, for moment tensor component (*j*) for 6 independent components (Stein and Wysession, 2003). It is then possible to invert for m_j (and by proxy M_0) via inversion by formulating a linear system of equations from Equation 1.11 often referred to time-domain moment tensor inversion.

While time-domain moment tensor inversion is commonplace in most seismic networks, it has some practical limitations. Most importantly, moment tensor inversions depend on the generation of synthetic Green's functions and their resolvability is very sensitive to the accuracy of the available earth model (Dahm and Krüger, 2014). Typically, this leads to filtering the seismogram to low frequencies for which the synthetic Green's functions are appropriate, due to the relatively coarse structure of the assumed earth model (Křížová et al., 2013). Generally, this limitation means that only earthquakes that have strong signal-to-noise ratios at low frequency (< 0.01 Hz, **M** > 3.5) are usually able to be inverted for a moment tensor.

To obtain M_0 estimates for smaller earthquakes alternative strategies have been developed, which are described here as spectral methods. These spectral methods range from the use of empirical Green's functions (e.g. Mayeda and Walter, 1996; Edwards et al., 2018) to spectral modelling methods (e.g. Edwards et al., 2010). This family of methods share commonality in that they all depend on reference source spectrum models. Boore (2003) pointed out that these methods are derivatives of Aki (1967), who first described the 'omega-squared' model of the source spectrum. Mostly, source definitions assume self-similarity for source scaling (constant stress drop is also assumed), and an inverse-cube power law between spectral amplitude and corner frequency (Figure 1.8).

The most commonly used self-similar model is the Brune (1970, 1971) source definition, given by Equation 1.12:

$$E(f) = \left(\frac{\Psi}{1 + \left(\frac{f}{f_c}\right)^2} \right) \tag{1.12}$$

$$\Psi = \frac{M_0 \langle R_{\Theta\phi} \rangle F \xi}{4\pi\rho v_s^3} = C M_0 \tag{1.13}$$

E(f) is the displacement spectrum (where f is frequency in Hz) for a far-field S-wave pulse, from a point source shear dislocation (with initial radius of 1 km) that grows radially as a circular plane at constant velocity. It is characterised by the long period spectral level, Ψ (Equation 1.13), single corner frequency f_c and the 'omega-squared' decay at f > f_c (see Figure 1.7). Ψ is related to M_0 through a constant (C) which are a set of assumptions about the ruptured media and wave partitioning; $\langle R_{\Theta\phi} \rangle$ is the average radiation pattern (Boatwright, 1978), F is the free surface coefficient (2 for vertically incident SH waves), ξ is a factor which describes partitioning of energy between vertical and horizontal ground motion (Boore, 2003), ρ is the average density at the source (e.g. 2800 kg/m^3) and v_s^3 is the average s-wave velocity at the source (e.g. 3500 m/s).

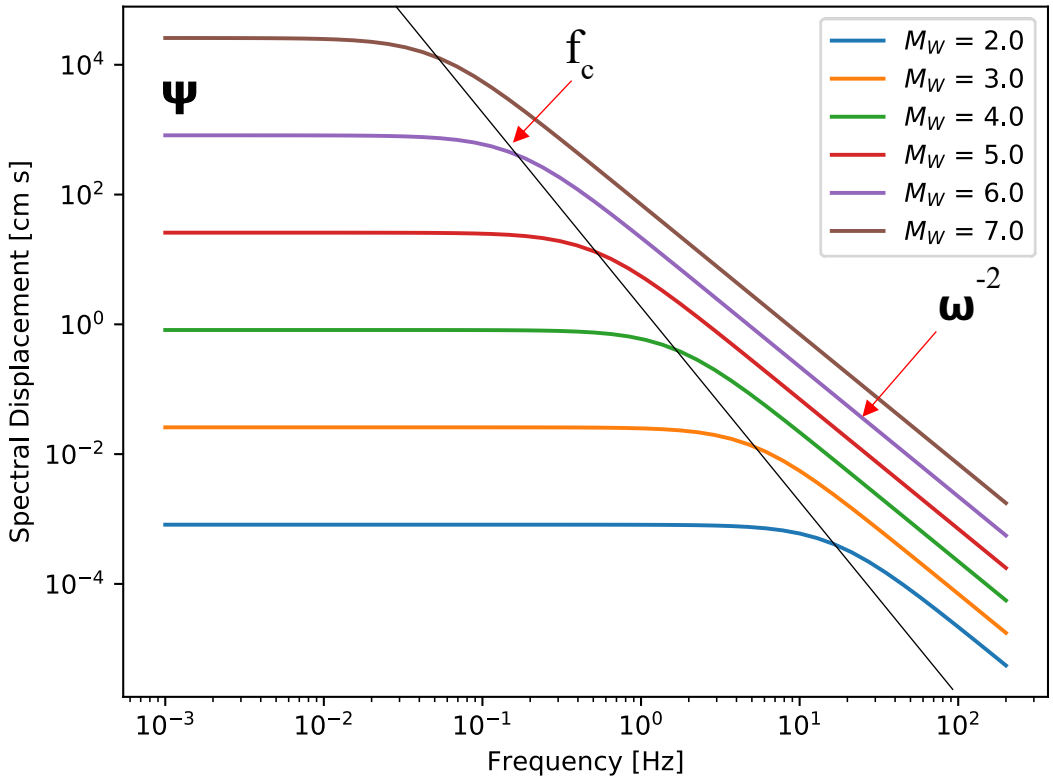

Figure 1.7 – Brune (1970, 1971) model for earthquakes 2.0 < M_W < 7.0 (coloured solid lines) with a constant stress drop of 1 MPa. The locations of the long period spectral level, corner frequency and the characteristic decay are marked in the figure for the M_W = 6 earthquake. The sold black line shows the cubic power law that relates corner frequency to earthquake size (M_0).

One may use the Brune model (where finite fault effects need not be considered) to estimate seismic moment (and therefore M_W), using a spectral fitting approach, by

relating it to the spectrum of recorded (instrument corrected) ground displacement (Equation 1.14) (Ottemöller and Havskov, 2003; Edwards et al., 2008):

$$U(f) = E(f)B(f,t^*)S(R)T(f)I(f) \quad (1.14)$$

Here, E(f) is the source model[12], B(f) is the anelastic attenuation model (for path and site) and S(R) is a geometric spreading model, T(f) is site amplification term and I(f) is the instrument response (which is deconvolved). The model given by Equation 1.14 may then be inverted to the recorded ground motion (after correction for geometric spreading), by leaving Ψ, f_c and t^* (source to site attenuation parameter) as free parameters (Edwards et al., 2010). Usually, there is an attempt to limit the fit to records with a good spectral signal-to-noise ratio, via comparison with the spectrum of pre-signal noise. This can be somewhat limiting for the method as spectral noise (particularly at long periods) can be significant and limit the frequency range for spectral fitting. Fortunately, this method can more reliably use higher frequencies (at the cost of trade-off with the attenuation model) to extrapolate the model to lower frequencies which are related to M_0. In other words, unlike moment tensor inversion this method does not rely on low frequencies (< 0.01 Hz) to predict M_0.

1.5 Magnitude Related Uncertainty Introduced to SHA

Seismic hazard assessment (SHA) is a broad term that pertains to a swathe of sub-topical expert analysis that is combined to estimate the annual rate of exceedance of a particular measure of ground shaking (Baker, 2008). Here, I discuss only the components of SHA that have direct magnitude dependence and how magnitude uncertainty may propagate. The primary stage of SHA involves characterisation of seismic sources, in terms of size (magnitude) and recurrence rate (Giardini et al., 2003). Upon quantifying the size of earthquakes, seismologists typically store this information in earthquake catalogues with other metadata about the event, e.g. origin time, location, depth and associated uncertainties. This catalogued seismicity can be

[12] Most commonly the Brune model but any other valid source definition may be used (e.g. Madariaga, 1976; Boatwright, 1978 etc.).

used to estimate recurrence times which are derived from the Gutenberg- Richter (G-R) relationship (Gutenberg and Richter, 1954), or truncated G-R relationship:

$$\log_{10} N = a - bM(M \leq M_{max}) \tag{1.15}$$

where, N is the cumulative number of earthquakes of magnitude M up to M_{max} (the largest considered earthquake), and a / b give the seismicity rate and relative proportion of small to large events, respectively. The key benefit of the magnitude-frequency distribution (MFD), as described by Equation 1.15, is that it follows a regionally dependent power law. This grants the ability to predict the frequency of earthquakes with given magnitude[13], which is crucial for SHA (Reiter, 1991).

M is preferred to generate unbiased estimates of the seismicity rate parameters as it: (1) is considered state-of-practice and (2) has greater consistency with other branches of SHA (e.g. Ground Motion Prediction Equations) (Arabasz et al., 2016). Moreover, **M** is a great reference magnitude since the scale does not saturate (Kanamori, 1977).

[13] This topic branches into statistical seismology which is beyond the scope of this thesis. Refer to Utsu (2003a) for a reference guide on how recurrence rates are estimated using statistical methods.

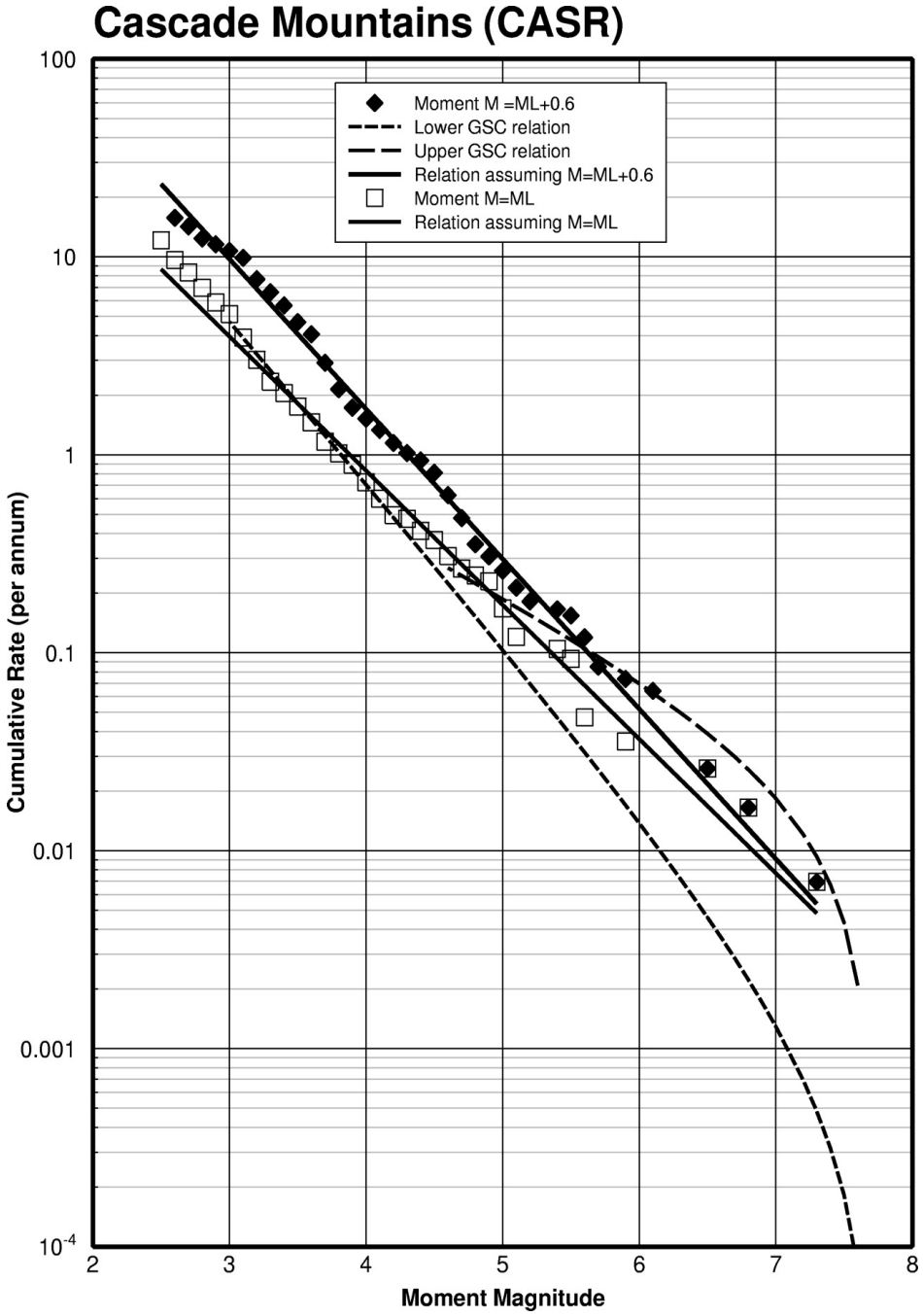

Figure 1.8 – Magnitude recurrence rate curves comparing the catalog with magnitudes adjusted to match **M** = M_L + 0.6 (solid triangles) and the same assuming **M** = M_L (empty squares). Modified from Atkinson and McCartney, A Revised Magnitude-Recurrence Relation for Shallow Crustal Earthquakes in Southwestern British Columbia: Considering the Relationships between Moment Magnitude and Regional Magnitudes, Bulletin of the Seismological Society of America [BSSA], 95(1), p334-340, 2005, https://doi.org/10.1785/0120040095, © Seismological Society of America.

It is possible to use other magnitude ordinates in place of **M** assuming they are consistent, however this assumption can be dangerous. This was pointed out by Atkinson (2004) who looked at magnitude recurrence rates in Canada. They noted that the original earthquake catalogue used for the regional hazard assessment was constructed using a mixture of **M,** body wave magnitude (m_b), coda magnitude (M_C) and (mostly) M_L. However, it was shown by Dewbury and Crossen (1995) that **M** = 0.96 M_C + 0.19, Braunmiller and Nabelek (2002) that **M** = m_b + 0.46, Ristau et al. (2003) that **M** = M_L + 0.6 for offshore earthquakes and **M** = M_L for onshore events (Cassidy et al., 2005). In light of this, Atkinson and McCartney (2005) recalculated the recurrence rates by trying to unify the catalogue via conversion of M_L to **M**. Given that there was still a good degree of uncertainty in the **M**-to-M_L conversion they converted M_L to **M** using both aforementioned relations (Figure 1.8). The magnitude conversions significantly reduced the uncertainty of the G-R slopes by about 0.3 units and showed that the original lower bound recurrence rate curve was too low (lower-most dashed line at **M** > 6 in Figure 1.8). Fortunately, it would not have improved the hazard assessment considerably because the original lower bound slope had a relatively low weighting toward the final hazard assessment (Atkinson and McCartney, 2005). The case study does, however, highlight a couple critical points: (i) inaccurate assumptions about the relationships between magnitude ordinates may lead to underestimated recurrence rates of large **M** earthquakes (significant to SHA), (ii) uncertainty in scaling relationships should also be carefully derived and considered in SHA and (iii) simple M_L adjustments to account for differences in regional attenuation may introduce additional uncertainty. It may be possible to combat point (iii) by defining a uniform M_L scale for multiple regions, as was achieved by Uhrhammer et al. (2011) for California.

In the context of SHA, little focus has been given to the impact of the input magnitudes on the prediction variability (σ) of Ground Motion Prediction Equations (GMPEs) (Holmgren and Atkinson, 2018). Rhoads (1997) pointed out that typical GMPEs are regressed to data assuming there is no uncertainty in the event magnitude. This assumption has two obvious flaws; the first being even **M** values derived from moment tensors have uncertainty. For example, M_W derived by the University of Utah Seismograph Stations (UUSS) have standard error on the order of ~ 0.05 m.u., which was obtained by comparison to similar moment tensor solutions that used the same

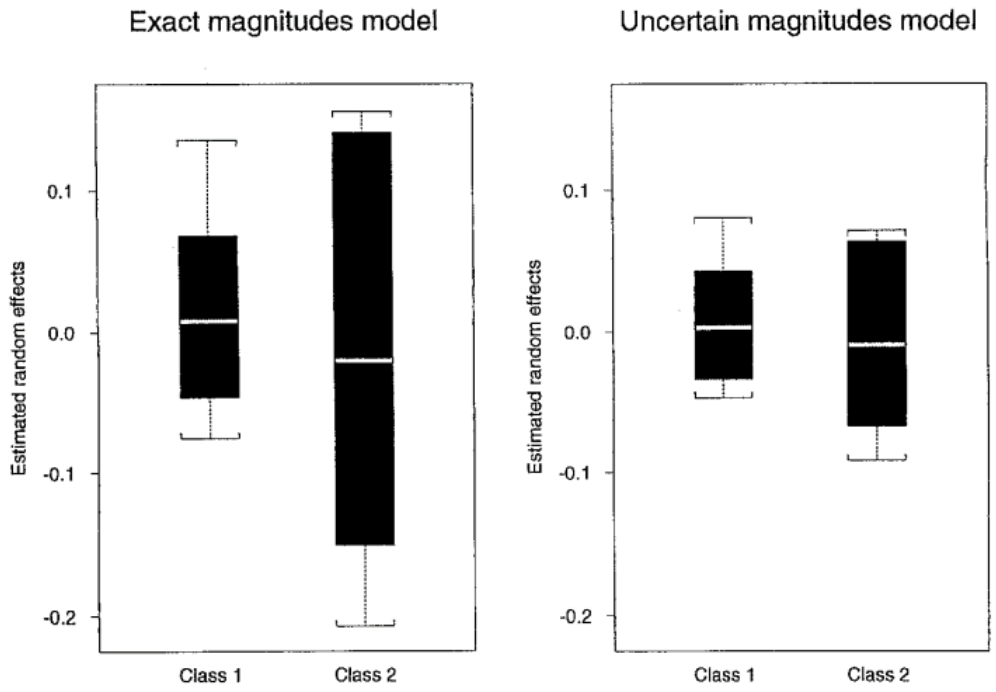

Figure 1.9 – Maximum likelihood estimates of random effects parameter in GMPEs derived assuming magnitudes have no uncertainty (left panel) and magnitudes are uncertain (right panel). Class 1 and Class 2 refer to using only **M** which is derived from M_W estimates and those converted to **M** from M_L respectively. Modified from Figure 1, Rhoades, Estimation of attenuation relations for strong-motion data allowing for individual earthquake magnitude uncertainties, 1997, Bulletin of the Seismological Society of America [BSSA], 87 (6), p1674-1678, doi:N/A, © Seismological Society of America.

velocity model (Arabasz et al., 2016). Secondly, as stated earlier, usually magnitudes are converted to **M** from other ordinates. This process adds an additional layer of uncertainty, which can be particularly problematic if magnitudes come from multiples sources (i.e. different regions/networks) and if magnitude dependent uncertainty is considered (Goertz-Allmann et al., 2011). Rhoades (1997) was able to show the impact of considering magnitude uncertainty (Figure 1.9) on the between-event variability. By considering uncertainty of Class 1 magnitudes (**M** = M_W) and Class 2 magnitudes (**M** converted from M_L) in the regression model, they show a modest reduction of the random effects for Class 1 and (importantly) a significant reduction for Class 2. This suggests that the uncertainty introduced due to scaling and mixing datasets is extremely important for source scaling in GMPEs. A recent study by Kishida et al. (2018) hints that part of this uncertainty could be caused by using an inverse-variance weighting for regression (which assumes variables have zero-correlation). They were

able to reduce the overall uncertainty in multivariate magnitude conversion by assuming the uncertainty in each magnitude ordinate was correlated.

Bindi et al. (2019) suggests an alternate approach, that takes more careful consideration of the type of magnitude ordinate used. They found that **M** might be a better metric for long-period ground motions, where they are dominantly controlled by M_0; M_L may be more appropriate for short-period ground motions, since they show a stronger dependence on stress drop. Certainty, this would help, but this could still benefit from the inclusion of uncertainty. There is also the limitation that M_L has been shown to systematically underestimate **M** at small-to-moderate magnitudes (**M** < 3) (Deichmann, 2006, 2017, 2018). One may question the need for accurate assessment of earthquake magnitude less than $\mathbf{M}_{min}$ ~ 4, the lowermost magnitude typically considered in probabilistic seismic hazard assessment (PSHA) after consideration of risk potential (Bommer and Crowley, 2017). The reason is that in regions of low or moderate seismicity (or for small source zones, e.g. induced seismicity), the bulk of available data is below $\mathbf{M}_{min}$ and the frequency of relevant events ($\mathbf{M} > \mathbf{M}_{min}$) is predicted through extrapolation of the G-R relation (or any alternative magnitude-frequency relations) derived at lower magnitudes.

In summary, modern SHA rely heavily on **M** as a unifying and stable magnitude ordinate. However, implicit and explicit uncertainties may propagate into SHA through magnitude scaling relationships. This is of particular importance when **M** is derived from many sources and over multiple regions. Extra care should be taken to derive realistic magnitude uncertainty so that it can be used to improve SHA assessments by giving confident predictions of ground motion and recurrence rates.

Chapter 2: Moment Magnitude Calculation of Small to Moderate-Size Earthquakes in Utah

Chapter 2 is constructed from a manuscript in preparation to be submitted to the *Bulletin of the Seismological Society of America*. The authors of this manuscript (correct at date of thesis submission) are James Holt (main author), James C. Pechmann, Benjamin Edwards, Keith D. Koper and Relu Burlacu. The study was aimed at calculating moment magnitude for small-moderate earthquakes in Utah, USA by modifying the spectral estimation method of Edwards et al. (2010) to work in this region. The relationships between M_W - M_L and M_C values is evaluated for the purpose of magnitude conversion over a broader range than previously possible for Utah. The scaling relationship between M_L - M_W at small M_L highlights additional uncertainty from the derivation of M_L itself. With the new scaling relationships, the background seismicity rate in Utah may be re-evaluated including the 218 newly calculated M_W. We also discuss potential uncertainty in the attenuation correction used to calculate M_W for current and future small-moderate earthquakes in Utah. James C. Pechmann, Keith D. Koper and Relu Burlacu of the University of Utah Seismograph Stations (UUSS) provided guidance in the adaptation of the method to Utahn earthquakes and helped draft the manuscript. Benjamin Edwards provided key codes that were used for spectral analysis, assisted with the analysis and helped draft the manuscript.

Abstract

We adapt a frequency domain method for moment magnitude (M_W) estimation and apply it to earthquakes in and around Utah—a region of significant seismic hazard which straddles the Intermountain Seismic Belt. The main goal of this work is to develop a capability for fast, automated determination of M_W for small ($M_L < 3.5$) earthquakes for operational use by the University of Utah Seismograph Stations (UUSS). The *Sg* / *Lg* frequency domain method used for this study produces scalar seismic moments similar to those from time domain moment tensor inversions but can be used for smaller earthquakes that lack long period energy. We calibrate this method in the Utah region using well-constrained, pre-determined moment tensor solutions for 53 earthquakes ($3.17 \leq M_W \leq 4.59$). We find that four published attenuation models for the Utah region are unsuitable, necessitating the derivation of a new attenuation model to confidently predict M_W. Our frequency-domain M_W (SgH Spectral M_W)

follows a 1:1 relation with the time-domain Mw when the new attenuation model is used. With our improved methodology, we produce a new M_W catalogue containing 218 SgH Spectral M_W estimates ($1.5 < M_W < 4.0$). We find bilinear relationships for M_W as a function of both M_L and coda-duration magnitude (M_C). The slope of the M_L - M_W relationship is 2/3 for $M_L < 3$, consistent with theory and similar observational studies.

2.1 Introduction

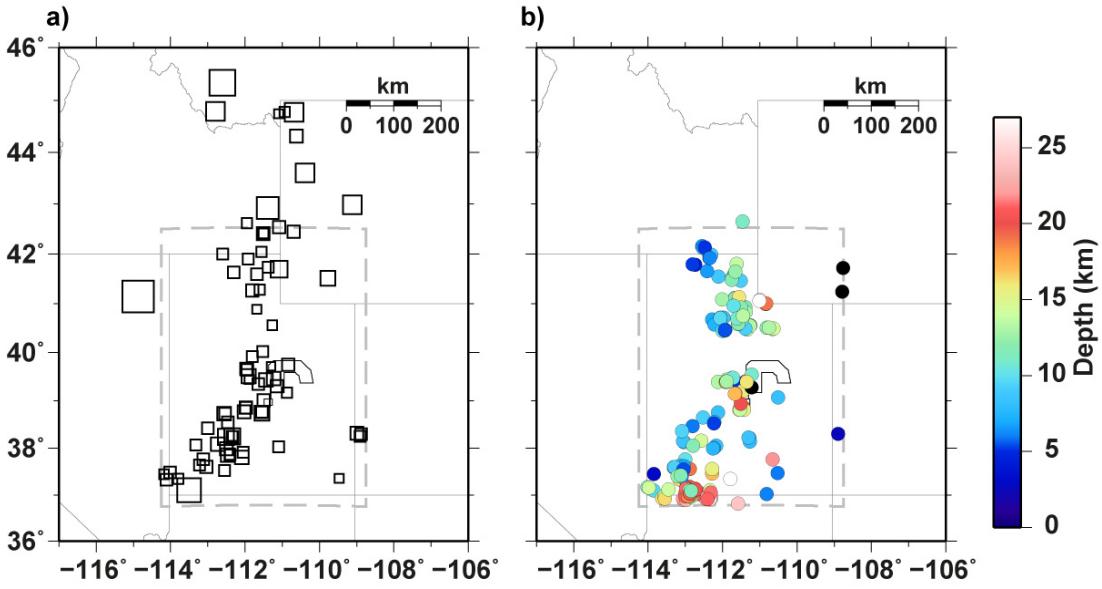

Figure 2.1 - Seismicity maps of showing events with moment tensor M_W (UUSS M_W) (subplot a; Table 1) and the events without moment tensor M_W that were used in this study. The event locations in subplot a) are marked by squares and are scaled by M_W and are presented in Table 1. The events locations in subplot b) are represented by solid circles which are coloured by depth (km) in subplot b). In both subplots the Utah catalogue region is bounded by the dashed line, the Extended Utah Region (Arabasz et al. 2016) is slightly larger by ~ 1° in all directions. Also, the location of a coal mine in central Utah is shown which is bounded by a solid line.

The University of Utah Seismograph Stations (UUSS) routinely monitors seismicity in and surrounding Utah (Figure 2.1), a region of significant seismic hazard which straddles the Intermountain Seismic Belt (ISB) (Smith and Arabasz, 1991). Seismic sources in this region include natural and mining-induced earthquakes, but here we focus only on natural earthquakes. UUSS calculates coda-duration magnitude (M_C) for nearly all seismic events that it locates, and local magnitude (M_L) for the ~50% of events for which the necessary measurements can be obtained from two or more broadband stations (Pechmann et al., 2007; Koper et al., 2016). UUSS also calculates moment magnitude (M_W) for most earthquakes with $M_L \geq 3.5$, and some smaller events,

using time domain moment tensor inversion of long-period waveforms recorded at distances of up to a few hundred kilometres (Whidden and Pankow, 2012). However, M_W is difficult to obtain for $M_L \leq 3.5$ sources with the current UUSS time domain methodology. Consequently, like many other regional seismic networks, UUSS relies on M_L as the primary measure of earthquake size.

Moment magnitude (M_W) (Kanamori, 1977) was defined by Hanks and Kanamori (1979) as:

$$M_W = \frac{2}{3}\log_{10}(M_0) - 6.03 \quad (2.1)$$

It is directly linked to physical properties of the source rupture, described by the seismic moment M_0 (N·m), which is the product of the rupture surface area, S (m^2), the average displacement along the fault surface, $\bar{d}$ (m), and the rigidity of the material, μ (Pa):

$$M_0 = \mu S \bar{d} \quad (2.2)$$

The link to physical rupture properties is an extremely attractive feature of M_W. In the context of seismic hazard, it is preferred that Gutenberg-Richter (G-R) recurrence relation is determined with M_W because it is inherently more consistent with earthquake size (Woessner and Weimer, 2005). Recurrence parameters estimated from G-R are critical to seismic hazard analysis (SHA) as they are used in probabilistic seismic hazard analysis (PSHA) (Beauval and Scotti, 2004). M_W, however, remains challenging to estimate independently at small magnitudes because determination using conventional methods, e.g. moment tensor inversion Minson and Dreger (2008), requires data with good signal-to-noise ratios at low (0.025–0.100 Hz) frequencies. The availability of such data depends on various factors at the time of the earthquake in question (such as the proximity of the earthquake to the seismic stations and low frequency noise levels at the stations). Furthermore, estimating M_W with these methods generally requires accurate earth models, for time domain waveform modelling (Dahm and Krüger, 2014). While not impossible to overcome, these factors become increasingly important for smaller earthquake sources. These factors make it challenging even for well-developed networks (such as the UUSS) to routinely compute M_W for small earthquakes and impractical for many others.

Local magnitude (M_L) is defined as (Richter, 1958):

$$M_L = \log_{10} A - \log_{10} A_0 + S_i \quad (2.3)$$

In UUSS operations A is taken as on half of the largest peak-to-peak amplitude in mm (on a horizontal component simulated Wood-Anderson [W-A] seismograph record) averaged over two horizontal components, $-\log_{10} A_0$ is the distance correction (UUSS uses the correction of Richter, 1958) and the S_i are empirically derived site corrections (Pechmann et al., 2007). The W-A is a short-period instrument with fundamental period (T_0) of ~ 0.8 s. Because of this peak-to-peak amplitude can generally be measured for earthquakes with $M_L << 3.5$, even in the presence of relatively high levels of background noise.

M_L is the preferred size measurement for the UUSS but is only determined for about 50% of earthquakes in the UUSS catalogue. This limitation is likely due to the current (and past) density of broadband stations used to determine M_L and the relatively high background noise (e.g. microseisms). To supplement the M_Ls, the UUSS also calculates coda-duration magnitude (M_C) in the Utah (Equation 2.4) and Yellowstone regions (Equation 2.5) for almost all events (Pechmann, et al., 2006).

$$M_C = -2.25 + 2.32 \log_{10} \tau + 0.0023\Delta \text{ in the Utah region} \quad (2.4)$$

$$M_C = -2.60 + 2.44 \log_{10} \tau + 0.0040\Delta \text{ in the Yellowstone region} \quad (2.5)$$

Here, τ is the signal duration (s) and Δ is epicentral distance (km). The scale was recalibrated by Pechmann et al. (2006) to M_L in Utah and Yellowstone, via orthogonal regression and a revised definition of τ. They re-defined τ to be the length of time from the P-wave onset to where the signal drops below an absolute ground velocity threshold (0.01724 microns/sec), instead of the pre-event noise threshold. This new definition allows for automatic determination of τ and M_C even when the pre-event noise is significant.

It is well understood that the relation between M_L and M_W is non-linear over a wide magnitude range (e.g. Hanks and Boore, 1984; Shemeta, 1989; Edwards et al., 2010; Munafó et al. 2016; Deichmann, 2017; Malagnini and Munafó, 2018; Staudenmaier et al., 2018). For the purpose of SHA, it has become commonplace to develop conversion relationships between M_L and M_W. However, in cases where these relations must be extrapolated below the magnitude range where M_W can be determined confidently, the resultant magnitude conversions may introduce significant uncertainty into SHA. For example, recurrence relations may be incorrect because of over or under estimation of earthquake numbers in small magnitude bins. As a result, extrapolation of the relations to larger magnitudes (more significant to SHA) becomes a significant risk (Staudenmaier et al., 2018).

In this study, we adapt a method to calculate moment magnitudes for small-to-moderate earthquakes below the current UUSS M_W determination threshold. Specifically, we modify the spectral estimation method of Edwards et al. (2010) used previously, with various modification, to calculate M_W in the UK, Japan, Switzerland, Netherlands and California (Edwards et al., 2008, 2009, 2010; Dost et al., 2018; Staudenmaier et al., 2018), to work for earthquakes in the Utah region, for routine use by the UUSS. To calibrate the method, new attenuation models for Utah are generated which we compare to other similar models for the region. We then use moment magnitudes, determined with our preferred attenuation model, to explore the M_W - M_L and M_W - M_C relationships for the Utah region over a wider magnitude range than was previously possible.

2.2 Estimating M_W from Frequency Domain Modelling

In this section, we briefly review theory for calculating Mw from S-wave spectra. For an in-depth review, we refer the reader to Edwards et al. (2008, 2010). The earthquake velocity spectrum, $\widehat{\Omega}(f, R)$, may be simply expressed as a product of the source $[E(f)]$, whole path $[S(R), B(f, t^*)]$, site amplification $[T(f, A)]$ and instrument $[I(f)]$ responses (Equation 2.6):

$$\widehat{\Omega}(f, R) = 2\pi f E(f) S(R) B(f, t^*) T(f, A) I(f) \quad (2.6)$$

Here, $E(f)$ is a Brune (1970, 1971) model for the source displacement spectrum of an Sg phase window taken from the horizontal component (referred to as SgH) and f is frequency. $S(R)$ is a geometrical spreading model and R is distance (km). $B(f, t^*)$ is a model of anelastic attenuation from source to site, and t* is the whole path attenuation operator (Rietbrock, 2001). Finally, $T(f, A)$ is the site amplification model, split into frequency dependent and independent components, A is a constant site factor applicable at low frequencies. To obtain M_W we calculate the scalar seismic moment using the Brune model:

$$M_0 = \frac{4\pi\Psi_i V_{S,i}^3 \rho r_0}{F\Theta_{\lambda\Phi}}, \tag{2.7}$$

where, Ψ_i is the long period spectral displacement plateau at the source, $V_{S,i}$ is the shear wave velocity at the source of earthquake (i), ρ_i, is the density at the source (assumed 2600 kg/m^3), r_0 is the reference source distance (1000 m), F is a factor to account for the free surface effect (F=2) and $\Theta_{\lambda\Phi}$ is a factor accounting for the average radiation pattern of SH propagation over the focal sphere ($\Theta_{\lambda\Phi}$=0.55). Ψ_i is not observed directly, but from Equation 2.6 it is related to Ω_{ij}, the amplitude of the long period spectral plateau (LPSP) of earthquake (i), recorded at site (j) by:

$$\Omega_{ij} = \Psi_i A_j S(R_{ij}) \tag{2.8}$$

The measured LPSP (Ω_{ij}) is the constant amplitude of the SgH spectrum (assuming a Brune source), at frequencies well below the corner frequency (f_c). We assume that the anelastic attenuation are small and frequency-dependent site amplification effects have minimal impact since our model is a smooth fit through the average spectral level; therefore Ω_{ij} becomes a product of LPSP at the source Ψ_i, the frequency independent site amplification factor (A_j) and the geometrical spreading factor $S(R_{ij})$. Here, R is the distance in km from the hypocentre of earthquake (i) to station (j). Edwards et al. (2010) explained that including A_j to calculate moment magnitudes for earthquakes in Switzerland did not significantly improve (1) the agreement to well-constrained moment tensor M_W values or (2) the scatter of individual station M_W estimates using this method. We therefore assume $A_j = 1$ for the remainder of this study and accept a

small trade-off with $S(R_{ij})$. Finally, by measuring Ω_{ij} from an observed spectrum then correcting to the source using $S(R_{ij})$, it is possible to calculate Ψ_i from Equation 2.6 (Brune, 1970, 1971).

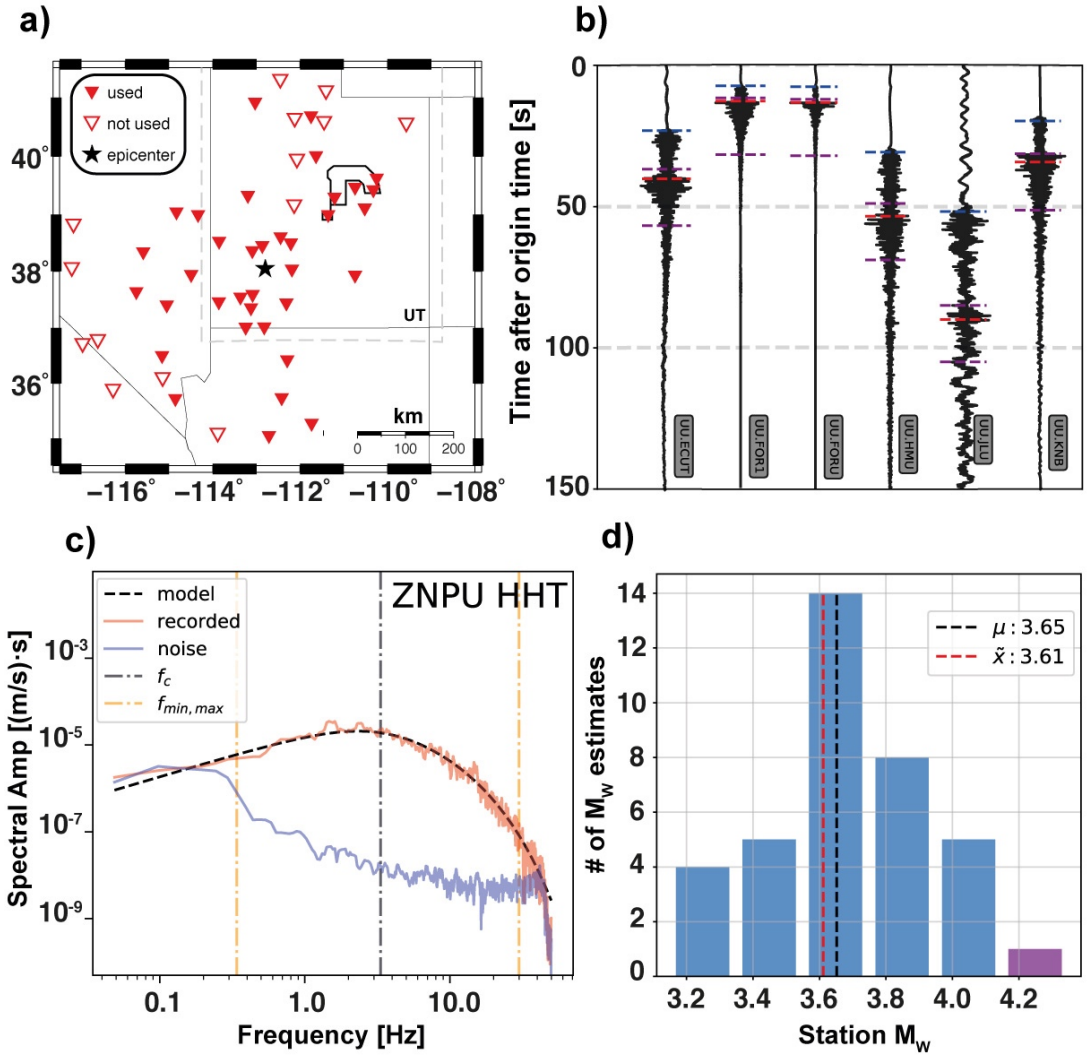

Figure 2.2 - Summary figure of the four stages of the automated M_W estimation workflow. The subfigures (a-d) pertain to calculating M_W for a recent M_W 3.6 earthquake in southwestern Utah. The first stage, a), shows the map of stations automatically selected for the event (red inverted triangles). Stations which were used for the final M_W calculation are represented by solid red symbols and open symbols indicate unused stations. The second stage, b), shows a subset of rotated, transverse-component waveforms with estimates arrival times superimposed. The blue dashed line shows the Pg time, the red dashed line is the Sg time and the two magenta dashed lines show the window chosen for spectral M_W estimation. The third stage, c), shows the optimal model fit (dashed black line) to the recorded velocity spectra at station UU.ZNPU (solid red line) and the spectral noise level (solid blue line). A common source corner frequency (f_c), taken from the station with the smallest misfit to the model (mentioned in the key) is also shown (black dot dashed line) along with the frequency limits of the spectral fit (yellow dot dashed line). The final stage, d), is a histogram of the station M_W estimates. The magenta bar shows an M_W outlier automatically rejected in this workflow. The sample mean (μ) and median ($\tilde{x}$) M_W are shown by the black and red dashed lines respectively. This workflow utilises open source seismic processing tools provided by ObsPy (Krischer et al., 2015).

In practice, it is challenging to directly measure Ω_{ij} since the signal-to-noise ratio generally decreases at low frequencies. However, it is possible to use the higher-frequency part of the spectrum (with generally better signal-to-noise ratio) to reliably extrapolate the Brune model to lower frequencies. Ω_{ij} is therefore obtained via a multi-stage inversion seeking a common source corner frequency (f_c), for all spectra from a given event, and t^* as defining features of each recorded velocity spectrum. For brevity we again refer the reader to Edwards et al. (2010) for a more complete review of the methodology.

Figure 2.2 outlines the workflow for spectral M_W determination for an M_W 3.6 earthquake in southwestern Utah that occurred on 2018-10-30 08:15:17 (UTC) at 38.062°N 112.798°W and a depth of 11.7 km. All pre-processing is performed using the open-source ObsPy package (Krischer et al., 2015). Seismic records from broadband stations (HH and BH) within a 400 km circular domain of the epicentre are obtained from the IRIS data management centre (www.iris.edu/dmc), along with station metadata and response files (Figure 2.2a). The instrument responses are deconvolved and the horizontal-component waveforms are rotated to obtain the transverse component, which we use to better isolate SgH (Figure 2.2b). Average propagation velocities of Pg and Sg phases (derived from seismic refraction experiments), 5.9 and 3.3 km/s respectively (Pechmann et al., 2007), are used to predict travel times, and a 20-second window is created around the Sg arrival. We begin the Sg window at 80% of the predicted Pg - Sg interval time to allow for some uncertainty. We follow the procedure of Edwards et al. (2010) to convert the time-domain signal window frequency: (1) zero-pad to 2^N samples (N is window length), (2) de-mean and apply five 3-pi prolate tapers (Lees and Park, 1995), (3) apply Fast Fourier Transform (FFT) and multiply by sampling period. The spectral content of the window is inverted with a Brune (1970, 1971) model using Powell's minimization to obtain the LPSP (Figure 2.2c). For each velocity spectrum the model is only fit between frequencies where the spectral signal-to-noise ratio is ≥ 3 as indicated by the yellow dot-dashed lines. Again, we follow the Edwards et al. (2010) method to estimate the spectral noise: (1) noise window is from record start to 75% of duration between start and predicated Pg arrival, (2) converted to frequency using same method as the signal window and (3) noise is normalized (excluding zero-padding) by the ratio

of signal and noise window length (to account for differences in window length). For each velocity spectrum the best fit model is converted to displacement and the LPSP is converted to M_0 using Equations 2.7 and 2.8 then station SgH Spectral M_W using Equation 2.1. For $S(R_{ij})$ in Equation 2.7, our model that was developed specifically for Utah (see *section 2.3*) is used to correct the LPSP to the source. The final stage (Figure 2.2d) is to compute a statistical determination of the event SgH Spectral M_W by taking the sample mean of station estimates, after automatically excluding outliers beyond 2.5σ (where σ is the sample standard deviation). We only accept an event SgH Spectral M_W if it has 3 or more station estimates.

2.3 Apparent Geometrical Spreading in the Utah Region

Our objective is to calibrate the spectral method to produce SgH Spectral M_Ws that match UUSS M_Ws as closely as possible. We use the term UUSS M_Ws to refer to the high quality Whidden and Pankow (2012) moment tensor M_Ws plus M_Ws determined for some more recent earthquakes (mostly by K.M. Whidden) using the same procedure (Table B1, Appendix B). In the calibration phase of this study we focus mainly on geometrical spreading ($S(R_{ij})$ in Equation 2.7), then later on consideration of the sensitivity of M_W to the shear-wave velocity (V_S) model. We only report results using the Herrmann et al. (2011) Western US (WUS) model because this model is the one that Whidden and Pankow (2012) used.

Geometrical spreading for body waves can be represented by simple functions of amplitude decay with distance, $R^{-\alpha}$, where R is the distance travelled in km and α is the geometrical spreading coefficient. It has been shown theoretically that α is equal to 1 for body waves (Chapman and Godbee, 2012) and 0.5 for surface waves in a homogeneous half-space. However, continuous geometrical spreading over a wide distance range is rarely observed (e.g. Atkinson and Mereu, 1992). Typical models (derived by fitting observed data) consist of several piecewise linear models of log-amplitude as a function of log-distance, over several distance ranges (≥ 2) and corresponding α, which are regionally dependent (Zandieh and Pezeshk, 2010). Sometimes they are referred to as ‘apparent geometrical spreading’ coefficients and they are usually derived along with a companion anelastic attenuation model (valid

only for the frequencies and region for which they were determined due to potential trade-off).

Apparent geometrical spreading is a critical input for our method since each recorded LPSP must be corrected to the source before it can be substituted into Equation 2.7 to calculate M_0. Since the LPSP has only weak dependence on anelastic attenuation, we assume that the decrease of LPSP with distance is dominated by apparent geometrical spreading of long period *Sg / Lg* in Utah. Figure 2.3 shows the decay of the LPSP values measured in Utah against hypocentral distance (R_{HYP}). This LPSP dataset is for a subset of 53 earthquakes ($3.17 \leq M_W \leq 4.59$) that are presented in Figure 2.1a and Table A1 (Appendix A). We include earthquakes in our subset that; (1) have at least 3 LPSP estimations from SgH spectra that satisfy our minimum SNR threshold, (2) are not mentioned in Whidden and Pankow (2012) as requiring special attention, (3) do not have a significant isotropic component (so they could reasonably be interpreted as double couple) and (4) occurred within the Extended Utah Region defined by Arabasz et al. (2016) as 36.0° to 43.5° N, 108.0° to 115.0° W.

We normalized the LPSP values to the expected Ω of an M_W 3.5 earthquake, Ω_{norm}, with a source velocity ($V_{S,source}$) of 3520 m/s (closest to an assumed average crustal S-wave velocity of 3500 m/s in the WUS model). The normalization is formed using the following equation based on equation 2.7:

$$\Omega_{norm} = \Omega \cdot \left(\frac{1.995 \times 10^{13}}{M_0}\right) \cdot \left(\frac{V_{S,WUS}^3}{3520^3}\right) \quad (2.9)$$

The second factor in Equation 2.9 is the ratio of M_0 (N·m) for theoretical M_W 3.5 and UUSS M_0 (converted to N·m from dyne·cm). The third factor is the ratio between the cubed velocities of the WUS model at source depth, $V_{S,WUS}$, and V_S = 3520 m/s. The resultant normalization cluster removes the effects of M_0 and near-source velocity on Ω to emphasise the observed pattern of apparent geometrical spreading (Figure 2.3).

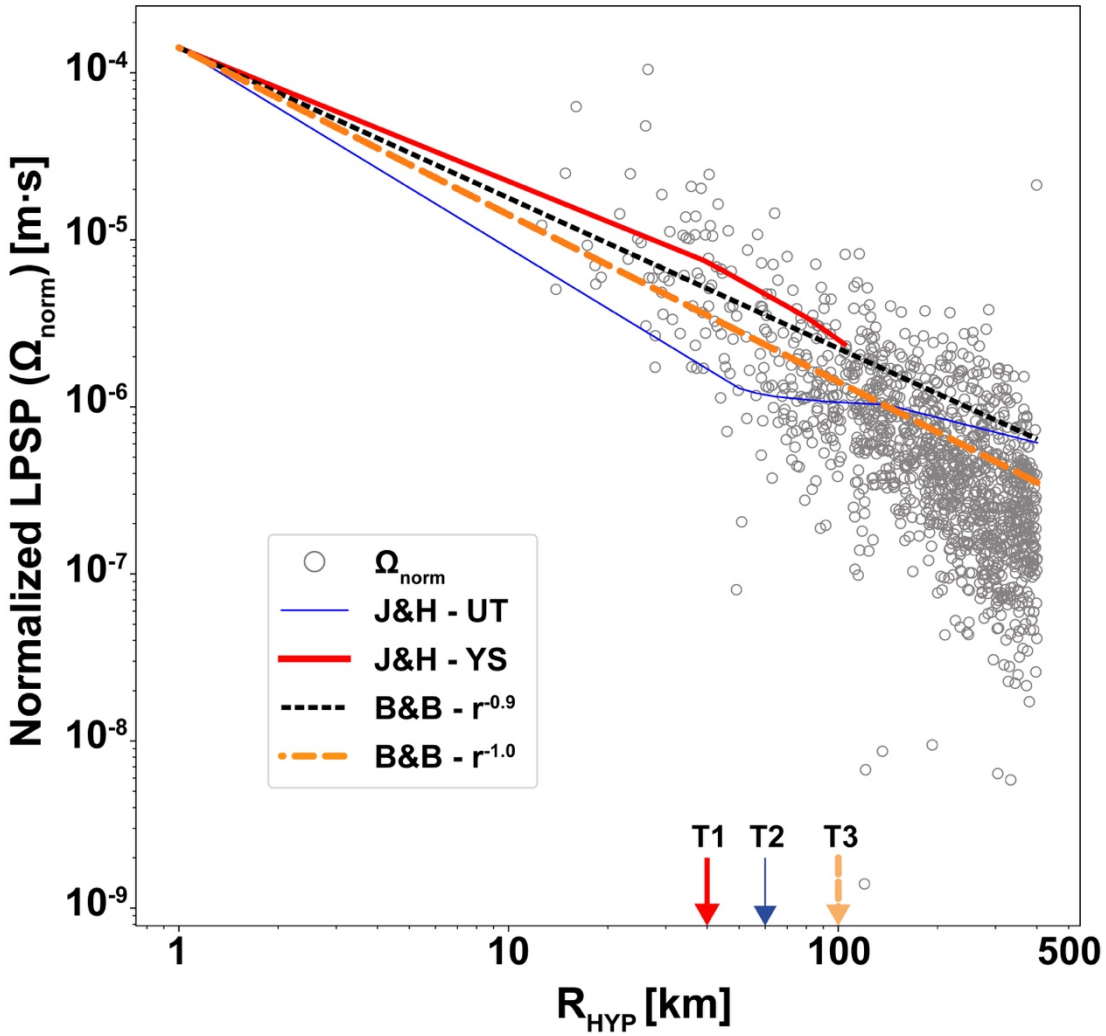

Figure 2.3 - Long period spectral plateau (LPSP) values that are normalized using Equation 2.9 (grey dots - Ω_{norm}) plotted against hypocentral distance (R_{HYP}). The LPSP values are from inversions of SgH spectra from earthquakes which have a known moment tensor solution. For reference we plot models from Jeon and Herrmann (2004) (J&H) for Utah (thick red line - UT) and Yellowstone (thin blue line - YS) and from Brockman and Bollinger (1992), for $r^{-0.9}$ (dashed black line) and $r^{-1.0}$ (thick dashed orange line), where r is distance in km. We also mark three transition zones identified qualitatively with T1, T2 and T3. The color and style of the arrows corresponds to models we believe match data the best and we relate them to possible transitions in apparent geometrical spreading.

We compared apparent geometrical spreading models for Utah from Brockman and Bollinger (1992) and Jeon and Herrmann (2004) to the observed decay of Ω_{norm} (Figure 3). The Brockman and Bollinger (1992) models are termed, B&B - [$r^{-0.9}$, $r^{-1.0}$] for α = 0.9, 1.0 respectively. The Jeon and Herrmann (2004) models are labelled J&H - [UT, YS] for their Utah and Yellowstone region models, respectively. In the magnitude range of interest Ω is weakly dependent on whole path attenuation (t^*) and, by extension, the quality factor (Q_S); we therefore only compare the frequency independent parts of their models (representing geometrical spreading) with Ω_{norm}. Each model was anchored at R_{HYP} = 1 km to the predicted value of Ψ (Equation 2.7)

for a theoretical M_W 3.5 earthquake (assuming a Brune source), with $V_{S,source}$ = 3520 m/s (referred to henceforth as Ψ_{REF}). Ψ_{REF} is the level of the LPSP, as predicted by the Brune model, at the source for the theoretical earthquake scenario to which we normalize our observations. The difference between anchor at the source and the LPSP (measured at some arbitrary distance) is our target for a theoretical M_W 3.5 earthquake and we should not correct to a level significantly different from this value (i.e. outside of the scatter of Ω_{norm}). We trust that this anchor point is reasonable for our dataset because we normalized our observations (using M_0 and V_S) to the theoretical scenario we predicted the source anchor for.

Qualitatively, it is clear from Figure 2.3 that none of the models adequately match the observed decay of Ω_{norm} over the entire distance range (1 to 400 km). The observed distance dependence of Ω_{norm} is unique to our dataset, requiring a new model. The single slope Brockman and Bollinger (1992) model with $\alpha = 1$ decay is the most reasonable approximation over the whole distance range, but systematically underpredicts near-field measurements (up to R_{HYP} ~40 km), suggesting that $\alpha = 1$ is too fast for near-field measurements of Ω. This observation appears contrary to similar studies, which usually report $\alpha > 1$ at short distance ranges ($R_{HYP} < 50$ km) (e.g. Atkinson and Boore, 2013). Importantly, we note there are few studies which have experimented with a source anchor (e.g Atkinson and Boore, 2013). Likely, this is because other studies lack a confident way to predict what this value should be. Considering the distance range $10 < R < 60$ km in Figure 2.3, one could fit a model with a faster than $\alpha = 1$ decay to Ω_{norm} (see *section 2.6*), as with the other studies; however this model would not extrapolate backwards to the predicted Ψ_{REF}. Since we trust the anchor point of Ψ_{REF}, $\alpha < 1$ would be required to fit the near-field data cloud ($10 < R < 40$ km) and satisfy this constraint; as is made clear by comparing Ω_{norm} with B&B [$r^{-0.9}$] and J&H [YS] ($\alpha < 1$ near-field decay). Either B&B [$r^{-0.9}$] or J&H [YS] (or some model between) could provide a resonable fit to Ω_{norm} up to ~ 40 km, around where the J&H [YS] model changes. We mark this as the first possible transition point (T1) on Figure 2.3. Between ~60 to 100 km it appears that J&H [UT] is the best match and we label a second possible transition point at 60 km (T2) on Figure 2.3. Finally, beyond 100 km J&H [UT] does not match the decay and the best model is B&B [$r^{-1.0}$], which we mark as the final model transition point (T3) on Figure 2.3. Qualitatively, in

order to accommodate all of the turning points (and also connect to our anchor at R_{HYP} = 1 km) we require a model with at least four segments.

2.3.1 Derivation of a New Apparent Geometrical Spreading Model

The discussion in the previous section serves to inform the development of a new piecewise linear model. We suggest that the minimum complexity of four segments is required, or three turning points, referred to as hinges henceforth, in order to satisfy our additional constraint on the model at 1 km ($G[R = 1\ km] \equiv \Psi_{REF}$). We design a data driven approach to determine where those hinge points should lie. Since Ω_{norm} is very unevenly distributed in log-log space, model parameters for each piecewise linear segment are determined using a weighted least squares algorithm. Weights for each data point, w_i, are determined by splitting the data into equal sized log-distance bins (j) and taking the square root of the inverse of the log of the number of data (N) in each bin.

$$w_i = \sqrt{\frac{1}{\log_{10} N_j}} \tag{2.10}$$

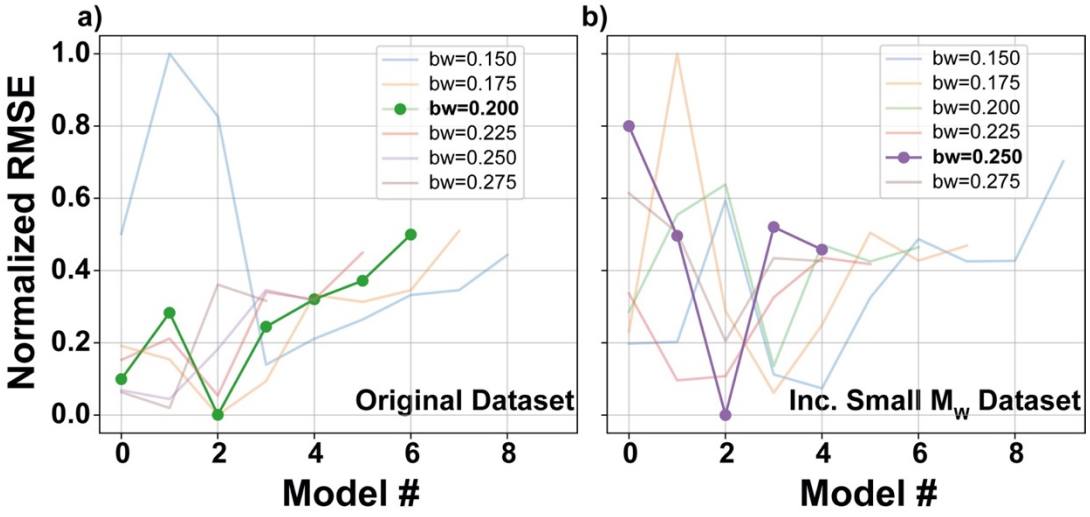

Figure 2.4 - Plot of normalized root mean square error (RMSE) of model candidates, with variable hinge points (based on our grid search) and variable binning width (bw). An optimal model is chosen by iterating over all binning widths (log-distance) and several combinations of hinge points in a grid search, then accepting the minimum RMSE model (highlighted in each subplot). Subplot a) shows shows the results only using Ω_{norm} from earthquakes in Table 1 (original dataset). Subplot b) shows the results when including Ω_{norm} values from additional earthquakes with SgH Spectral M_{WS} calculated using the first iteration of the apparent geometrical spreading model.

The weighting scheme given by Equation 2.10 was found by iterative trial and error. We compared the linear fit of each segment with the binned Ω_{norm} (0.05 log-distance spacing from log_{10} 10 to log_{10} 400 km) and used weights which gave the best visual match. Each piecewise segment, following the first (anchored to Ψ_{REF}), is constrained such that it must begin at the end of the prior segment (hinge point). This constraint ensures a contiguous model. To find the optimal model, we perform a grid search over the binning width and the locations of three hinge points to find the minimum root mean square error (RMSE) of the linear model fit to the data. The location of the hinge points were restricted to the edges of each bin (nodal points). We iterated over log-distance (log_{10} 10 km to log_{10} 400 km) with bin widths of 0.15 to 0.275 in 0.025 log-unit increments. We only look for combinations of hinge points (H) that are: (1)

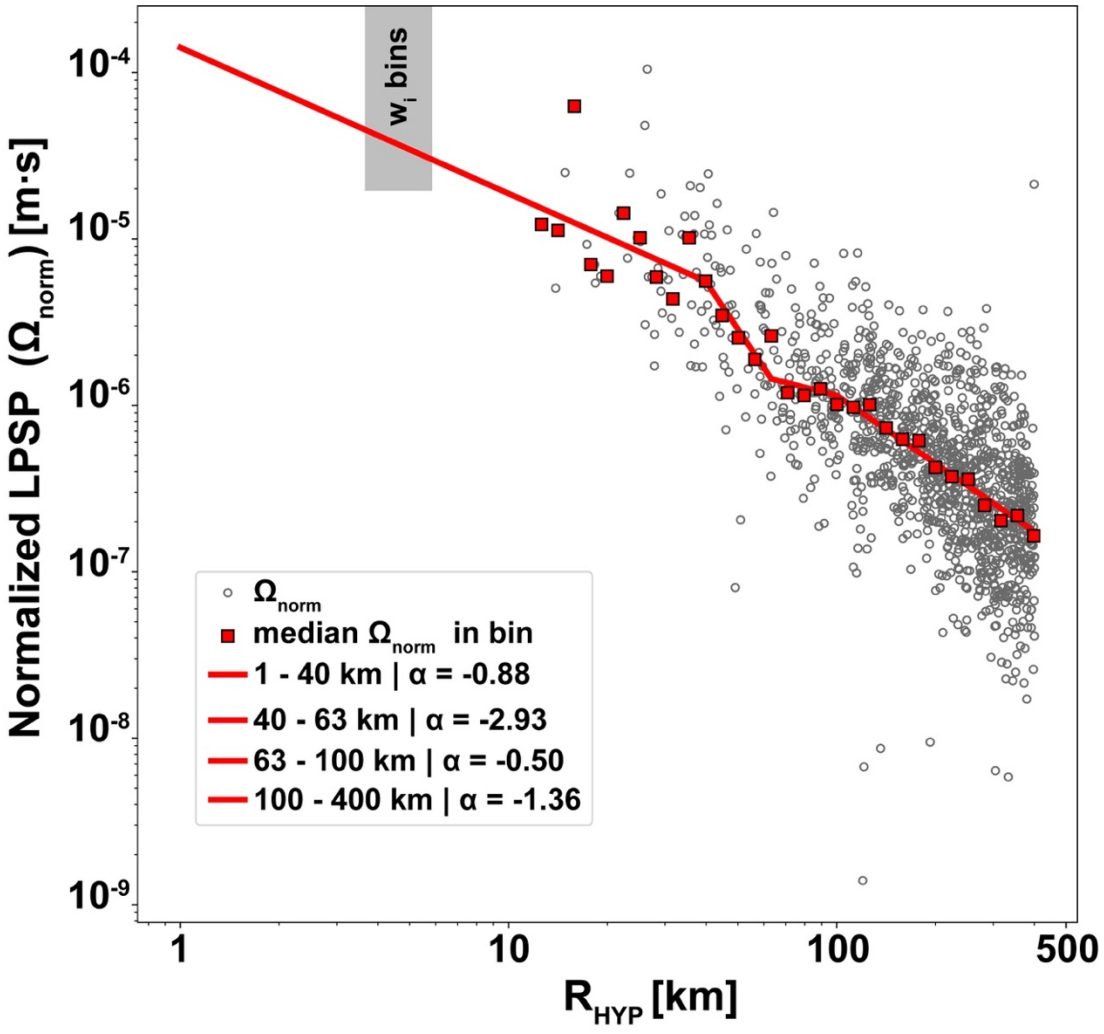

Figure 2.5 - New apparent geometrical spreading model for Utah created using the normalized LPSP data (Ω_{norm}) measured from earthquakes in Table A1, Appendix A, only. The red squares are the median of binned Ω_{norm} (0.05 log-distance spacing). The model is anchored to Ψ_{REF} at R_{HYP} = 1 km. The grey box represents the binning width, j, (0.2 log-distance spacing) used to calculate the weights for the weighted least squares scheme.

increasing with distance (e.g. H1 < H2 < H3) and (2) H combinations must not be selected from adjacent log-distance bins.This resulted in 8 - 16 bins per model and in 4 - 10 distance combinations. Varying the bin widths allows for greater variability in the number and location of H, thereby increasing the search space for an ideal model. Figures 2.4a and 2.4b show the results of the grid search and Figure 2.5 shows the optimal apparent geometrical spreading model (Holt et al. [O]; Table 2.1). To gauge uncertainty on the slopes of our optimal model we used a 10% random replacement bootstrapping scheme (Efron, 1987). Specifically, keeping our distances fixed, we randomly replaced 10% of the data in each distance rage 1000 times and recalculated the slopes. The standard deviation for each slope from bootstrapping are given in Table 2.1 and the bootstrap distributions for each slope are shown in Figure A1 (Appedix A).

Table 2.1 – Table of model parameters for various geometrical spreading models for Utah and Yellowstone. B & B [$r^{-0.9}$] / [$r^{-1.0}$] are from Brockman and Bollinger (1992). J & H [UT] / [YS] are from Jeon and Herrmann (2004) and are for the Utah and Yellowstone regions respectively. Holt et al. [O] / [R] are the original / refined apparent geometrical spreading models created during this study. The standard deviation of each slope from bootstrapping is also shown. R in all cells is hypocentral distance in kilometres and α is the apparent geometrical spreading coefficient for the given model segment.

Model	$-\alpha_1$ $R_{1\ (km)}$	$-\alpha_2$ $R_{2\ (km)}$	$-\alpha_3$ $R_{3\ (km)}$	$-\alpha_4$ $R_{4\ (km)}$	$-\alpha_5$ $R_{5\ (km)}$
B & B [$r^{-0.9}$]	0.90 R > 1	-	-	-	-
B & B [$r^{-1.0}$]	1.00 R > 1	-	-	-	-
J & H [YS]	0.80 1 < R ≤ 40	1.10 40 < R ≤ 80	1.40 80 < R ≤ 105	-	-
J & H [UT]	1.20 1 < R ≤ 50	0.55 50 < R ≤ 60	0.20 60 < R ≤ 90	0.10 90 < R ≤ 140	0.50 R > 140
Holt et al. [O]	0.88 ± 0.02 1 < R ≤ 40	2.93 ± 0.28 40 < R ≤ 63	0.50 ± 0.33 63 < R ≤ 100	1.36 ± 0.07 100 < R ≤ 400	-
Holt et al. [R]	0.90 ± 0.01 1 < R ≤ 43	2.57 ± 0.07 43 < R ≤ 76	0.44 ± 0.08 76 < R ≤ 136	1.54 ± 0.04 136 < R ≤ 400	-

2.3.2 Refinement of Apparent Geometrical Spreading Model

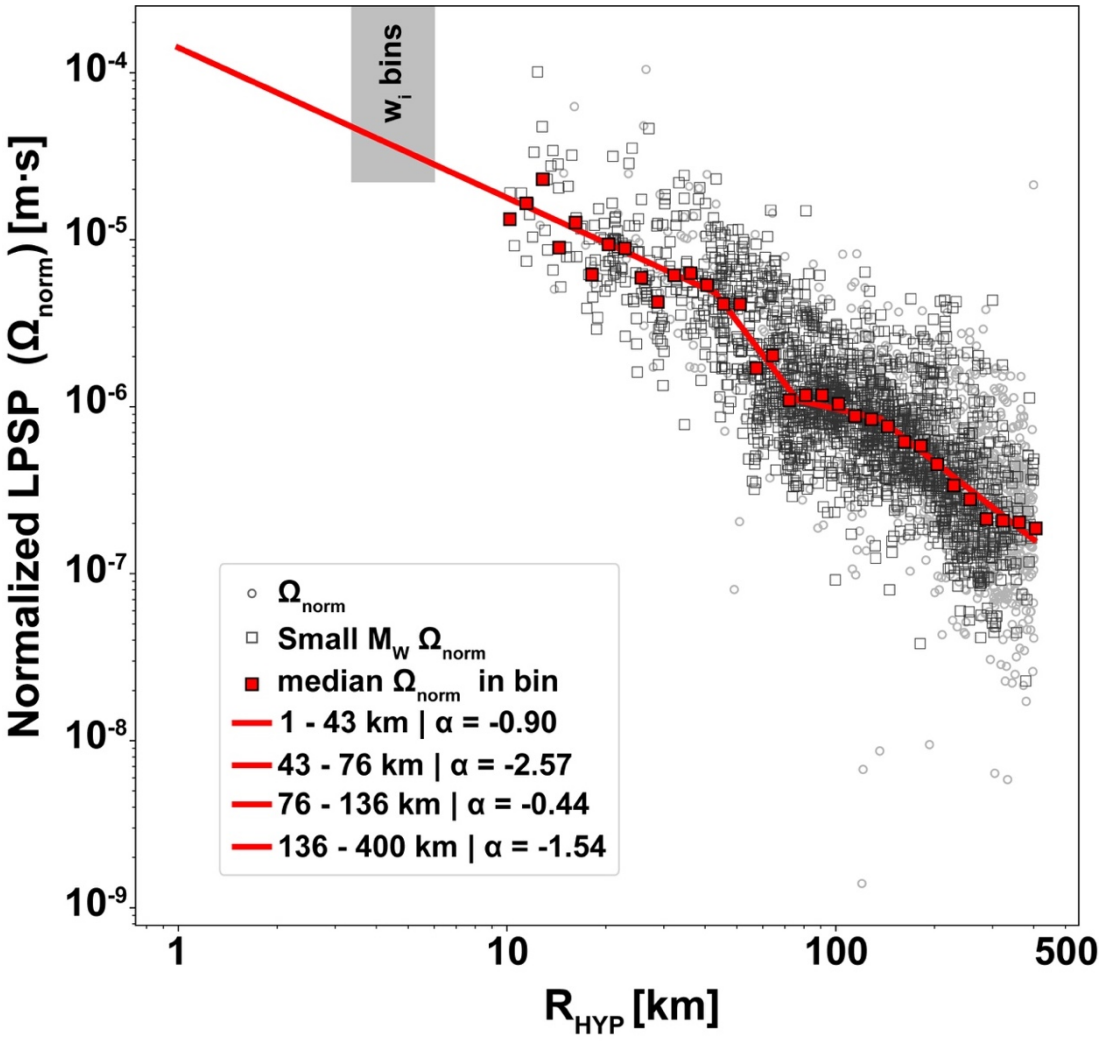

Figure 2.6 - Refined apparent geometrical spreading model calculated using data earthquake data from Table 1 and additional data from smaller magnitude earthquakes with SgH Spectral M_0. The red squares are the median of binned Ω_{norm} (0.05 log-distance spacing). The small magnitude (M_0) estimates are calculated using the first iteration of the apparent geometrical spreading model (Figure 5).

One potential problem with the geometrical spreading model developed in the previous section is that one of the hinge points (Figure 2.5) lies in a region of sparse data (R_{HYP} ~ 40 km). We chose to try to better constrain this hinge point by adding additional data points that we obtained for small M_L sources that we obtained by applying our SgH Spectral M_W method with our initial apparent geometrical spreading model (Table 2.1). Following the methodology of the previous section, we normalised Ω for the small M_L earthquakes using Equation 2.9. We acknowledge that some circular reasoning is introduced by normalizing the data to M_0 calculated from SgH Spectra since the Holt et al. [O] geometrical spreading model and SgH Spectral M_0 are not independent. To address this issue, we limit our new Ω_{norm} dataset to earthquakes with a minimum -

maximum distance ratio of at least 2. This restriction reduces circularity because, theoretically, the relative distance decay between measurements should be preserved, regardless of the M_0 normalization. We added these new values of Ω_{norm} to our database and reapplied our grid search. The results of the new grid search are shown in Figures 2.4c and 2.4d and the final model is shown in Figure 2.6 and also in Table 2.1 (Holt et al. [R]) along with the standard deviation derived from bootstrapping (the bootstrap distributions are also shown in Figure A2 (Appendix A). Finally, we show a comparison between the Holt et al. models in Figure 2.7.

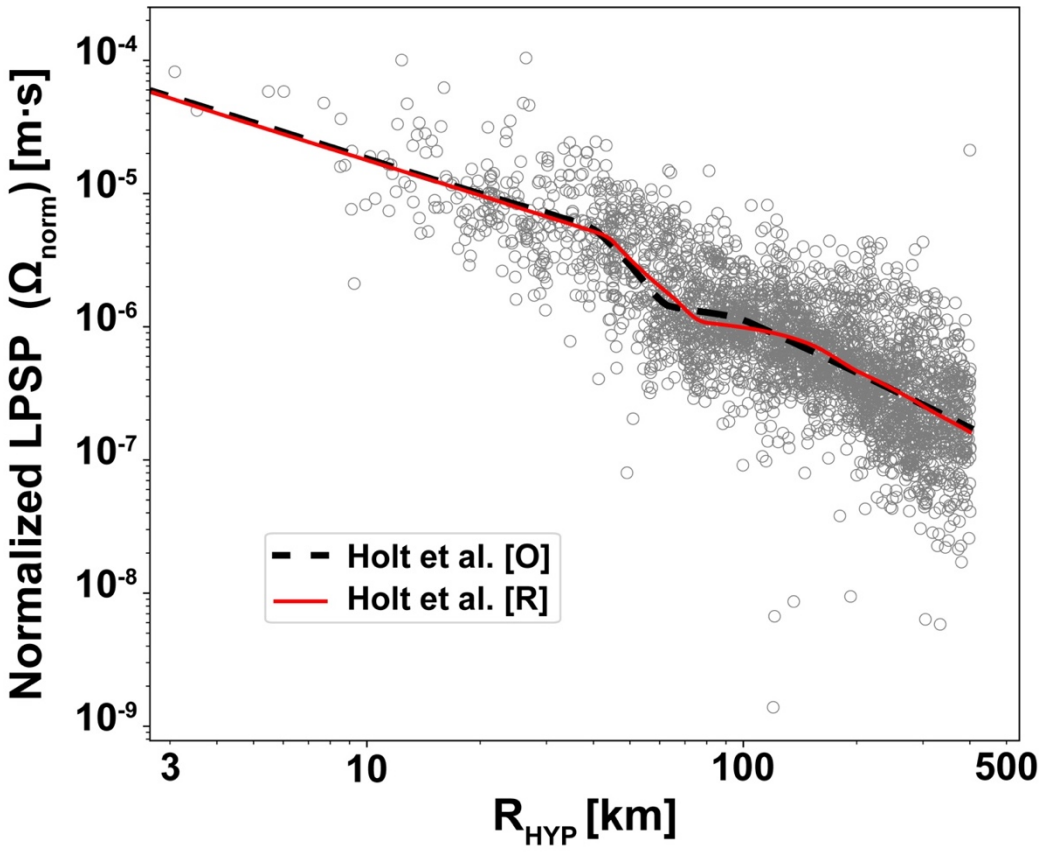

Figure 2.7 - Comparison of the original (dashed black line – Holt et al. [O]) and refined (solid red line – Holt et al. [R]) apparent geometrical spreading models. The original model was determined using Ω_{norm} calculated only from earthquakes with UUSS M_{WS} (Table 1). The final model included Ω_{norm} values calculated from smaller earthquakes with preliminary SgH Spectral M_{WS}. Values of Ω_{norm} measured at R_{HYP} < 10 km are included on this plot for comparison only but were excluded from regressions for the Holt et al.[R] model. Parameters for both models are summarized in Table 2.1

2.4 Results: SgH Spectral M_W Validation

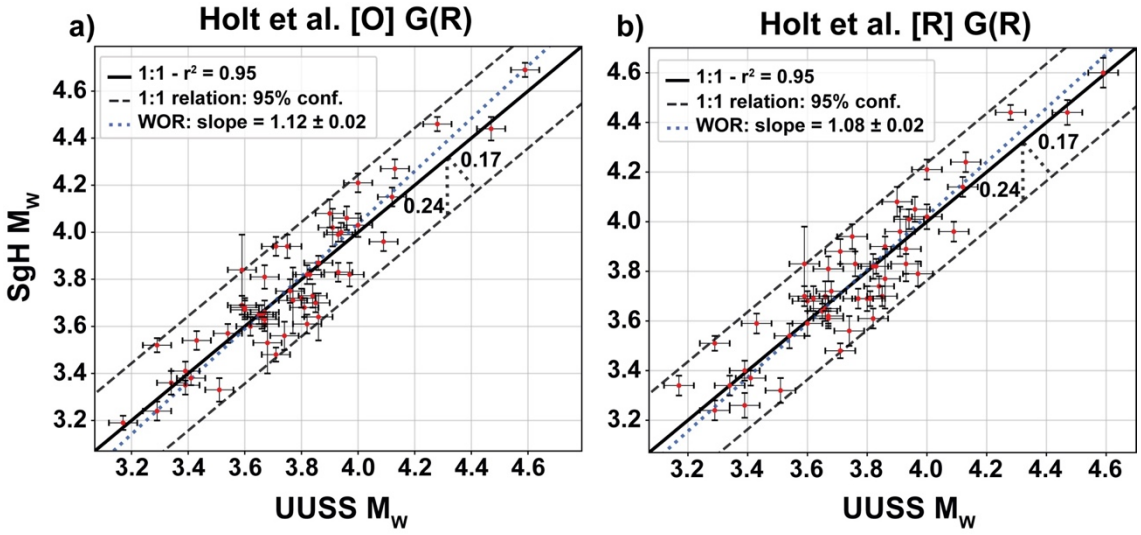

Figure 2.8 - Comparison of SgH Spectra M_W with UUSS M_W (red circles) and their respective standard errors for earthquakes in Table 1, before (subplot a) and after (subplot b) refinement of the apparent geometrical spreading model. The solid black line is a 1:1 relation and the black dashed lines are 95 % orthogonal confidence limits. The standard error is estimated by calculating the residual of orthogonal distances to the 1:1 relation. The dashed blue line calculated with a weighted orthogonal regression (WOR) between SgH Spectral M_W and UUSS M_W and ± one standard deviation on the slope.

We assess the accuracy of the SgH Spectral M_W by direct comparison with the UUSS M_Ws used to calibrate the geometrical spreading function (Table A1; Appendix A). Figure 2.8 shows the relation between UUSS M_W and SgH Spectral M_W before (Figure 2.8a) and after (Figure 2.8b) refinement of the apparent geometrical spreading model. We tested both models to (1) ensure SgH Spectral M_W with the original model had reasonable accuracy and (2) to see if the refinement improved accuracy. Since error in SgH Spectral M_W and UUSS M_W is of a similar magnitude it is only suitable to use orthogonal metrics in our statistical models. Therefore, all of the following statistical tests and errors (r^2 and confidence limits) consider orthogonal distances only.

First, for both cases we performed a weighted orthogonal regression (WOR) between the M_W estimates. Each WOR was calculated using ODRPACK (Version 2.01; Boggs et al., 1989), and weights are estimated from the variance ratio of each point. In both cases the WOR does not give a slope of 1 (1.12, 1.08 respectively); we see a small improvement after the refinement. However, the relation over such a small range and size could be biased by a few outliers. To complement the WORs we also assessed the validity of the expected 1:1 relation and provided 95% confidence limits calculated using the orthogonal residuals. In both cases almost all of our data points fall within

95% confidence limits assuming a 1:1 relation. Not only this, but both cases give an r^2 statistic of 0.95 assuming a 1:1 relation. We see in both cases that only 1 out of 53 points lie outside of the 95% limit. In each case the point is for the same event, which has a high standard error and therefore could conceivably fall within the 95% limit. Considering the above discussion, the 95% confidence tests and the r^2 statistic, we conclude that our data follow a 1:1 relation in both cases and the refinement provided a small improvement in accuracy.

Finally, we present M_W residuals (UUSS M_W – SgH Spectra M_W) before (Figure 2.9a) and after (Figure 2.9b) refinement of the apparent geometrical spreading model. Assuming a Gaussian model, we estimated the probability density functions (PDFs) of both sets of residuals (dotted red lines) and find they appear to follow a normal distribution. The PDFs change only slightly when the different attenuation models are used, although the residual distributions look more different. For both residual distributions, standard error / standard deviation is 0.02 / 0.12 magnitude units which is further evidence of a close agreement between UUSS M_W and SgH Spectra M_W.

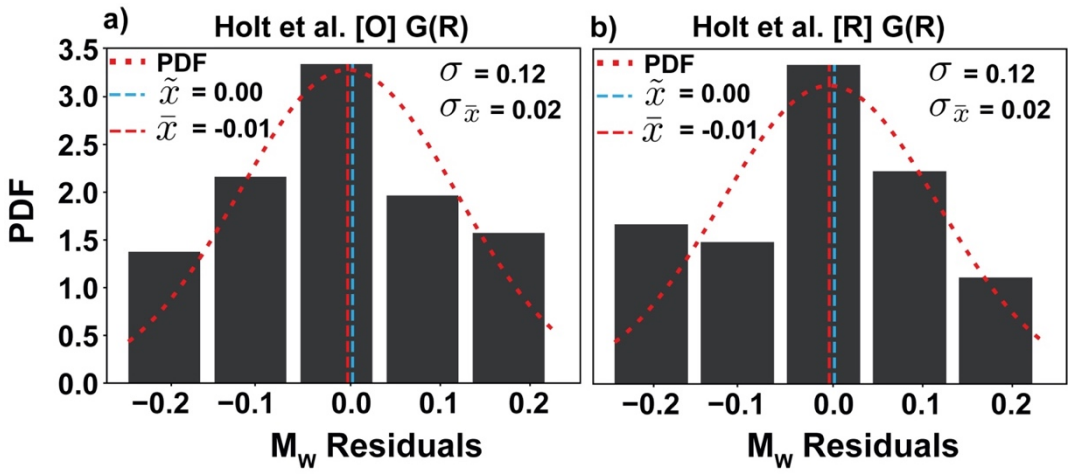

Figure 2.9 - Comparisons of UUSS M_W - SgH Spectra M_W distributions before (subplot a) and after (subplot b) refinement of the apparent geometrical spreading model. The sample mean ($\bar{x}$) / median ($\tilde{x}$) for the M_W residuals are specified and marked by dashed red and blue vertical lines, respectively. Standard deviation (σ) and standard error of the mean ($\sigma_{\bar{x}}$) are indicated for each M_W residual distribution. We estimate the probability density function (PDF) (dotted red line) and show that M_W residuals appear to approximate a normal distribution.

2.5 Results: Relationship between M_W - M_L and M_C in Utah

Once satisfied that the SgH Spectral M_Ws are in agreement with the UUSS M_W, where both are available, we calculated SgH Spectra M_W for a catalogue of events with UUSS M_L but no UUSS M_W. Furthermore, we again constrained our catalogue to events within the Extended Utah Region, defined by Arabasz et al. (2016). Then, following our methodology, we calculated SgH Spectra M_W for 218 events ($0.94 \leq M_L \leq 4.03$, $0.93 \leq M_C \leq 4.15$).

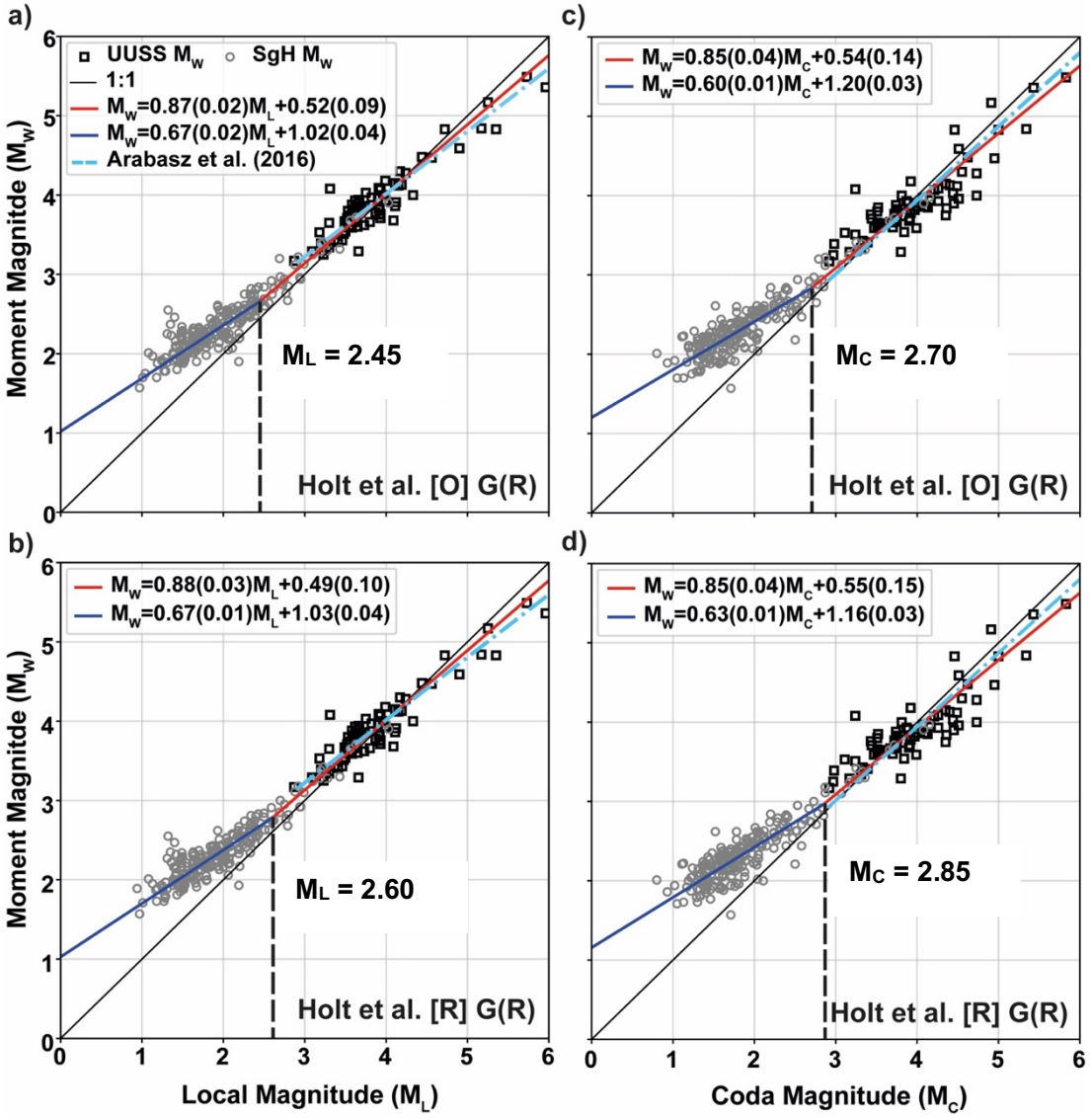

Figure 2.10 - New bilinear relationships between Mw and M_L or M_C derived using SgH Spectral M_W combined with a UUSS Mw dataset. The subplots a) and b) show M_W versus M_L (UUSS) before and after (respectively) refinement of the apparent geometrical spreading model used to calculate SgH Spectral M_W. Similarly, subplots c) and d) show M_W versus M_C (UUSS) before and after (respectively) refinement of the apparent geometrical spreading model. Overlain in each panel is a bilinear relationship derived via weighted orthogonal regression (WOR). The model equations and ± one standard deviation are provided in the legend as well as in Tables 2 and 3. Break points between linear models are shown by a black dashed line in each subplot. For comparison with M_W - M_L and M_C (all subplots) we show the relations derived by Arabasz et al. (2016) for the Utah (dash-dot light-blue line).

With this newly expanded M_W dataset, we determined new $M_W - M_L$ (Figures 2.10a and 2.10b) and $M_W - M_C$ (Figures 2.10c and 2.10d) relations for the Utah region. These new relations are valid over wider ranges of M_L and M_C than the relations that Arabasz et al. (2016) developed and used to estimate M_Ws for the Working Group on Utah Earthquake Probabilities earthquake catalogue (Tables 2.2 and 2.3). Our dataset is updated from Pechmann and Whidden (2013) and Arabasz et al. (2016) but includes only earthquakes with UUSS M_Ws (Table 1). It is clear from inspection of Figure 2.10 that a single linear relation will not fit either the $M_W - M_L$ or $M_W - M_C$ datasets, consistent with the findings of other studies cited in the Introduction. Following some of these studies e.g. Shemata (1989) and Staudenmaier et al. (2018), we search for a bilinear relation between $M_W - M_L$ and $M_W - M_C$. Specifically we search for a piecewise linear model with two linear segments, joined at a single hinge point.

Study	M_W vs M_L Relationship 1	M_W vs M_L Relationship 2
Arabasz et al. (2016)	$M_W = 0.79M_L + 0.85$ $2.87 < M_L < 6.05$	-
Holt et al. [O]	$M_W = 0.87(\pm0.02)M_L +$ $0.52(\pm0.09)$ $2.45 < M_L < 6.05$	$M_W = 0.67(\pm0.02)M_L +$ $1.05(\pm 0.06)$ $0.94 < M_L < 2.45$
Holt et al. [R]	$M_W = 0.88(\pm0.03)M_L +$ $0.53(\pm 0.10)$ $2.60 < M_L < 6.05$	$M_W = 0.67(\pm0.01)M_L +$ $1.03(\pm 0.04)$ $0.94 < M_L < 2.60$

Table 2.2 – M_W vs M_L relationship summary and comparison for Utah.

Table 2.3 - M_W vs M_C relationship summary and comparison for Utah.

Study	M_W vs M_C Relationship 1	M_W vs M_C Relationship 2
Arabasz et al. (2016)	$M_W = 0.93M_C + 0.23$ $2.91 < M_C < 6.06$	-
Holt et al. [O]	$M_W = 0.85(\pm0.04)M_C +$ $0.54(\pm0.14)$ $2.70 < M_C < 6.06$	$M_W = 0.60(\pm0.01)M_C +$ $1.20(\pm0.03)$ $0.80 < M_C < 2.70$
Holt et al. [R]	$M_W = 0.85(\pm0.04)M_C +$ $0.55(\pm0.15)$ $2.85 < M_C < 6.06$	$M_W = 0.63(\pm0.01)M_C +$ $1.16(\pm0.03)$ $0.80 < M_C < 2.85$

To find the best model, the hinge point (H) is iterated over the range $1.5 < M_L < 4.0$ in steps of 0.05 magnitude units. For each iteration we determine model parameters for both linear segments with WOR, ensuring both models connect at the hinge point. This constrained fit is implemented in two ways; (1) calculating the $M_L < H$ model and using it to fix the value at $M_L = H$, for the $M_L > H$ model determination (method 1) or (2) calculating the $M_L > H$ model and using it to fix the value at $M_L = H$, for the $M_L < H$ model determination (method 2). The weights are determined for each data point using the ratio of error variance. We calculate the root mean square error (RMSE) of all data for each model to inform our decision which are the best. This exact procedure was then repeated to calculate relationships for M_W versus M_C. The results are presented in Figure 2.11 and the relations are given in Table 2.2 (M_W - M_L) and Table 2.3 (M_W - M_C), respectively. For the $M_W – M_L$ relations we make the observation that the misfit curves are flat between H = 2.2 to 2.8. Since there is an expected theoretical relation between $M_L – M_W$ at $M_L < 3$, we decided to pick the model whose lower slope was closest to the theoretical value of ~0.67 (see *section 2.6*). For both sets of SgH

Spectral M_W this model had a similar RMSE to the global minimum (Figures 2.11a and 2.11b). Because there is no similar relation for M_W – M_C in our case we simply chose the model that gave a global minimum RMSE (Figures 2.10c and 2.10d). We chose this method over a more standard segmented regression because we wanted to use the same orthogonal regression software throughout the study, which does not support segmented regression; therefore, we created a bespoke method using the ODR Pack software.

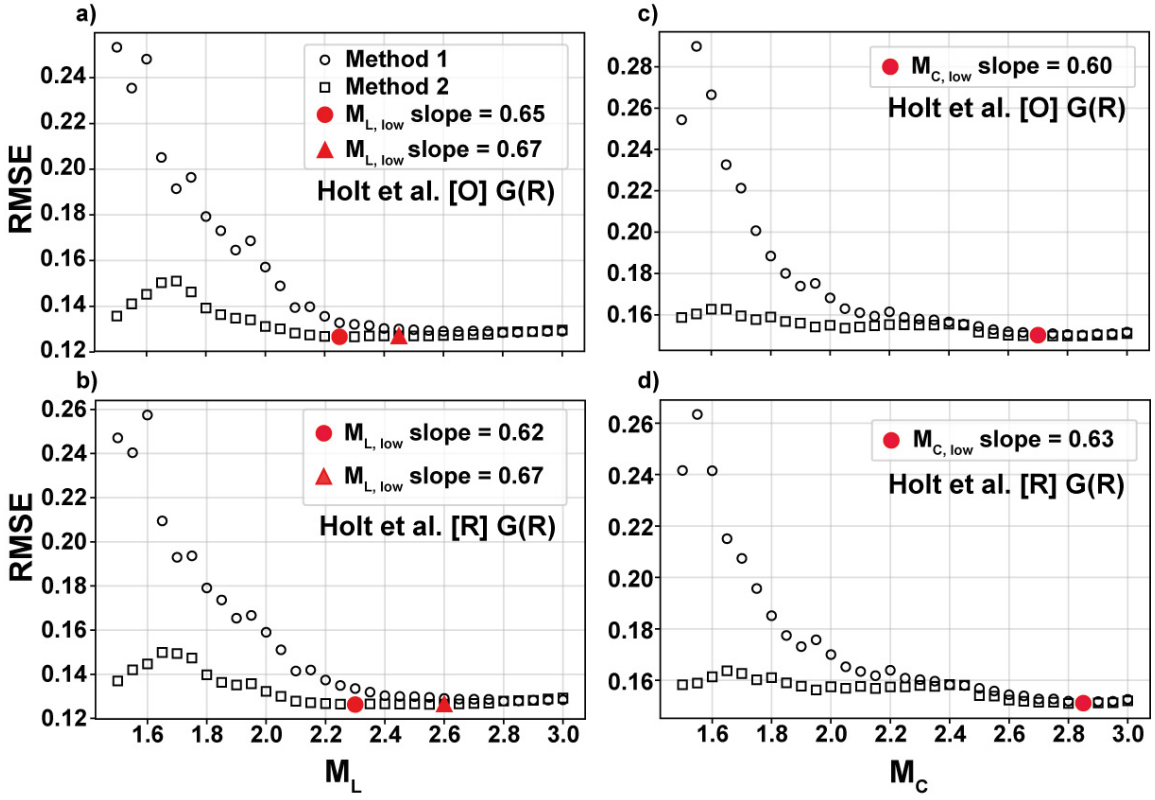

Figure 2.11 - Misfit curves of iterative searches for the optimal hinge point of bilinear relationships for M_W as a function of M_L and M_C using either the original or refined geometrical spreading model (labelled in each figure). The optimal hinge locations are highlighted with solid red circle. The bilinear relations are shown in Figure 2.10. The range of slopes for $M_{L, low}$ between hinges $2.2 < M_L < 3.0$ are 0.61-0.85 and 0.63-0.86 for subplots a) and b) respectively.

2.6 Discussion

During this study we put significant effort into modelling the attenuation of *Sg / Lg* LPSPs. This input was critical to calculating SgH Spectral M_W and is further discussed here. As mentioned in *section 2.3*, our attenuation models differ from most other models because they have slower than R^{-1} decay in the near-source region ($R_{HYP} \leq 40$). This decay is necessary to satisfy our constraint at the source while also fitting our data

in this distance range. We have argued that our dataset is actually not unique in that, had we chosen to fit the data in ways more consistent with other studies we could have observed faster than R^{-1} decay. We now substantiate that claim.

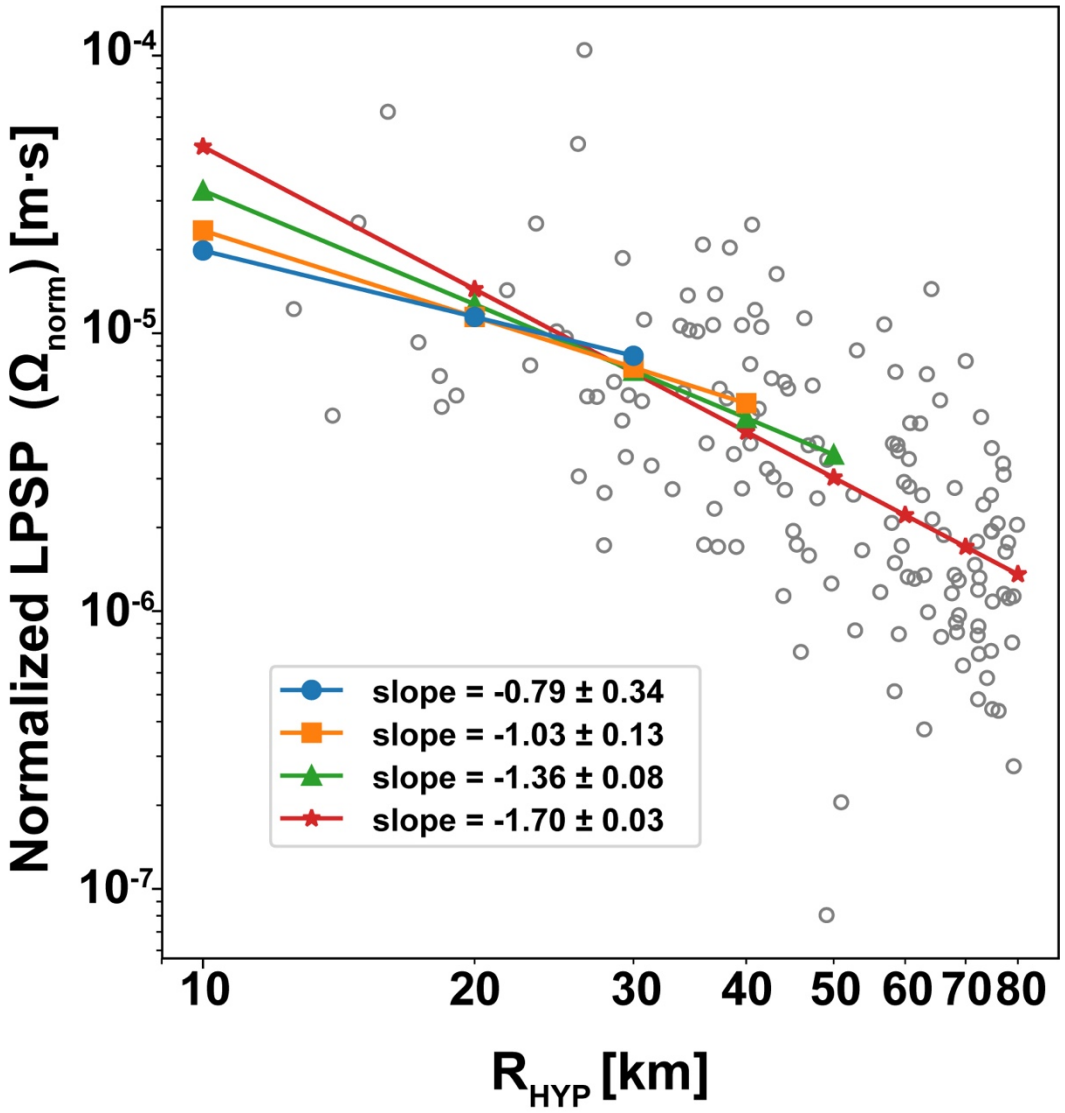

Figure 2.12 - LPSP plotted against hypocentral distance (R_{HYP}) for measurements $10 < R_{HYP} < 80$ km, only for the events in Table A1, Appendix A. Overlain are unconstrained least squares regression lines, the slopes for different distances and 95% confidence limits are indicated in the key.

Figure 2.12 shows the normalized LPSP measured for earthquakes with UUSS M_W in Table A1 (Appendix A), with four unconstrained weighted least squares regression lines overlain (weighting given by Equation 2.10 and binning width is the same as Holt et al. [O]). We fit these lines to data between R = 10 km and upper R limits that varied from 30 to 80 and provide 95% confidence limits on all slopes. Not only do we see

that is it possible to fit this data with a faster than R^{-1} decay, similar to J&H [UT]'s slope of -1.2 for a distance range of 1-50 km (Table 2.1) we also observe a significant range in slope (-0.79 to -1.56). We avoid assigning physical meaning to these slopes, but the result suggests a single slope model over the range $10 < R < 80$ km might not be adequate. We also acknowledge the potential for the underestimation of the slopes due to the sparsity of available data $R_{HYP} < 30$ km as is suggested by the large uncertainty. However, we argue that our data distribution is comparable to that of similar studies.

The models for apparent geometrical spreading (Figure 2.5 and 2.6; Table 2.1) show a $>> R^{-1}$ decay between ~ 40 and 63 - 73 km and $R^{-1.36}$ or $R^{-1.56}$ decay at R > 100 - 136 km. Edwards et al. (2011) found a similar decay of $R^{-1.4}$ at R > 120 km in Switzerland, and attributed it in part to a 'leaky' loss of long period shear-wave energy into the mantle. This is interesting because at those longer distances (R > 200 km) one might expect to observe geometric spreading closer to $R^{-0.5}$. Atkinson (2012) argues that this might be due to a velocity gradient between crust and the mantle which allows energy to escape the crustal waveguide. Instead, we only observe rates of geometrical spreading consistent with surface waves ($R^{-0.5}$) between 63-76 km to 100-136 km. Considering the length of the window used in the spectral inversion, it is possible that the distance range of this plateau is consistent with the generation of surface phases (more specifically Lg phase) which are included in our 20 s time window. The link between generation of Lg phase and relation to $R^{-0.5}$ in apparent geometrical spreading has been well documented and could be the cause here (e.g. Atkinson and Mereu, 1992; Benz et al., 1997; McNamara, 2000; Atkinson, 2012). However, this may also simply by that amplitudes in the range 40 – 63-73km are enhanced by lower crustal or upper mantle near-critical reflections (Catchings and Kohler, 1996).

For completeness we presented two sets of relations for M_W versus M_L and M_C, even though the difference between predictions of SgH Spectral M_W (for the same earthquakes) before and after refinement of the attenuation model are quite small (Figure A3, Appendix A). The 95% confidence limits of the difference between SgH Spectral M_W before and after refinement to be 0.005 magnitude units. This number is roughly 10 times smaller than the typical standard error on our mean SgH Spectral M_W predictions. Hence, the differences in the relations are most likely driven by the

differences in the sizes of the SgH Spectra M_W datasets. We successfully determined M_W for 201 earthquakes using the original geometrical spreading model and 218 earthquakes using the refined geometrical spreading model. Differences arise because, for some events, removal of outliers results in the exclusion of some calculated SgH Spectral M_W values and we require M_Ws from at least three stations. Station SgH Spectral M_W outliers depend on the choice of the geometrical spreading model since the attenuation leading to an individual measurement of Ω may vary significantly from the model due to particular path effects; e.g. multi-pathing, 3D heterogeneities, focusing/defocusing and so on (Pasyanos et al. 2009).

For the M_W - M_L relationships (Table 2.2, Figures 2.10a and 2.10b) we find that, at higher M_Ls (2.25 - 2.30 to 6.05), they have a similar slope and intercept to those found by Arabasz et al. (2016). The differences can be explained by the addition of new SgH Spectra M_W data, closer to the lower M_L limit, steepening the slope of the model. Interestingly, both the Holt et al. relations and Arabasz et al. (2016) give a slope significantly lower than 1, where it might expect that the relation is closer to 1:1. The lower magnitudes (M_L 0.96 to 2.25 - 2.30) show a significantly different M_W – M_L relation. This change at small magnitudes has a theoretical basis with the slope predicted to be 2/3 beginning somewhere between $2 < M_L < 3$ (Deichmann, 2017). Somewhere lower than this M_L range, M_L tends to decrease at a faster rate than M_W. Deichmann (2017) explains that for the small earthquakes, attenuation causes the observed pulse durations to be nearly the same, driving the systematic difference between M_W and M_L at low magnitudes. For higher magnitudes, in the range $M_L \sim$ 2-3 to M_L 4.5 and greater, theory predicts a 1:1 relation between M_W and M_L. The upper M_L limit of the 1:1 relation, and derivations from it, are controlled mainly by stress drop and the Wood-Anderson instrument response (Hanks and Boore, 1984). Observational studies have given validity to this theory (Hanks and Boore, 1984; Munafò et al., 2016; Deichmann, 2017; Malagnini and Munafò, 2018; Staudenmaier et al., 2018) and were also able to obtain slopes at lower magnitudes that match those predicted by theory.

Unlike Staudenmaier et al. (2018) we find bilinear relationships between M_W - M_C that are similar to our bilinear relations between M_W - M_L. The UUSS's M_C scale was calibrated to match M_L over the M_L range ~1 – 5 (Pechmann et al., 2006).

Consequently, the similarity between our M_W - M_L and M_W - M_C relations is not surprising. Our relationship for M_W - M_C were closer to M_W - M_L when the Holt et al. [R] model was used to calculate SgH Spectral M_W, although still significantly different within the uncertainty. This may be due to the increased scatter of M_W - M_C compared to M_W - M_L.

2.7 Conclusion

We calculated SgH Spectra M_W for 218 earthquakes with UUSS M_L, at least 216 of which had a corresponding UUSS M_C. To enable these M_W determinations, we developed a new attenuation model that was further refined for *Sg / Lg* LPSPs, which we interpret to represent apparent geometrical spreading in Utah. The attenuation model is a critical input and we took care to derive the models, so that we could robustly calculate SgH Spectra M_W to match UUSS M_Ws from moment tensor solutions.

Our geometrical spreading model should only be used for similar applications in Utah, but the procedure may be easily replicated for other regions. It is our recommendation that our method should be calibrated to moment magnitudes for natural seismic events only (i.e. no mining induced seismicity or explosions), but that is not a strict requirement, especially if *Sg / Lg* attenuation is known apriori. We found that refinement of our geometrical spreading model made little difference to our SgH Spectral M_W, likely because the two models are similar (Figure 2.7), therefore we present both models along with the corresponding, SgH Spectra M_W and scaling relationships for the sake of completeness. However, we prefer the Holt et al. [R] geometrical spreading model and corresponding SgH Spectral M_W and $M_W – M_L$ and M_C scaling relations are recommended to be used where applicable to further studies. We base our decision on the following factors: (1) Holt et al. [R] has lower uncertainty (to 95% confidence limits) on all slopes (likely owing to the larger dataset used for the regressions), (2) we were able to predict M_W for more events using the Holt et al. [R] model and (3) M_W - M_C relationship moved closer to $M_W – M_L$ (which should be similar).

Chapter 3: A Local Magnitude Scale for Yellowstone National Park, USA

Chapter 3 is constructed from a manuscript in preparation to be submitted to the *Bulletin of the Seismological Society of America*. The authors of this manuscript (correct at date of thesis submission) are James Holt (main author), James C. Pechmann, Benjamin Edwards and Keith D. Koper. The study was focussed on improving the local magnitude (M_L) scale in Yellowstone aimed at reducing uncertainty in the prediction of M_L. We also derived a new set of station corrections to complement the expansion of the network enabling more stations to be used to calculate M_L. We improve the agreement of M_L with M_W in the region and, of note, reduce the apparent uncertainty in M_L for earthquakes of M_L 3.6 and larger (which may be significant to seismic hazard studies). We comment on the agreement between the old and new scale and discuss possible uncertainty introduced because the prior distance correction was not derived specifically for earthquakes in Yellowstone. James C. Pechmann and Keith D. Koper of the University of Utah Seismograph Stations (UUSS), along with Benjamin Edwards, provided guidance for study (particularly regarding the non-parametric inversion) and how to reduce the seismic catalogue and helped draft the manuscript. Additionally, James C. Pechmann helped to design a sensitivity calculation of hypocentral distance to depth. The purpose was to determine an epicentral distance threshold, below which we must consider records only with well resolved focal depths.

Abstract

The University of Utah Seismograph Stations (UUSS) is responsible for monitoring earthquake activity in Yellowstone National Park, USA. Using a subset of their high-quality earthquake catalogue amounting to 1493 earthquakes (complied by professional seismic analysists over 24 years) we revisit the local magnitude (M_L) scale for that region. A non-parametric inversion is used to derive a new distance correction for Yellowstone, along with a set of station corrections to complement the rapid expansion of the network. We find Yellowstone has a unique and complex local attenuation structure, that is stable over 1000 bootstrap replications, warranting further investigation. Moreover, we re-calculated M_L using the new attenuation model and station corrections and made a comparison between new (YS M_L) and old (UUSS M_L)

magnitudes for 3844 earthquakes. Although the attenuation and station corrections for YS M_L and UUSS M_L (Richter, 1958; Pechmann et al., 2007) are very different, the two scales give broadly similar M_L predictions in the range 1 < UUSS M_L < 3.6. Outside of this range, however, UUSS M_L predictions are smaller by up to ~0.2 magnitude units for UUSS M_L > 3.6. Additionally, YS M_L has greater agreement with moment magnitude (M_W) ($3.1 < M_W < 4.5$) from the UUSS and Saint Louis University (SLU) than UUSS M_L does. Finally, new station corrections are compared with those last derived in 2007 and we show that the absolute value of the new corrections are generally smaller. Combined with analysis of YS M_L vs UUSS M_L residuals, this suggests that the old station corrections over corrected to account for differences between the assumed Richter (1958) model and the actual attenuation.

3.1 Introduction

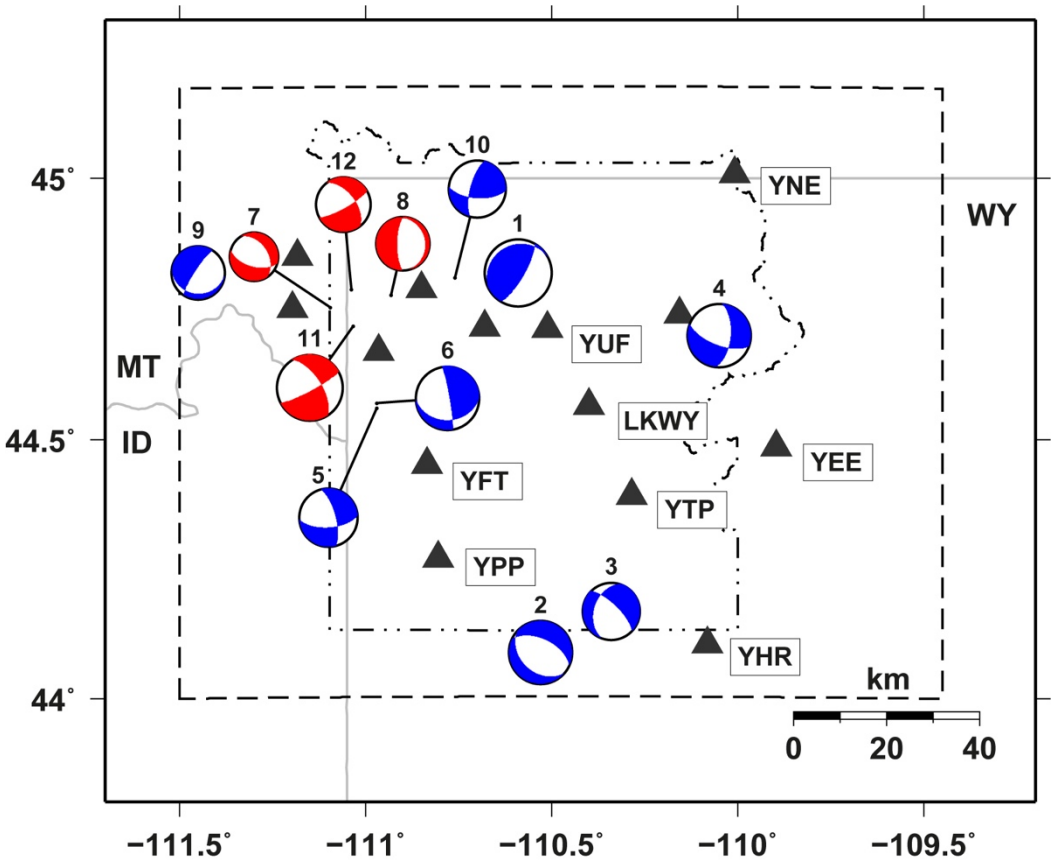

Figure 3.1 - Map of the UUSS catalogue region (dashed boundary) and the moment tensor solutions (SLU are blue and UUSS are red), given in Table 1. Also, for reference we show the Yellowstone national park region (dash-dot boundary) and the considered broadband stations (solid triangles) inside the catalogue region.

The University of Utah Seismograph Stations (UUSS), in partnership with the Yellowstone Volcano Observatory (YVO) have routinely monitored earthquakes in Yellowstone National Park region since 1984 (Pechmann et al., 2007). As part of the Advanced National Seismic Service (ANSS), the UUSS was assigned an authoritative region for the Yellowstone seismic network that spans 44.00° - 45.17° latitude and -109.45° to -111.33° longitude (Holt et al., 2019). The Yellowstone earthquake catalogue region extends slightly to the west of this to -111.50° (Figure 3.1). The Yellowstone network (WY) currently consists of a total of 30 stations. The network comprises 15 sites with broadband instruments (100 or 40 Hz), 11 of which are co-located with strong-motion instruments (100 Hz) and 5 co-located with short period instruments (100 Hz). There are a further 15 sites with single short period sensor deployments (100 Hz) (quake.utah.edu; last accessed 23rd August 2019). Here, we only use waveforms recorded at broadband or strong-motion stations, preferring the former.

Yellowstone National Park is located on the Yellowstone Plateau, a region of significant volcano-seismic activity related to its many hydrothermal features (Farrell et al., 2014; Wu et al., 2017), rising magma, abnormally high heat flow and significant rate of uplift (Farrell et al., 2009). Seismicity in the region is mixed with some related to volcanic systems, characterised by shallow (~ 5 km) spatio-temporal swarm activity (associated with the magma and fluid migration, Shelly et al., 2013) intermingled with deeper (~ 20 km) tectonic seismicity related to the Intermountain Seismic Belt (ISB, Smith and Arabasz, 1991), which crosscuts the Yellowstone Plateau (Christiansen et al., 2007). We consider all earthquakes recorded by the Yellowstone network in this study, regardless of their origin. Shear-wave attenuation on the Yellowstone Plateau has been shown to be significantly different from the surrounding regions. Early evidence was shown by the relatively low V_P/V_S ratios in Yellowstone (Chatterjee et al., 1985). More recently, Lawrence and Prieto (2011) and Bowden et al. (2017) produced seismic attenuation maps (for periods between 8 – 32 s) of the Western US and, in each case, Yellowstone was highlighted as a region of anomalous attenuation. Jeon and Herrmann (2004) looked at shear-wave attenuation in Utah and Yellowstone regions and found higher attenuation, in Yellowstone, $Q(f) = 140f^{0.70}$, compared to Utah, $Q(f) = 160f^{0.75}$. Jeon and Herrmann (2004) noted that their Q is averaged over the whole upper crust in Yellowstone. They go on to explain that studies by Clawson

(1989) have shown Q and can be much lower (< 50) and their average ($Q(f) = 140f^{0.70}$) includes regions outside of the caldera with lower Q more similar to Utah.

Yellowstone is also a region of significant hazard (Christiansen et al., 2007) so the UUSS produces seismic catalogues; these are mostly made up of local magnitude (M_L) and coda-duration magnitude (M_C). Though the catalogue is mainly dominated by M_C, those magnitudes are calibrated to match the M_L predictions (over the range $0.5 \leq M_L \leq 5$) making M_L integral to UUSS operations and by extension, the local hazard assessment. Currently, the UUSS calculates M_L using the following equation (Richter, 1935; Richter, 1958):

$$M_L = \log_{10}(A) - \log_{10}(A_0) - S \tag{3.1}$$

where A is half of the maximum horizontal peak-to-peak amplitude (p-to-p) (in mm, averaged over NS and EW components) of a synthetic Wood-Anderson record, $-\log_{10}(A_0)$ is the distance correction and S is a station correction. The most recent station corrections were derived by Pechmann et al. (2007) to transition M_L determinations smoothly from paper to digital records. They used the Dugway station as a reference because it had a WA seismometer and a newer digital broadband (BH) station they could use for comparison. For $-\log_{10}(A_0)$ the UUSS used the distance correction defined by Richter (1935, 1958) that was arbitrarily fixed to 3 at an epicentral distance (R_{EPI}) of 100 km. UUSS has used Richter's correction since operations began in 1965 to the present because both Grizcom and Arabasz (1979) and Pechmann et al. (2007) separately confirmed the correction was valid for earthquakes covering the entirety of the ISB. Pechmann et al. (2007) found this was true even with additional broadband data, over range 0 – 600 km. However, from their analysis it was difficult to see if it was strictly valid for Yellowstone, even though the associated seismicity made up a quarter of that catalogue. A cursory study looked at only Yellowstone, but it was determined that the difference was insignificant to M_L predictions across the entire ISB (after the derivation of station corrections), likely because there were only a few stations that could be used for M_L determination there. Pechmann et al. (2007) also noted that they would have preferably used hypocentral distance (R_{HYP}) over R_{EPI} had they recalibrated their distance correction but were unable due to insufficient data with well resolved focal depths.

Today, UUSS has a high-quality catalogue for the Yellowstone region (which has well constrained focal depths and superior network coverage), that was compiled by professional seismic analysists over more than 24 years. With this greatly expanded dataset we revisit the question of how appropriate the Richter (1958) distance correction is for Yellowstone; where we hypothesise attenuation may be different from Utah (where most of the UUSS network is based) and the rest of the ISB. Also, to complement the expansion of the Yellowstone network since 2007, we derive new station terms, *S,* for 16 stations, 13 from the Yellowstone network and 3 from other networks routinely used by the UUSS. We use the 'non-parametric' inversion method described by Savage and Anderson (1995) to invert our dataset for the distance correction, M_L and *S* in Yellowstone. To maintain continuity between M_L in Utah and Yellowstone, new *S* are fixed relative to some stations with known corrections. The new $-\log_{10}(A_0)$ model is compared with the Richter (1958) and Hutton and Boore (1987) models and we find that using Richter (1958) attenuation tends to underpredict large and small magnitudes, compared to the new scale. Furthermore, our improved magnitude scale for Yellowstone has a closer to 1:1 agreement with existing M_W ($3.1 < M_W < 4.5$) than the previous scale. Finally, for robustness we perform the inversion for 1000 bootstraps with 10% random replacement to report uncertainty on the distance correction, magnitudes and station corrections.

3.2 Data and Processing

The initial UUSS Yellowstone catalogue used for this study spans from Sept 1994 – Dec 2018 and consists of 29199 p-to-p amplitudes (mm) from 7001 earthquakes. All earthquakes in the Yellowstone catalogue have been relocated using 1D P-wave velocity model, which was generalised from a 3D model derived by Smith and Husen (2004). The p-to-p amplitudes recorded at 19 out of 20 stations were obtained from synthetic WA seismograms and from paper records recorded at one station (BUT, an electronically simulated WA seismometer). The UUSS pre-processing procedure to obtain synthetic WA records is summarised in Pechmann et al. (2007) as the following: (1) demean, (2) apply 5% cosine taper, (3) append 5 seconds of zeros to the end of the record, (4) deconvolve instrument response, (5) convolve standard WA response; static magnification (V) = 2800, damping (ζ) = 0.8, free period (T_0) = 0.8 s. They use the standard WA response, rather than V = 2080, ζ = 0.69, T_0 = 0.8 s (Uhrhammer and

Collins, 1990) and accept a trade-off with station corrections, as we also do in this study for continuity. This procedure has remained broadly similar since they began using Jiggle software (http://pasadena.wr.usgs.gov/jiggle/; last accessed 17/09/19) for routine analysis in October, 2012 and no obvious discontinuities were introduced between pre and post transition data. The p-to-p amplitudes may be picked from anywhere on the seismogram, this makes it possible to pick P-waves (but this is rare). Most often they require a signal-to-noise ratio (SNR) ≥ 2, but sometimes lower at the discretion of the analyst. Finally, p-to-p is taken as the largest peak to adjacent trough distance ignoring any perturbation less than 10% of the entire amplitude.

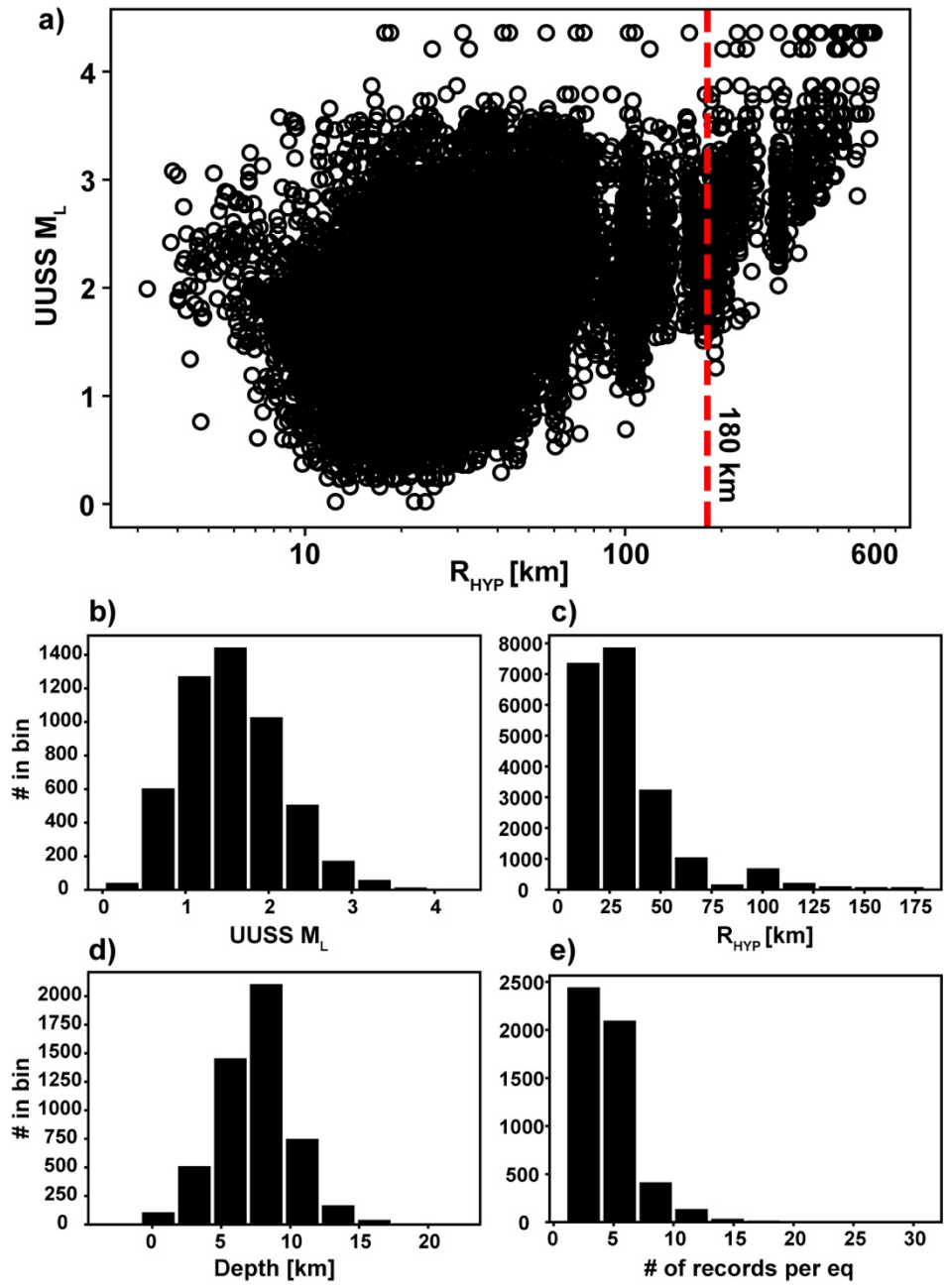

Figure 3.2 - Initial catalogue considered in the study. Subplot a) shows the magnitude-distance relation. The red line shows the maximum distance considered for the remainder of the study. Subplot b) is the magnitude distribution, c) is the hypocentral distance distribution, d) is the depth distribution (relative to sea level) and e) shows the number of records per catalogue event.

Although dense, the Yellowstone network only spans ~1° of latitude and longitude or roughly 111 x 111 km (Figure 3.1). This is evident in the magnitude - distance (M-D) plot (Figure 3.2a), made using the existing UUSS local magnitudes (UUSS M_L), which shows that most events tend to be recorded at distances of < 60 km (Figure 3.2c). We include only events with 'well-constrained' focal depths for the M-D distribution. Our criteria for well-constrained depths (h) are: (1) the closest recording station (D_{MIN}) is within 1 focal depth corrected to the average surface elevation (from sea level) (D_{MIN} / [h + 2.4 km] $\leq$ 1), or $R_{EPI} \leq 5$ km and (2) the depth error is no larger than ± 2 km. Also noteworthy is the relatively short range of magnitudes in the dataset ($0.02 \leq$ UUSS $M_L \leq 4.36$; Figure 3.2b), their shallow focal depths (median ~ 8 km; Figure 3.2d), which are relative to sea level, and how well recorded events are (most between 2-6 records per earthquake; Figure 3.2e). On the basis of the M-D distribution we decided to limit our investigation to $R_{HYP} \leq 180$ km since at that distance we see a significant shortening of UUSS M_L and large data gaps. Our reasoning is that the path effects beyond 180 km would be governed by larger earthquakes that have similar paths to the more distant stations—mostly stations to the south, in Utah—thus introducing bias to our result.

We impose quality control constraints to our catalogue that: (1) records at $R_{EPI} \leq 50$ (see Appendix B for comments) must have a well-constrained focal depth (so R_{HYP} is reliable in this range), (2) the SNR ≥ 2 and (3) each earthquake must be recorded by a minimum of 3 stations. However, we make an exception for any earthquake from the additional quality control criteria if it has an existing moment magnitude (M_W) solution. This was a strict requirement because we wanted to compare the existing and new M_L with M_W. The M_W catalogue (Figure 3.1; Table 3.1) was compiled from the UUSS moment tensor catalogue (UUSS M_W; Whidden and Pankow, 2012; https://quake.utah.edu/regional-info/earthquake-catalogs/moment-tensor-solutions; last accessed 21st August 2019) and the Saint Louis University (SLU) North America moment tensor catalogue (SLU M_W; http://www.eas.slu.edu/eqc/eqc_mt/MECH.NA/; last accessed 21st August 2019). Imposing the above reduces the catalogue to 3967 earthquakes, 12 of which have either a SLU M_W or both SLU M_W and UUSS M_W (we prefer UUSS M_W when available because they are all manually reviewed).

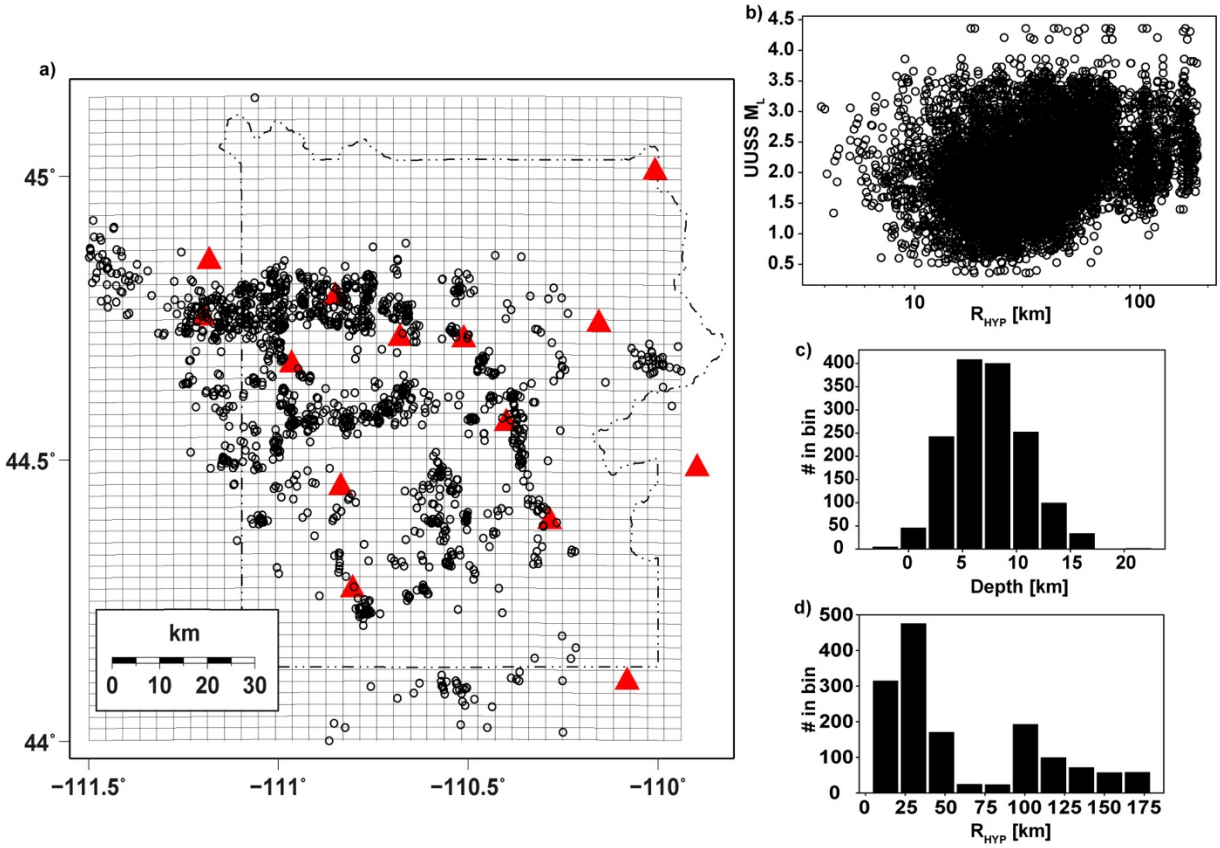

Figure 3.3 – Subplot a) is a Seismicity (empty circles) map for the final earthquake catalogue after quality control and geographic weighting. The broadband stations (solid triangles) and the Yellowstone National Park boundary (inside dot dashed region) from Figure 1 are plotted for reference. The gridded region was defined by the extremal surface locations of the earthquakes and split into 55 even lines in latitude and 35 even lines of longitude. Subplot b) is the Magnitude-Distance distribution of final earthquake catalogue. Subplots c) and d) are the depth (relative to sea level) and distance distributions of the final earthquake catalogue. The drop around 75 km in subplot d) is likely caused by the sharp drop in station coverage outside of the Yellowstone region.

Next, we focus on providing a more even geographic distribution of seismicity, so the solution is not overwhelmed by many similar propagation paths. This is of particular importance in this catalogue since it is dominated by seismic swarms (Farrell et al., 2009). Firstly, we only attempt to reduce the spatial bias, since the time dependence has lesser importance to M_L. Furthermore, we can narrow down to only latitude and longitude weighting because the depth distribution appears to be normally distributed (Figure 2c). We first create a square domain whose boundaries are determined by the min and max latitudes and longitudes of the catalogued earthquake locations. Next, the square is split evenly into x slices of longitude and y slices of latitude, to create a grid. Then, we search over the gridded domain and check if sub-grid (x, y) has more than a threshold number of earthquakes (N_T); if so, the number of earthquakes is reduced to N_T. To reduce to N_T, we prefer to keep earthquakes if they have an M_W, or alternatively,

are ≥ to some threshold magnitude (M). If we reduce the number of earthquakes left in the grid (n) to < N_T earthquakes, we sort the removed earthquakes from highest to lowest number of recordings and pick N_T - n earthquakes from the best recorded. After some manual balancing, we found that the ideal parameters were x = 35, y = 55, N_T = 10 and M = 3. Our decision to have more slices in latitude was based on the fact that seismicity is focussed along an E-W striking strip toward the north of the national park area (Figure 3.3) and thus, helped reduce events there without removing too many earthquakes. Ultimately, using our geographic reduction algorithm, the dataset was reduced from 3967 to our final subset of 1493 earthquakes. Figure 3.3 shows the catalogued seismicity map (after the initial quality control criteria was applied) and gridded search domain with the earthquakes that remained (black circles) after spatial reduction. We also include the same map but with the removed earthquakes in Appendix B (Figure B1).

3.3 Non-Parametric Inversion

The 'non-parametric' method is was used in Savage and Anderson (1995) as a way to estimate $-\log_{10}(A_0)$ at distance nodes (n) via linear interpolation and simultaneously solve for M_L and S, without an assumed functional form for the distance correction. The 'non-parametric' equation is formulated by rewriting Equation 3.1 as:

$$\log_{10}\left(A_{\hat{n},i,j}\right) = -a_n \log_{10}(A_0) - a_{n+1}\log_{10}(A_0) + b_i M_{L,i} - c_j S_j \qquad (3.2)$$

$$a_n = \frac{R_n - r_{\hat{n},i,j}}{R_{n+1} - R_n}$$

Here, $A_{\hat{n},i,j}$ is the amplitude (mm) of earthquake i, recorded at station j, for bin $\hat{n}$ (records between node and n+1). a_n is a coefficient of linear interpolation to node n at hypocentral distance (R_{HYP}), R_n and $a_{n+1} = 1 - a_n$. $M_{L,i}$ is the local magnitude of event, i, and S_j is the station correction of station j. Finally, b_i and c_j are dummy variables that are equal to 1 or 0 depending on if the event - station pair exists or does not exist, respectively. Equation 3.2 is rearranged from Equation 3.1 by making $-\log_{10}(A_0)$, $M_{L,i}$ and S_j model parameters. They can then be inverted for in linear system of equations, $\mathbf{d}=\mathbf{G}\cdot\mathbf{m}$ (see Equation B.4, Appendix B). The number of nodes (N) and node spacing ($R_{n+1} - R_n$) can be arbitrary. Our node spacing was intentionally set to be similar to Richter (1958), hereafter referred to as R58, corrected to R_{HYP} assuming h = 10.4 km (the median catalogue depth) using Equation 3.3:

$$R_{HYP} = \sqrt{R_{EPI}^2 + 10.4^2} \tag{3.3}$$

We invert for three additional R_{HYP} nodes at 1, 5 and 75 km that are not in the Richter (1958) table as the first two did not exist because it was defined in terms of R_{EPI} and the node at 75 km was not present. For the latter, it is unclear if this was an intentional decision by Richter (1935). Nevertheless, data coverage in Yellowstone is sufficient to resolve attenuation at all of these hypocentral distances via interpolation. We round R_{HYP} to the nearest whole number because we cannot be more precise than R58. The data matrix is then organised into distance bins ($\hat{n}$), for a total number of bins ($\widehat{N}$) = N – 1, then ordered by event (i) and finally by unique station (j).

To constrain the inversion, it is typical to anchor $-\log_{10}(A_0)$ to a reference value of the Richter (1958) equation, for which most studies choose $-\log_{10}(A_0)$ = 3 at 100 km (e.g. Bakun and Joyner, 1984; Savage and Anderson, 1995; Brazier et al., 2008; Di Bona, 2016). However, Hutton and Boore (1987), hereafter referred to as HB87, suggested that this anchor should be $-\log_{10}(A_0)$ = 2 at 17 km. Their reasoning is twofold: (1) to allow more freedom to match regional attenuation at longer propagation distances and (2) because they suggest that R58 incorrectly assumed a $1/R^2$ (R_{EPI} < 30 km) geometric spreading and their average focal depth was too deep. However, Pechmann et al. (2007) argued that R58 mentions no assumption about geometric spreading; adding that it was justified empirically and, no matter the case, much faster than 1/R geometric spreading in the near-field is not unreasonable (e.g. Frankel et al., 1990). Furthermore, Alsaker et al. (1991) found that using the HB87 anchor introduced an apparent difference of attenuation in the Norwegian distance correction. They recommended that the anchor should be chosen with care and ensure it reflects observed attenuation of the desired region, at an appropriate distance range.

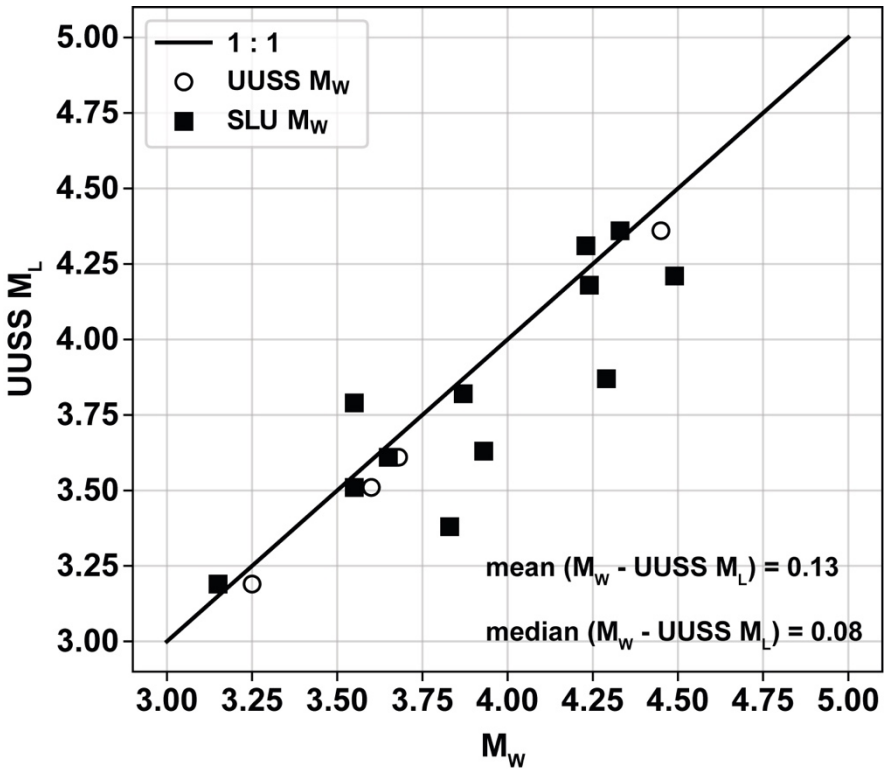

Figure 3.4 – A plot comparing the UUSS M_L with M_W (SLU and UUSS) for 12 earthquakes in Yellowstone. The mean and median magnitude residuals are calculated using the UUSS solutions if available, otherwise the SLU solution is used.

To assist in choosing an appropriate anchor distance we compare *A* with the R58 and HB87 attenuation. However, we suspected that the current UUSS M_L would not equate to a true magnitude 3 earthquake. M_W is therefore used as a base of comparison, since M_W and M_L should have close to 1:1 mapping at this magnitude (Deichmann, 2006, 2017, 2018) and we trust M_W. Additionally, UUSS M_L was plot against M_W (Figure 4) for the 12 earthquakes (Figure 3.1; Table 3.1) that have moment tensor solution in Yellowstone to see what the current relationship was like. Figure 3.4 shows that UUSS M_L appear to be linearly offset from the 1:1 line and appear to be systematically underestimating M_W. Taking the median of the differences between preferred M_W and UUSS M_L (Table 1) yields 0.08 magnitude units (m.u.). We take the median since it is less sensitive to potential outliers. Adding 0.08 m.u. to UUSS M_L gives $M_W \simeq$ UUSS M_L + 0.08. The average standard error of UUSS M_L is ~0.1 (Arabasz et al., 2016), so we look for *A* from earthquakes between 2.98 ≤ UUSS M_L ≤ 3.18. Next, the distance corrections are converted to horizontal WA motion for a theoretical M_W / M_L = 3 earthquake (by adding 3 to each curve), so that both equations are equal to 0 at 100

km. Figure 3.5 shows the comparison between A and the attenuation functions. Most notably, it is clear that for $R_{HYP} \leq 20$ HB87 is very different to the observed attenuation in Yellowstone. In fact, at the suggested anchor point, HB87 is ~ 0.4 log-mm smaller than observed. Had we chosen this anchor, likely this would have forced an apparent increase of attenuation, thereby increasing M_L by the same amount (0.4 m.u.) on average. Interestingly, A does have good agreement with HB87 around R_{HYP} = 50 km, as was also found in Alsaker et al. (1991). It can be inferred from Figure 3.5 that for an M_W 3 earthquake in Yellowstone, A ~ 1.4 mm at R_{HYP} ~ 18 km from the source, the same as R58. We therefore choose to anchor our scale to R58 at R_{HYP} = 18 km (R_{EPI} = 15 km, $-\log_{10}(A_0) = 1.6$). Anchoring to R58 gives exact continuity with the previous M_L scale and is close (in distance) to the suggested HB87 anchor.

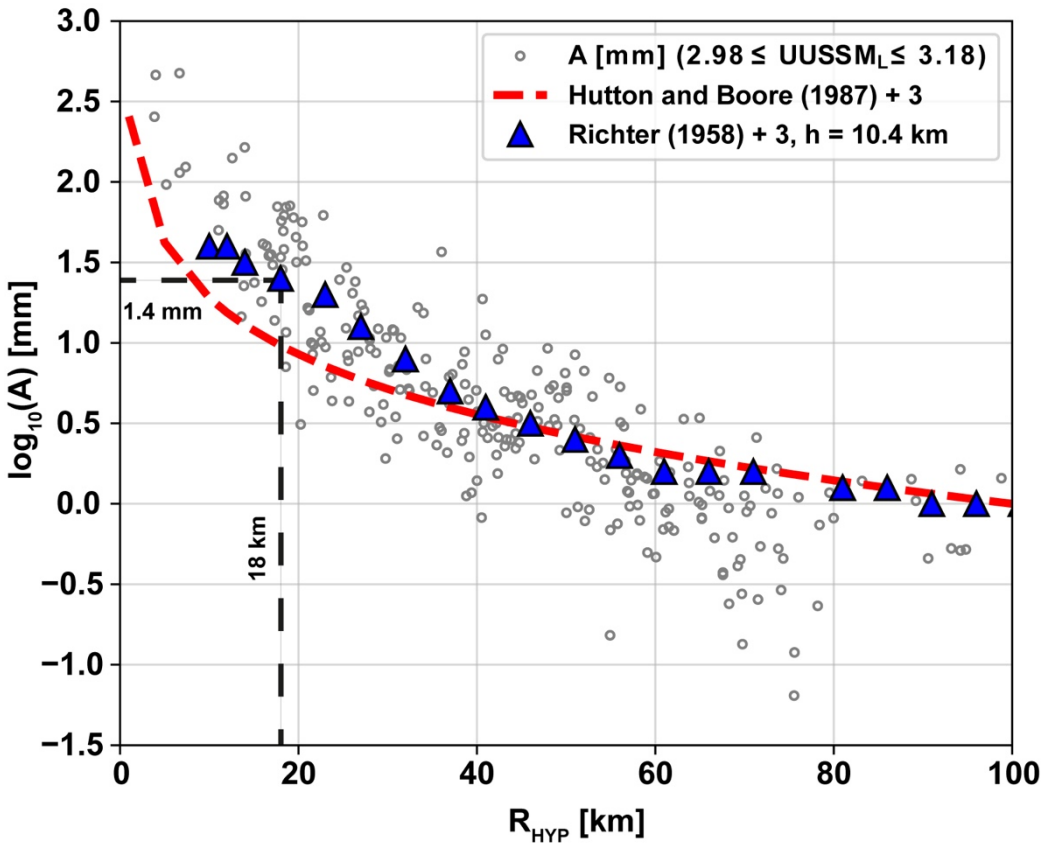

Figure 3.5 – Comparing the half p-to-p amplitudes for 2.98 < UUSS ML < 3.18 with expected p-to-p amplitudes (over distance) for a magnitude 3 earthquake. We use models from Hutton and Boore (1987) (red dashed line) and Richter (1958) (solid triangles), adjusted to hypocentral distance assuming h=10.4 km and corrected to A as a function of distance for an M_W 3 earthquake. The black dashed lines mark the location of reference value of Richter (1958) chosen to anchor the inverted distance correction to.

Table 3.1 –Mws derived from moment tensor solutions complied from UUSS and SLU catalogues for the Yellowstone region.

ID	UTC	SLU M_W	UUSS M_W	Preferred M_W	UUSS M_L	Depth [km]
01	2000/11/24 04:20:06	4.49	-	4.49	4.21	4.10
02	2003/08/21 07:46:54	4.23	-	4.23	4.31	4.20
03	2006/05/18 10:16:21	3.87	-	3.87	3.82	3.84
04	2008/03/25 11:59:38	4.24	-	4.24	4.18	4.21
05	2010/01/19 21:32:31	3.93	-	3.93	3.63	3.90
06	2010/01/21 06:16:19	4.29	-	4.29	3.87	4.26
07	2012/08/07 05:07:15	3.15	3.25	3.25	3.19	5.00
08	2012/09/05 22:52:51	3.55	3.60	3.60	3.51	12.00
09	2013/06/06 02:09:21	3.55	-	3.55	3.79	3.52
10	2014/06/03 09:33:27	3.83	-	3.83	3.38	3.80
11	2017/06/16 00:48:46	4.33	4.45	4.45	4.36	15.00
12	2017/07/18 20:31:10	3.65	3.68	3.68	3.61	12.00

The UUSS already had station corrections for some stations within the Yellowstone network and the surrounding area (ten exactly) after calibration by Pechmann et al. (2007). Figure 3.6 shows a map of all stations that recorded our final subset earthquakes and their corresponding ray paths. We decided that four stations, which are sufficiently far away from WY and that already have corrections (solid triangles / square in Figure 3.6) should be fixed in the final inversion. This would grant us the ability to increase the range of the distance correction outside of the Yellowstone network without introducing significant bias to the distance correction or magnitudes, because the station density drops significantly outside of Yellowstone. All other station corrections are left free and are shown in Figure 3.6 as triangles with no fill. We impose a further constraint on all station corrections by forcing their sum to 0, $\sum_{j=1}^{J} S_j = 0$ (e.g. Savage and Anderson, 1995; Miao and Langston, 2008; Bindi et al., 2019).

To apply the constraints, we simultaneously solve for system of constraint equations $\mathbf{h} = \mathbf{F}\cdot\mathbf{m}$ ($\mathbf{h}$ are the constraint values, $\mathbf{F}$ are the constraint coefficients) and $\mathbf{d} = \mathbf{G}\cdot\mathbf{m}$ using the method of Lagrange multipliers (Menke, 1984). The final system of equations is solved in a least-squares sense via Singular Value Decomposition (SVD). Finally, we require that the numerical second derivative is small and find a weight of 20 observations provides ample smoothing, similar to Savage and Anderson (1995).

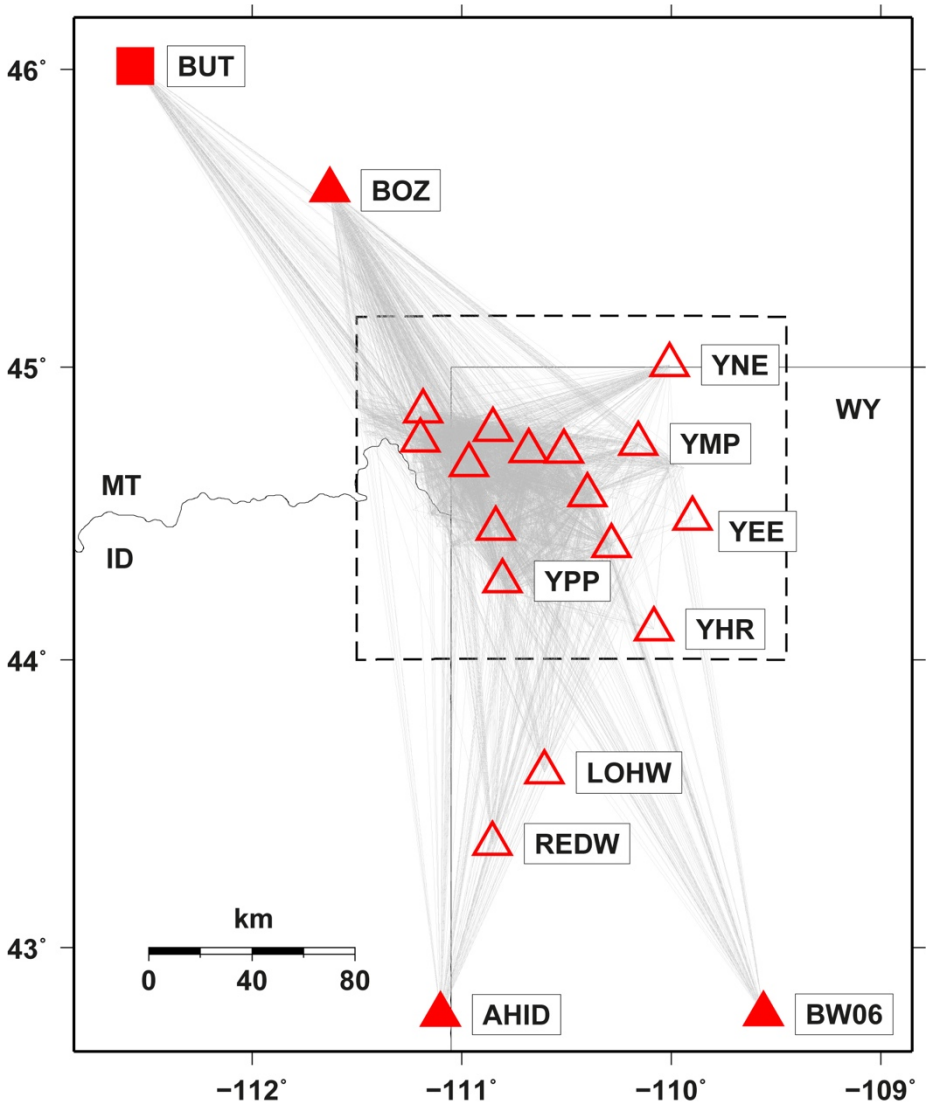

Figure 3.6 – Map of all stations used for the final inversion. As in Figure 3.1 the Yellowstone catalogue region is bounded by the black dashed line. The red triangles represent the broadband / co-location strong motion stations and the square is an electronically simulated WA seismometer. The ray paths to each station are also plotted as grey lines. Stations that have fill had their station corrections fixed to values derived by Pechmann et al. (2007). Conversely, station corrections for stations with no fill were left free in the inversion.

3.4 Results

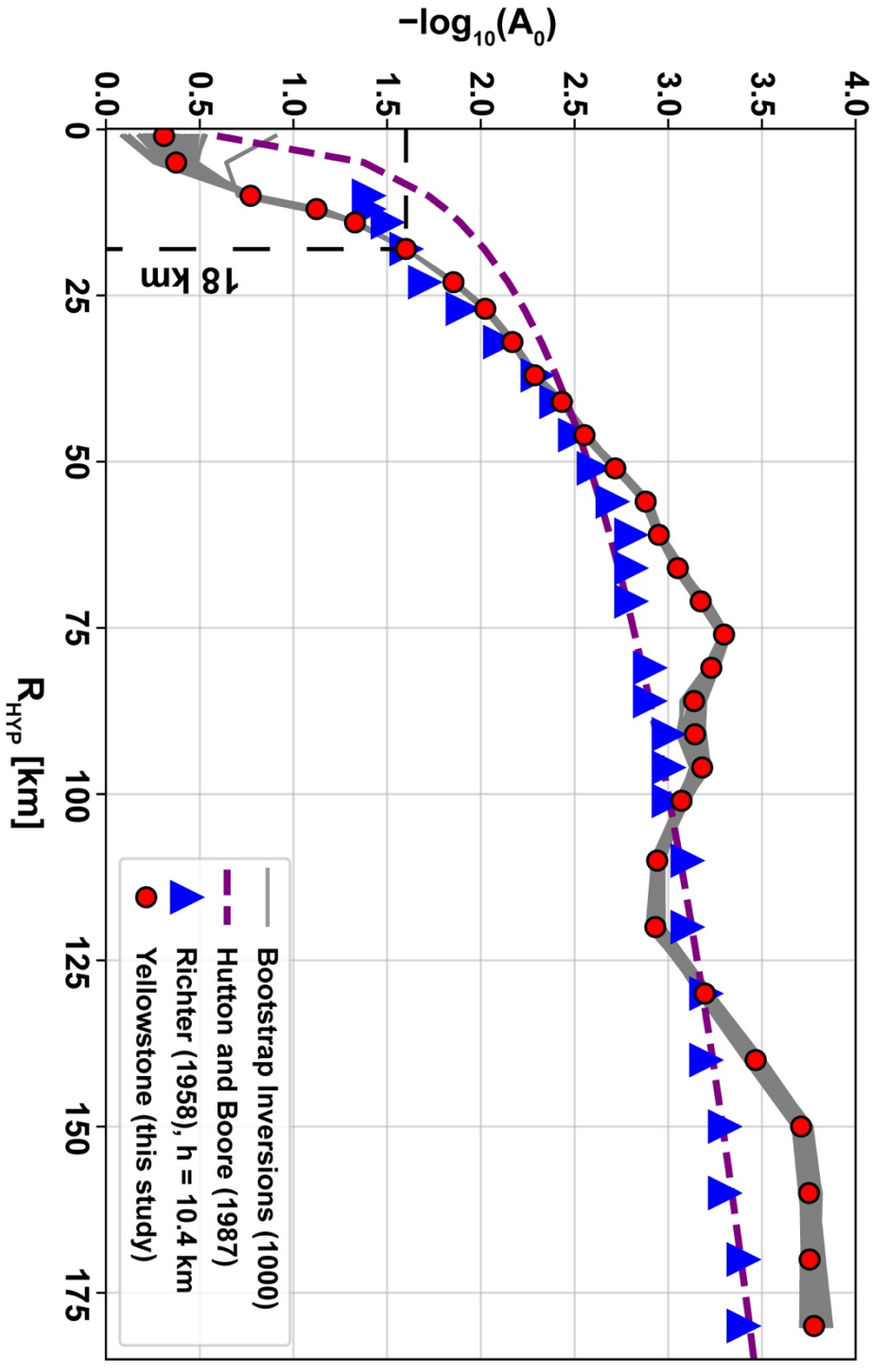

Figure 3.7 – Comparison of the Yellowstone distance correction obtained from the final inversion (red circles) against Hutton and Boore (1987) and Richter (1958). The Yellowstone distance correction nodes were chosen to match Richter (1958), except for one additional node at R_{HYP} = 75 km. Also plotted are 1000 inversions from bootstrap replications with 10% random replacement of the data. The anchor point of the inversion is marked by the dashed black lines.

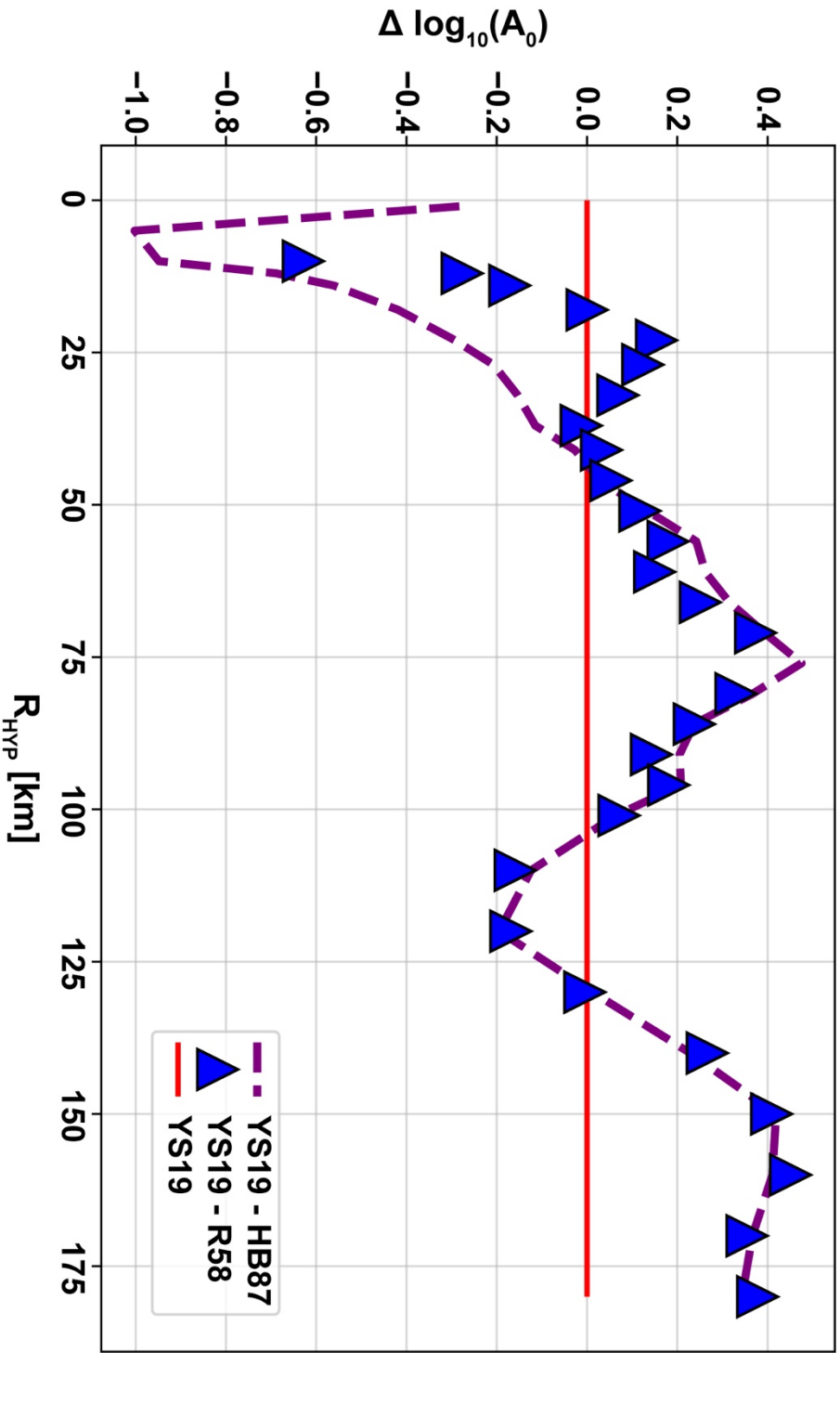

Figure 3.8 – Difference between the YS19 and HB87 (dashed line) / R58 (solid triangles) respectively. The red line corresponds to where the distance corrections match exactly with YS19.

Figure 3.7 shows the final non-parametric attenuation curve for Yellowstone, hereafter referred to as YS19, from the inversion. We gauge uncertainty on the model by performing 1000 bootstrap replications of p-to-p amplitudes with 10% random replacement (Efron, 1979) and they are plot behind YS19. We also plot R58 and HB87 on Figure 3.7 for comparison and the absolute differences between YS19 and R58 / HB87 ($\Delta \log_{10} A_0$) on Figure 3.8. Plots of just the Yellowstone attenuation curve and the data corrected to $\log_{10} A_0$ can be found in the Appendix B (Figure B2). HB87 and YS19 show the greatest difference (up to ~ 1 m.u. larger) at $R_{HYP} < 45$ km. In the same distance range, YS19 is more similar to R58 overall, except for $R_{HYP} < 18$, where R58 is larger (up to ~ 0.65 m.u.). At $R_{HYP} > 45$ km the relationship between YS19 and R58 / HB87 is essentially the same since HB87 is effectively a smoothed average of R58 between 45 – 180 km, so we focus on the relationship with R58 here. In that range YS19 is the largest by up to 0.4 m.u. or ~ 0.2 m.u. on average. Most notably, YS19 is smaller than R58 between ~110 – 130 km, in a larger region ($75 < R_{HYP} < 120$) showing a sharp apparent reduction of attenuation.

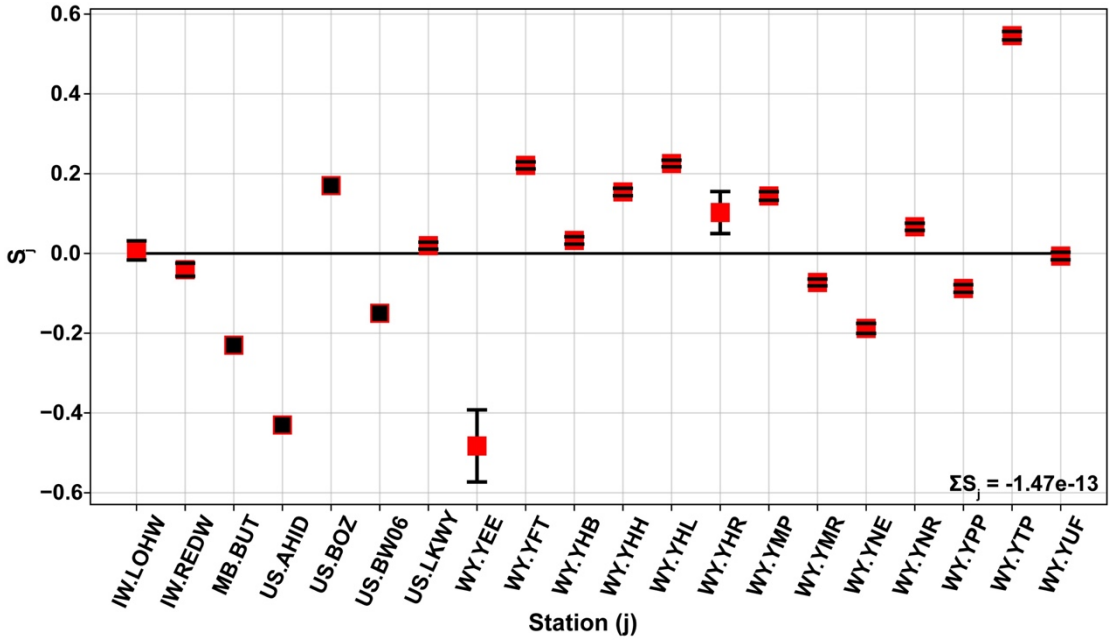

Figure 3.9 – Station corrections calculated in the final inversion (red squares) and the fixed station corrections (black squares). The error bars for the free station corrections were calculated via bootstrapping.

Next, we recomputed M_L for the subset of 3967 Yellowstone earthquakes (YS M_L) that passed our quality control criteria *(see Data and Processing)*, using YS19 and the newly derived station corrections (Figure 3.9; Table B1). The station corrections

shown in Figure 3.9 also show ± 1 standard deviation (error bars) from bootstrapping and the histograms are shown in Appendix B (Figure B3). We used the station corrections given by the final inversion (red squares in Figure 3.9) to calculate YS M_L. Figure 3.10a shows the comparison between YS M_L and UUSS M_L as a 2d histogram

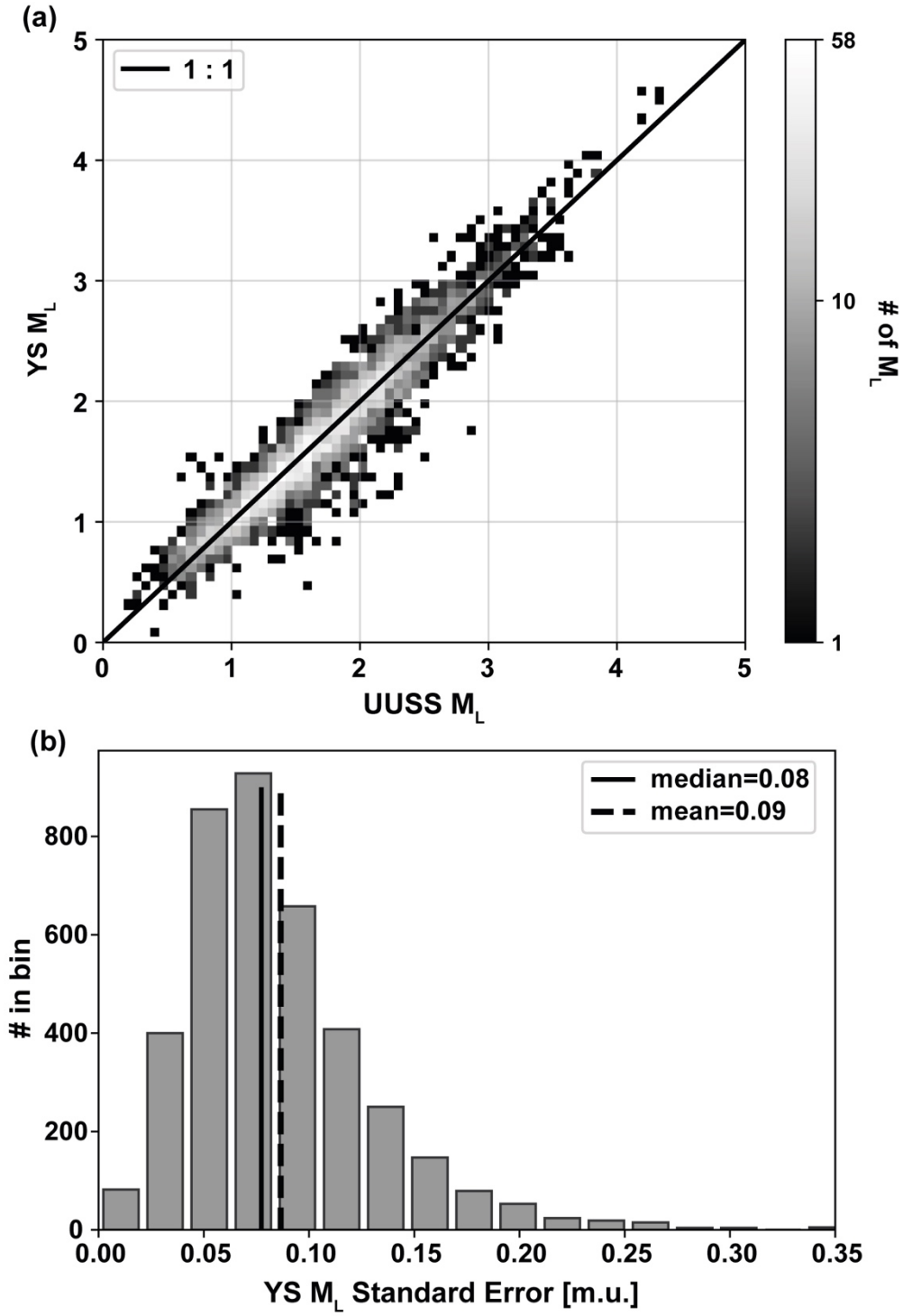

Figure 3.10 – Subplot a) shows a 2d histogram of local magnitude re-calculated for Yellowstone earthquakes, using the YS19 attenuation model and station corrections (YS M_L) vs local magnitude calculated by the UUSS following Pechmann et al. (2007) (UUSS M_L). Subplot b) is a histogram of the standard error of YS M_L, truncated at 0.35 magnitude units (m.u.).

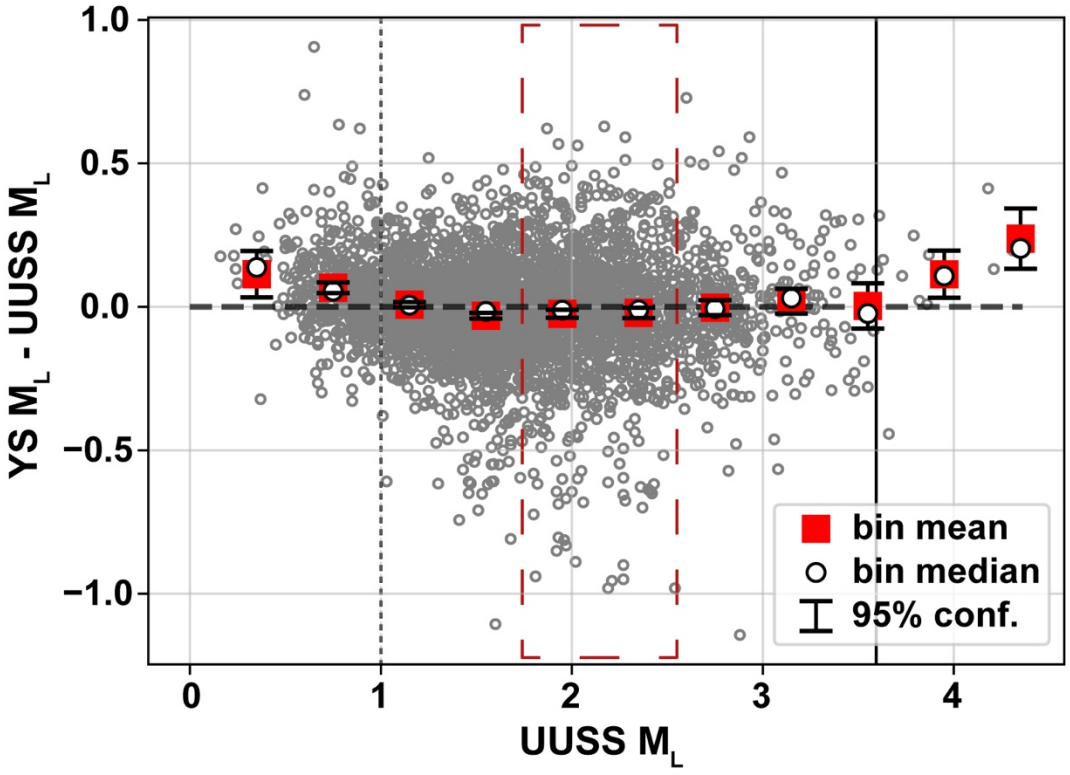

Figure 3.11 – YS / UUSS M_L magnitude residuals, absolute (grey circles) and binned means (red squares). The bins cover the range 0.1 < UUSS M_L < 4.4 and are spaced 0.4 m.u apart. The error bars show 95% confidence limits for each bin and the white circle shows the bin median. The vertical dashed line marks a boundary (zone 1) before which YS M_L is larger than UUSS M_L. The red dashed box represents a region where UUSS M_L and YS M_L are almost equal (zone 2). The vertical solid line marks the boundary beyond which YS M_L is larger than UUSS M_L (zone 3).

and Figure 3.10b shows a 1d histogram of the measured standard error in YS M_L. The mean standard error is 0.1 m.u. and, on this basis, we decided to reduce our dataset to events that had a standard error < 0.2 (~95% limits on the mean), resulting in a reduction of the catalogue from 3967 to 3844 events. We use the reduced catalogue for all further analysis. It appears that in the range 1 < UUSS M_L < 3.6, both M_L ordinates closely follow a 1:1 relationship. However, outside of this range (UUSS $M_L \leq 1$ and UUSS $M_L \geq 3.6$) YS M_L tends to be higher than UUSS M_L on average. This is clearer when looking at the difference between YS M_L and UUSS M_L, which is presented in Figure 3.11. In this figure, the event magnitude residuals are plot. The residuals were binned between 0.1 < UUSS M_L < 4.6 with 0.4 m.u. to make the plot more interpretable. We plot bin means, bin medians and 95% confidence limits (error bars) on the mean. As in Figure 3.10a the binned means in Figure 3.11, between 1 < UUSS M_L < 3.6, show very close to 1:1 relationship and show significant differences (to within 95% confidence) outside of those limits. For UUSS $M_L \leq 1$ (thin dashed

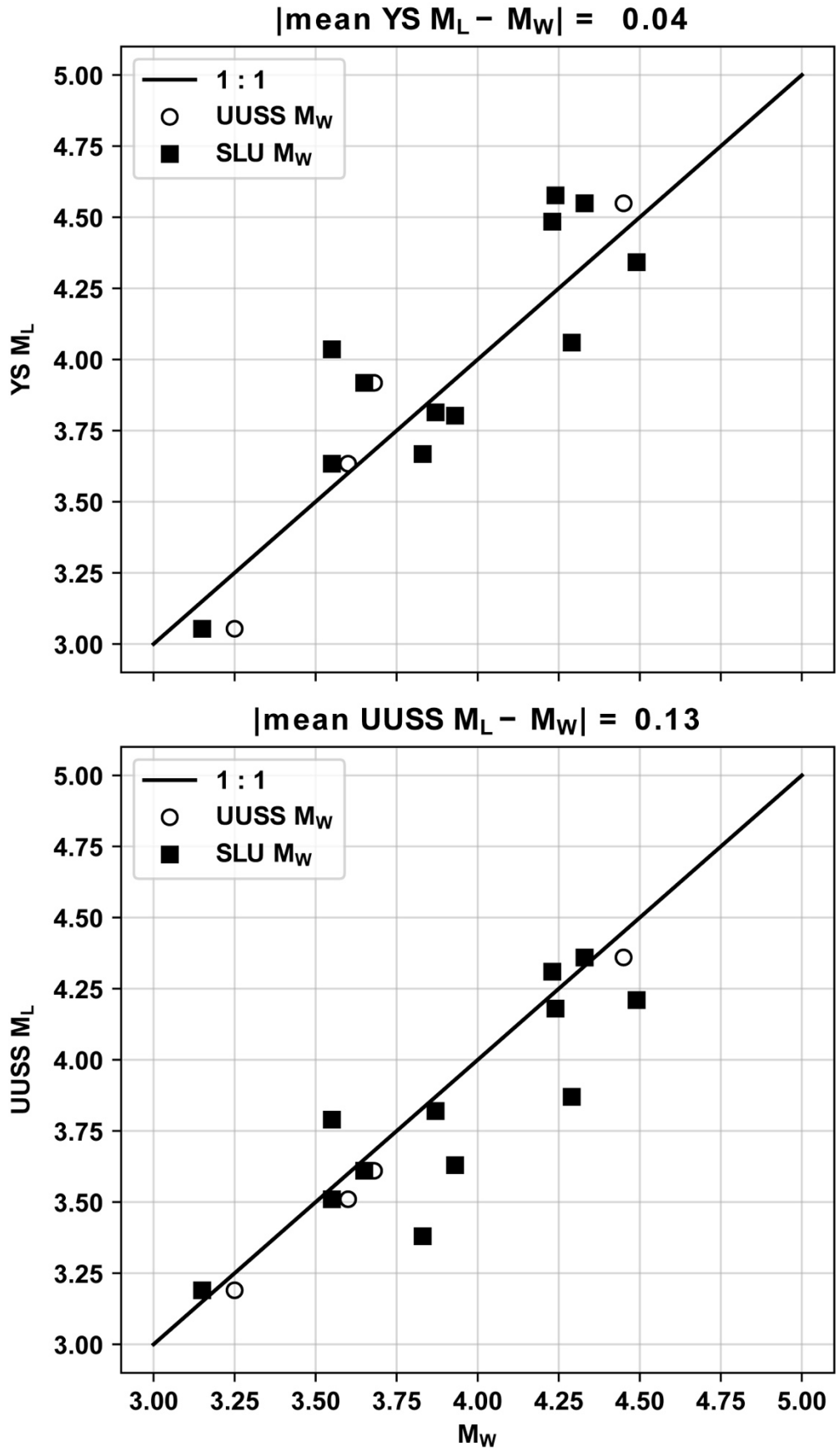

Figure 3.12 – Comparison of YS M_L and UUSS M_L with M_W.

vertical line in Figure 3.11), the maximum deviation is ~ 0.11 m.u. and ~ 0.09 m.u. on average. For UUSS $M_L \geq 3.6$ (solid thin vertical line in Figure 3.11) the maximum deviation is ~ 0.24 m.u. and ~ 0.18 m.u. on average. Qualitatively, the relationship between UUSS M_L and YS M_L appears to have some inherent non-linearity, but we refrain from modelling this since there is no obvious physical justification. Figure 3.12 shows the YS M_L and M_W (top) and UUSS M_L vs M_W (bottom) is also shown for comparison. YS M_L has a closer to 1:1 relationship with M_W than UUSS M_L. The mean difference between YS M_L and M_W is -0.04 m.u, which is within one standard error of M_W (0.05 m.u; Arabasz et al., 2016).

In Figure 3.13 we show station magnitude - event magnitude residuals (Sta M_L – Ev M_L) for UUSS M_L and YS M_L (Figures 3.13a, b and c, d) with and without the inclusion of station corrections (Figure 13a, c and b, d). For reference, the solid black line is the zero-centre line and the dashed lines are ± 0.05 about the centre line. The data was binned using R58 distances (R_{EPI}) as bin edges, such that each bin is centred between distance pairs from 0 – 180 km[14]. All subplots of Figure 3.13 have been cropped to a window of -0.75 < Sta M_L – Ev M_L < 0.75, however Figure 3.13a, b have residuals ranging from -1 to 2 and -1 to 1 respectively, from near-field data (R_{EPI} < 25 km). For the UUSS Sta M_L – Ev M_L, the inclusion of station corrections reduced the root-mean square error (RMSE) from 0.21 to 0.15 and appears to reduce the negative bias that is observed without station corrections. However, the variability is greatly reduced for YS Sta M_L – Ev M_L, even without station corrections the RMSE is 0.09 and is reduced further to 0.04 by including station corrections. Also, we note that the binned Sta M_L – Ev M_L shown in Figure 3.13d all fall within 0.05 to with 95% confidence intervals. Figure 4B (Appendix B) shows two histograms of Sta M_L – Ev M_L, with station corrections included, for UUSS (Figure 3.13b) and YS (Figure 3.13d). The YS residuals show a tighter distribution than UUSS, the standard deviation was reduced by more than 0.1 m.u. from 0.29 to 0.18 by using the YS19 distance correction and station corrections to calculate M_L.

[14] Including an extra node at 75 km (see *Data and Processing*).

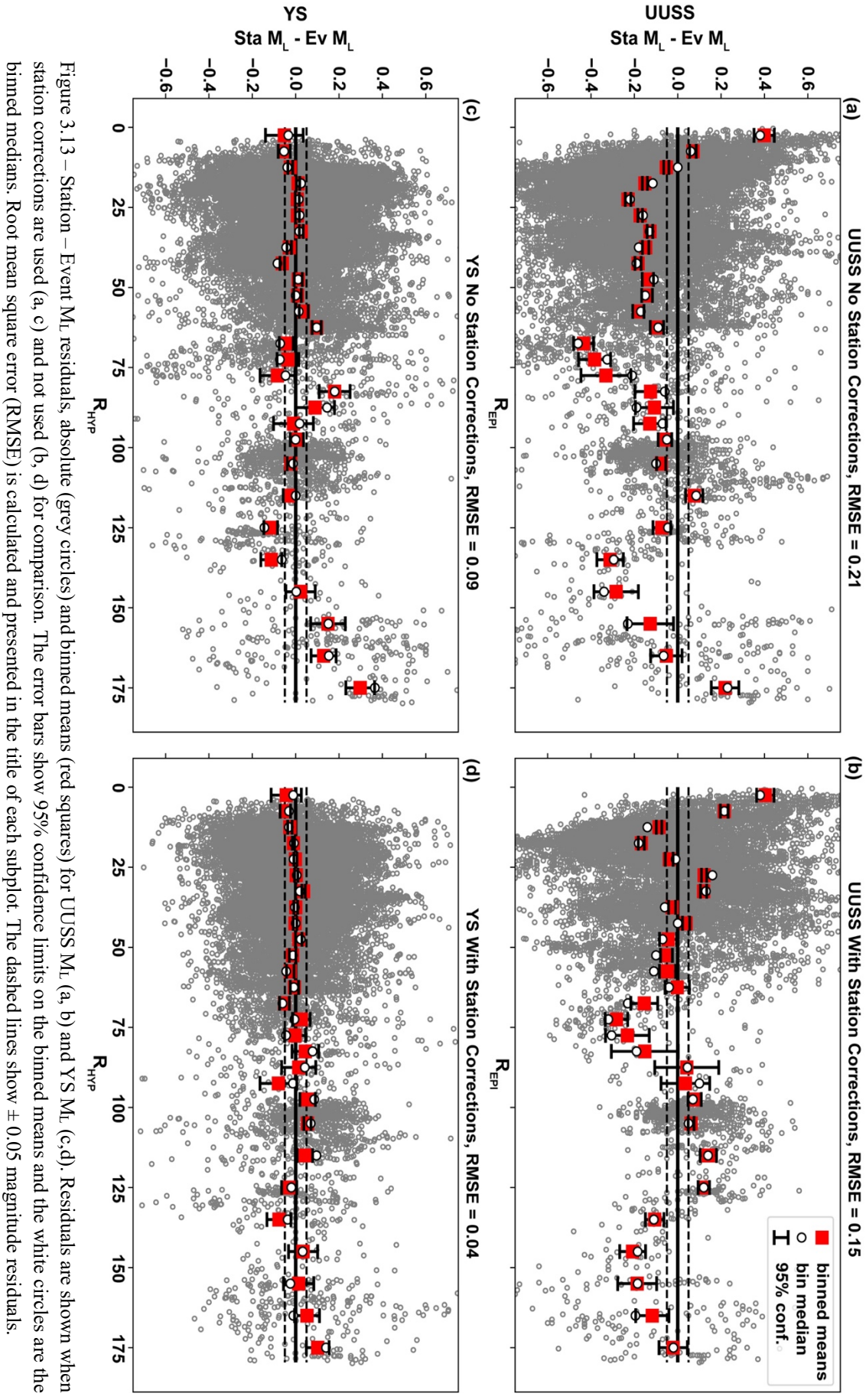

Figure 3.13 – Station – Event M_L residuals, absolute (grey circles) and binned means (red squares) for UUSS M_L (a, b) and YS M_L (c,d). Residuals are shown when station corrections are used (a, c) and not used (b, d) for comparison. The error bars show 95% confidence limits on the binned means and the white circles are the binned medians. Root mean square error (RMSE) is calculated and presented in the title of each subplot. The dashed lines show ± 0.05 magnitude residuals.

4.5 Discussion

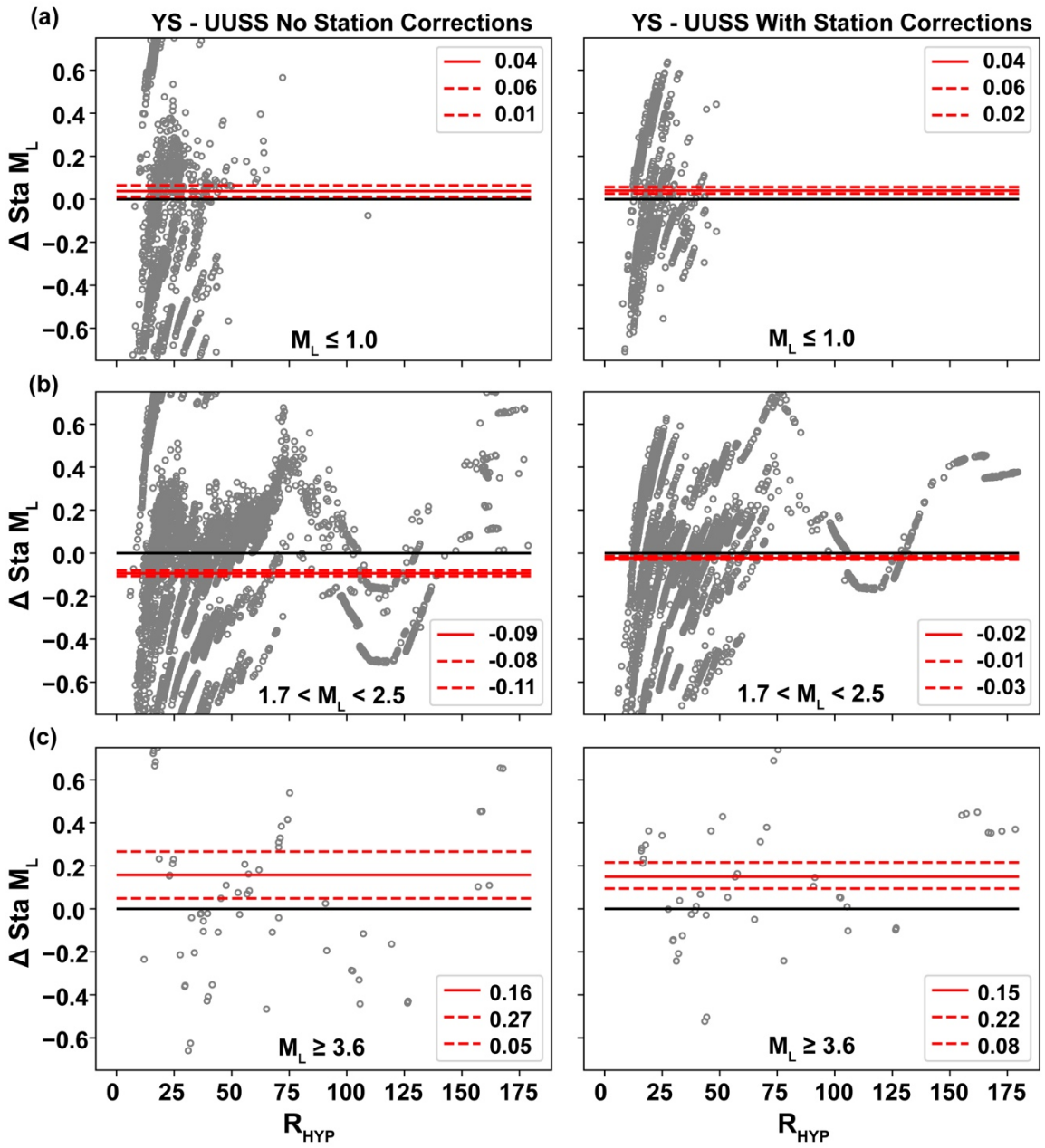

Figure 3.14 – YS station ML – UUSS station ML residuals, with (right column) and without (left column) station corrections, for three UUSS ML bands (a, b and c) identified in Figure 13.11. The mean residual is the solid line and ± 95 % confidence limits on the mean.

Although the distance correction used to calculate YS M_L (YS19) is quite different from that used to calculate UUSS M_L (R58), overall UUSS M_L matches YS M_L remarkably well (Figures 3.10 and 3.13). One could attribute this to the fact that R58 behaves like a smooth average of YS19 over the whole distance range (R_{HYP} < 180 km). Although, we can clearly see that below UUSS M_L ~ 1 and above UUSS M_L ~ 3.6, there is significant (to within 95% confidence) underestimation of YS M_L. For the latter range there are fewer data, but the fact M_W and YS M_L were in better agreement

in this range is a good indication that YS19 is likely correct and that this difference is real. However, from Figures 3.10 and Figure 3.11 it is hard to see exactly where the difference is being introduced.

To better understand the deviation from 1:1 we looked at the differences M_L recorded at each station (Δ Sta M_L) using the YS or UUSS distance correction, with and without station corrections (Figure 3.14). The data used in rows a, b and c was binned to match the three distinct 'zones' we have marked in Figure 3.11. The first zone uses data from earthquakes with UUSS $M_L < 1$, the second $1.7 <$ UUSS $M_L < 2.5$ (red dashed box in Figure 3.11) and the third UUSS $M_L > 3.6$. The bin sizes were chosen to each cover two magnitude bins presented in Figure 3.11 (mainly to include more data for the third zone). Observing the differences in station M_L, we pick out the broad effects of the distance correction on the difference in average YS M_L – UUSS M_L by taking the mean Δ Sta M_L (red line), we also plot 95% confidence limits on the mean (dashed red line).

Figure 3.14a shows that over the short distance range that small earthquakes are recorded at, the YS M_L tends to be slightly larger (~0.04 m.u) regardless of whether station corrections are used. It appears that such small events were more likely be recorded at distances that straddle the first R58 / YS19 crossover distance (Figure 3.8) and enough recorded at $R_{HYP} > 18$ km, where YS19 is larger, to cause the average UUSS M_L to be smaller than YS M_L. It is possible that if there were more stations with station corrections at $R_{HYP} < 25$ it could have balanced out. That balancing is the most likely reason why UUSS M_L in zone 2 matches YS M_L so well. These were recorded over a sufficient distance, such that UUSS M_L would average to be approximately the same as YS M_L. We observe the same pattern in Figure 3.14b as we do for YS19 – R58 in Figure 3.11. In fact, there is a slight negative bias (when using station corrections) in Figure 3.14b that is also present in Figure 3.11 over the same range of M_L. The difference is far more significant without the use of station corrections, where UUSS M_L is larger over the whole distance range (which is also the only range where they make a significant difference to the mean). Finally, in Figure 3.14c we again see the same pattern that is observed in Figure 3.11 (UUSS $M_L > 3.6$) that YS is overall larger than UUSS. For such large earthquakes it appears as though they depend largely on

records from stations further than 18 km, where YS19 attenuation is more different than R58 (except for the narrow band between 100-125 km; Figure 3.8).

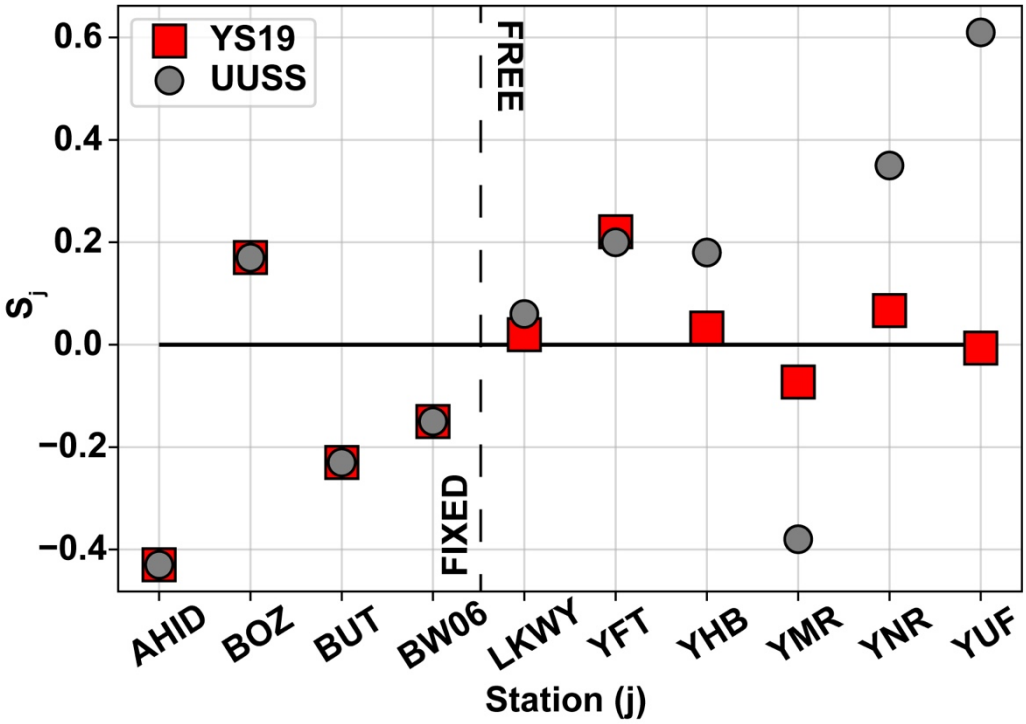

Figure 3.15 – Comparison of UUSS station corrections (grey circles) with station corrections derived via inversion (red squares). Station corrections that are fixed plot on the left side of vertical the dashed line.

We can conclude that the differences at small and large M_L are likely due to some combination of the difference in the distance correction and the specific nuances of the datasets used to calculate each earthquake For the mid-range however, it appears that there are two major factors: (1) that these earthquakes tend to be recorded over enough distances that the overall difference between YS19 and R58 cancel out and (2) station corrections have made up for the difference in actual attenuation compared to R58. With regard to (1), if not for the fact that apparent attenuation in YS starts reducing at $75 < R_{HYP} < 125$, UUSS M_L would have been far greater than YS M_L at nearly all distances (> 18 km). In general, apparent reduction in attenuation is not unique to Yellowstone and has been observed before using similar methods (e.g. Wesley Greig et al., 2018; Bindi et al., 2019). However, what is unique is that the apparent reduction in attenuation is very sharp in a very narrow range.

Many studies attribute post-critical moho reflections to such phenomena (e.g. Atkinson and Merau, 1992). The post-critical reflections could also come from a shallower layer

with sharp positive or negative (e.g. low-velocity layer) shear-wave velocity gradient (Catchings and Kohler, 1996). However, post-critical moho reflections seem more likely for Yellowstone given the depth of the moho (~45 km, Huang et al., 2015) and the distance range of the apparent reduction in attenuation. Finally, the rationale for (2) comes from looking at Figure 3.15b and at the difference between the YS19 station corrections and the existing UUSS corrections from Pechmann et al. (2007) (Figure 3.15). Overall, for corrections that were not fixed (red squares in Figure 3.9 and 3.15), three UUSS corrections are significantly more positive than YS19 station corrections (YHB, YNR and YNF), two are close (LKWY and YFT) and one is much more negative (YMR). An explanation for this is that the minimisation gave some stations that were > 0, very large corrections in a bid to increase M_L to make up for the M_L deficit observed in Figure 3.13a. Additionally, because they were constrained to sum to 0, the corrections < 0 were too negative to make up for those larger corrections. We suspect that the YS19 corrections are more reliable in the Yellowstone catalogue region since they trade-off less with the complex local attenuation.

3.6 Conclusions and Future Work

Using a high-quality catalogue of local earthquakes recorded in (and in close proximity) to the Yellowstone National Park region, we have successfully recalibrated the M_L scale. We gauge our success on the basis that YS M_L has a better agreement with M_W than the previous estimates and the significant reduction of magnitude-distance residuals. In tandem, we were able to produce new station corrections for an additional 10 stations and improved 6 of them. Using the new M_L scale (and station corrections) we recomputed M_L (YS M_L) for earthquakes and compared it to the old M_L (UUSS M_L). While the difference was unimportant for small M_L, for larger M_L it is more problematic. UUSS M_L large enough to be considered in seismic hazard assessment are currently underestimated in Yellowstone. Fortunately, this difference is only on the order of ~ 0.2 m.u. at maximum, which is approximately one standard deviation from mean UUSS M_L (Arabsaz et al., 2016). Additionally, this is in the range where it would be possible to calculate moment tensor solutions for such events, which are preferable for the hazard assessment. Nevertheless, we recommend that earthquakes with UUSS M_L > 3.4 (3.6 – 1 standard deviation) should be recomputed with YS19.

For the most part, UUSS M_L was close to YS M_L with the exception of small (< 1) or large (> 3.6) M_L. We surmised that there were likely two main reasons why UUSS M_L was similar to YS M_L (1) old station corrections made up for some of the difference in attenuation and (2) a sharp apparent reduction of attenuation in Yellowstone between 75 and 125 km meant that R58 was a smooth average of the observed regional attenuation. The issue highlighted in (1) is of great importance as it shows how highly dependent station corrections can be on assumptions used for their derivation with regard to M_L. We note that there generally seems to be little effort toward validating station corrections against site information (e.g. Vs30, surface-to-borehole ratios, 1D modelling). It is unfortunate that for the Yellowstone network we do not have site information to compare our station corrections with. We aim to implement methods of deriving station corrections that are independent of the distance correction and magnitude and are related to physical site properties in further studies. Ultimately, we discovered that attenuation in Yellowstone is clearly complex and we want to investigate the origin of this feature, but it is beyond the scope of this study.

Chapter 4: Scenario-Dependent Site Effects for the Determination of Unbiased Local Magnitude

Chapter 4 is derived from a manuscript accepted by the *Bulletin of the Seismological Society of America* on 03/09/2019, *in press,* doi: TBD. The authors of this manuscript are James Holt (main author), Benjamin Edwards and Valerio Poggi. The study was aimed at the reduction of uncertainty in station corrections (and by extension local magnitude) used by local magnitude scales via a single station modelling approach. We prototyped a new method of deriving station correction using surface/borehole data and compared the result with real measurements. We show that station corrections derived in this way closely followed the difference in Wood-Anderson amplitude and have a strong magnitude-distance (scenario) dependence. We then propose how these corrections may be used in the future to reduce epistemic uncertainty in station corrections used in local magnitude prediction. Finally, we use our models to understand the driving force behind the scenario dependence and reinforce our current understanding of the **M** - M_L relationship. Benjamin Edwards assisted with the analysis and helped draft the manuscript. Valerio Poggi provided code to calculate the theoretical site amplification functions and helped draft the manuscript.

Abstract

We explore the role of scenario-dependent site amplification on local magnitude (M_L) and possible bias it may introduce. M_L is strongly influenced by local site response, which is conditioned by unique local geological factors. In order to isolate the effect of the near-surface amplification on M_L, relative differences between station-specific M_L at the surface and borehole ($\Delta M_{L,STN}$) are studied for 34 sites from the KiK-Net network, Japan. We find strong moment magnitude (**M**) dependent, scenario specific, $\Delta M_{L,STN}$ trends over the range $3.0 < \mathbf{M} < 6.5$. To model these trends, we employ the stochastic method, initially using empirical surface/borehole Fourier spectral ratios (S/B) for the site term. Simulated data, $\Delta M_{L,STN}(\mathbf{M})$, based on the available site response information are shown to closely match the empirical $\Delta M_{L,STN}$ trends. Subsequently, the site term is replaced with (i) linear 1D-SHTF amplification, (ii) H/V ratios, and (iii) QWL amplification to calculate $\Delta M_{L,STN}(\mathbf{M})$ in the absence of S/B. We find that $\Delta M_{L,STN}(\mathbf{M})$ trends are best estimated with S/B as the site term, but in many

cases using a linear 1D-SHTF model is adequate. Furthermore, we discuss how this phenomenon may be related to the observed inequality between **M** and M_L at low magnitudes and how $\Delta M_{L,STN}(\mathbf{M})$ may be used in the future to compute unbiased M_L with greater confidence.

4.1 Introduction

Earthquake magnitude quantifies a measurable characteristic of a particular event, such as the size of a fault rupture or the resultant ground motion field. There are several magnitude scales used in different parts of the world, each with their own distinct advantages and disadvantages. We limit our investigation to local magnitude, M_L (Richter, 1935) and moment magnitude, **M** (Kanamori, 1977; Hanks and Kanamori, 1979). We use **M** to represent moment magnitude as it is distinct from M_w in its applicability across a broad range of moment magnitudes. M_W, was originally based on work done is more generally used where seismic moment (M_0) is derived from moment tensor solutions. The moment magnitude we use here, **M**, was derived by combining the equations for surface-wave magnitude (M_S), M_L and M_W (Hanks and Kanamori, 1979). The almost ubiquitous use of M_L at seismological observatories worldwide is due to the simplicity of derivation and the fact that, over the range of interest to seismic hazard ($\mathbf{M}/M_L > 4$ or $M_L > 2.5$ for induced seismicity close to urbanised areas, Bommer et al., 2017), the magnitude-frequency distribution (MFD) appears to follow a power law (Gutenberg and Richter, 1954; G-R). This grants the ability to predict the frequency of earthquakes with given magnitude, a feature crucial for probabilistic seismic hazard analysis (PSHA) (Reiter, 1991). The *a* and *b* values (describing the seismicity rate and relative proportion of small to large events, respectively) in the G-R relation for a particular region or source zone have significant influence on generated hazard curves (Beauval and Scotti, 2004). It is therefore important that earthquake catalogues used to develop G-R relations are unbiased, in order to achieve an accurate representation of seismic hazard. Local magnitudes are also used to inform regulatory decision making. For instance, traffic light systems depend on reliable and unbiased values of M_L to inform the statistics behind critical decision-making models for safe unconventional oil/gas (hydraulic fracturing, or fracking) and geothermal energy extraction (e.g. Bommer et al., 2006; Mignan et al., 2017).

Generally, in earthquake hazard and risk applications, the use of **M** is preferred over M_L as **M** is related to the physical properties of the rupture. However, this metric is challenging to derive confidently and routinely for **M** < 3.5 with conventional methodology. One may question the need for accurate assessment of earthquake magnitude less than $\mathbf{M}_{min} \sim 4$, the lowermost magnitude typically considered in PSHA after consideration of risk potential (Bommer and Crowley, 2017). The reason is that in regions of low or moderate seismicity (or for small source zones, e.g. induced seismicity), the bulk of available data is below $\mathbf{M}_{min}$: the frequency of relevant events ($\mathbf{M} > \mathbf{M}_{min}$) is predicted through extrapolation of the G-R relation (or any alternative magnitude-frequency relations) derived at lower magnitudes, most commonly using M_L. M_L is considered regionally specific, so if a hazard analysis must be performed over multiple regions, catalogues are usually converted to **M** before harmonisation. This is problematic as there is a known inequality between **M** and M_L (Dost et al., 2018; Hanks and Boore, 1984). As a result, to facilitate the MFD (of **M)** from catalogues containing mostly small M_L, the derivation of scaling relationships between the two quantities has become common.

Deichmann (2006) showed that theoretically, in the absence of the Wood-Anderson instrument response and attenuation (or appropriately corrected attenuation), there should exist a 1:1 relation between M_L and **M**. However, in practice it is found that M_L, on average, systematically underestimates **M** for small **M** (< 2) and overestimates for larger **M** (> 3). This is problematic, particularly as **M** estimates are scarce for comparison with M_L in this range. In particular: (1) it is difficult to determine confident **M** values for $M_L < 3$; (2) there is reduced reliability of resultant empirical M_L to **M** correction (due to their inequality); and (3) incorrect magnitude conversion can lead to over or underestimated recurrence rates within specific magnitude ranges.

Many authors have attempted to develop scaling laws to map the **M**:M_L relationship (e.g. Hanks and Boore, 1984; Grünthal et al., 2009; Edwards et al., 2010). At regional levels these scaling relationships are typically linear adjustments in the form $M_L = b\mathbf{M} - c$, where b, c are constants over a limited magnitude range (e.g. Munafó et al., 2016). Studies investigating wider magnitude ranges observed quadratic scaling (e.g. Dost et al., 2018), while theoretical considerations suggest a transition in linear scaling, with $\mathbf{M} \propto 2/3\ M_L$ for **M** < ~2 and $\mathbf{M} \propto M_L$ for **M** > ~4. It is clear that the form of this

relation holds broader implications for extrapolation beyond the data threshold. Deichmann (2017) offers an explanation entailing that the combined effects of path and site attenuation (dominated by site attenuation) and resultant minimum observed pulse duration are at least partly responsible for driving the divergence of **M** and M_L at low magnitudes.

4.1.1 Local Magnitude, Station Corrections and Site Response

The local magnitude (M_L) scale (Richter, 1935) is given by:

$$M_L = \log_{10}(A_{WA}) - \log_{10}(A_0), \quad (4.1)$$

where A_{WA} is the displacement amplitude (in mm) as measured on a Wood-Anderson (WA) torsion seismometer and $-\log_{10}(A_0)$ is a correction term (a function of distance, and due to geometrical spreading and local intrinsic/scattering attenuation effects). Today, the WA response is simulated by convolving the response with broadband records (after the original instrument response is removed) (Kanamori and Jennings, 1978).

Distance dependent corrections alone are not sufficient to completely remove bias, there also must be consideration of local site effects. There is usually an effort to install stations on hard rock sites to minimise site effects. However, it is not always possible to install stations on hard rock and installing stations on hard rock is becoming less common as networks: (1) densify in urban areas and (2) monitor induced seismicity where we are rarely able to install on hard rock. It is generally well understood that stations located on soft rock/soil amplify ground motion compared to stations installed on hard rock sites. The extent of this amplification depends on the specific geological properties of the site, such as soil/rock density, seismic velocity, attenuation properties (degree of damping/heterogeneity), topographic effects, and basin focussing effects (Régnier et al., 2018). The original definition of local magnitude (Equation 4.1) does not consider local site effects, only attenuation along the path (geometrical spreading, and to some extent, path specific high frequency attenuation, Q). As a result of local amplification effects, the variation in site-to-site magnitude prediction can be as high as 1-2 magnitude units in extreme cases (Miao and Langston, 2007). Naturally, this

level of uncertainty is unacceptable, so an attempt is made to reduce the scatter by adding a site term to Equation 4.1:

$$M_L = \log_{10}(A) - \log_{10}(A_0) + S_i. \quad (4.2)$$

Equation 4.2 (Hanks and Boore, 1987; Pechmann et al., 2007) is the definition of local magnitude including station corrections S_i, where subscript i, is a unique station.

S_i are commonly derived via minimisation along with the attenuation correction (Castello et al., 2007; Miao and Langston, 2007; Illsley-Kemp et al., 2017). The minimisation attempts to reduce the difference between single station magnitude predictions ($M_{L,STN}$), by offering static magnitude corrections for each site, which are typically constrained such that all S_i sum to zero. So, for a group of stations, corrections may be positive or negative. However, since there is no universal practice, they may be derived via other methods: relative to trusted M_L (Edwards et al., 2015), relative to **M** (Ristau et al., 2016) or relative to a trusted site with a known station correction (Pechmann et al., 2007), for example. While some networks consider uncertainty in static station corrections (e.g. Bindi et al., 2019), in practice the uncertainty is rarely, if at all, used in magnitude calculations. Static station corrections tend to average over the range of magnitude-distance combinations observed in the data. On average and with good site conditions (e.g. hard rock), this may be adequate. However, it may be insufficient for more 'rare' earthquakes and/or sub-optimal site conditions outside of a standard network coverage due to scenario-specific variability.

This study mainly is focussed on the impact, and derivation, of scenario-specific M_L amplification, as first observed in linear amplification factors for pseudo response spectra (Stafford et al., 2017). In the following, we probe potential biases and uncertainty in the direct determination of local magnitude (for arbitrary earthquake scenarios) and how this may be fundamentally tied to local site effects. Using the stochastic method and a number of common empirical/deterministic site response models; we explore the complex interaction between the source, path, and site, which lead to earthquake-scenario-specific station correction sensitivity. Synthetic Wood-Anderson (WA) seismograms (generated using the stochastic method) are used to model the difference in observed WA peak displacements between surface and

borehole sensors ($\Delta M_{L,STN}$), measured at 34 sites in the KiK-Net network, Japan. The bulk site response phenomena (amplification/diminution) is assumed to occur between the borehole (at depths of approx. 100 to 200 m) and surface and it is this response that traditional static station corrections attempt to account for. We show that static station corrections developed via a standard network approach cannot fully capture the scenario-specific (magnitude – distance) variability in ΔM_L that we observe and model (over the range $1 < \mathbf{M} < 7$) using our single station approach. Aside this, we use the result of this study as a theoretical basis to comment on our understanding of the **M**-M_L scaling relationship. Finally, we provide some recommendations on how the method may be reproduced and then used in practice.

4.2 Simulation of Wood-Anderson Seismograms (and M_L) using the Stochastic Method

As summarised in Boore (2003), the stochastic method was first developed by Hanks (1979) as a tool to model the frequency content of the seismic wave-field. The method was then modified by Boore (1983) to produce time-domain records. It combines pseudo-physical frequency domain-based models, that define the earthquake source, $S(\omega)$, path-effects, $G(R, Q)$, and local site response, $R(\omega, \kappa_0)$, with random phase information to generate synthetic seismograms. In essence, the model attempts to simulate the interaction between the earthquake source, the propagation medium and the subsequent interaction with an arbitrary oscillator at the surface (in our case, the Wood-Anderson seismometer) (Hanks and Boore, 1984). Stochastic models are well suited to test the sensitivity of ground motion to various models/model parameters (e.g. stress parameter $\Delta\sigma$, high-frequency spectral decay κ_0, and the quality factor Q). This enables a cursory view at which parameters may drive uncertainty in M_L and by extension, the **M**-M_L relationship.

We present a stochastic model definition representative of a synthetic Wood-Anderson record, $A_{WA}(t)$, modified from Boore (2003) as:

$$A_{WA}(t) = \mathcal{F}^{-1}[\mathcal{F}[N(t)]E(M_0, f)P(R, f)T(f)I_{WA}(f)] \quad (4.3)$$

Here, $\mathcal{F}[N(t)]$ is the Fourier transform of random white noise with duration t (the sum of source and path duration), normalised to RMS = 1 and $\mathcal{F}^{-1}$ is the inverse Fourier transform. $E(M_0, f)$ is the source model, where any reasonable source definition may be implemented. For our specific case $E(M_0, f)$ is the (Brune, 1970, 1971) ω^2 spectrum in acceleration:

$$|E(f)| = \left[CM_0 \frac{\omega^2}{1 + \left(\frac{f}{f_c}\right)^2} \right] \qquad (4.4)$$

$$C = \frac{\langle R_{\Theta\phi} \rangle F \xi}{4\pi\rho v_s^3}$$

with M_0, the seismic moment (N·m), f the frequency (Hz), ω the angular frequency (rad.s^{-1}), f_c the corner frequency of the spectrum (Hz). $\langle R_{\Theta\phi} \rangle$ is the average radiation coefficient, ξ is the partitioning of energy at the source, and F is the free surface effect, (Brune, 1970, 1971). Constant, C, is scaled by the average density (ρ = 2800 kg/m^3) and the average shear wave velocity (v_s = 3500 m/s) at the source. This is a point source definition, single slope / corner frequency, controlled by the stress drop ($\Delta\sigma$) [~ 1 MPa for crustal earthquakes in Japan (Oth et al., 2010)]. With regard to this application, the definition is adequate for approximation of the seismic source radiation, relevant over most earthquake distances and magnitudes studied. We note that at large magnitudes (**M** > ~ 6) and short distances this model may be unsuitable as finite fault effects (e.g. directionality, non-uniform seismic radiation and saturation [Yenier and Atkinson, 2014]) become significant. However, since this study considers the analysis of spectral ratios, the aforementioned limitation is minimised.

$P(R, f)$ in Equation 4.3 represents a combined attenuation model accounting for the effects of geometrical spreading, $G(R)$, where R is epicentral distance in km (referred to as R_{epi} henceforth), and high frequency anelastic attenuation, exp $(-\pi f R/Q\beta)$, along the path due to scattering and absorption; Q is quality factor (Knopoff, 1964b) and β is the average crustal shear wave velocity (3500 m/s). Geometrical spreading is assumed to be $1/R$ in all models. $I_{WA}(f)$ is the response of the Wood-Anderson torsion seismometer, which behaves like a high pass filter, with a corner frequency at 1.25 Hz (f_{WA}).

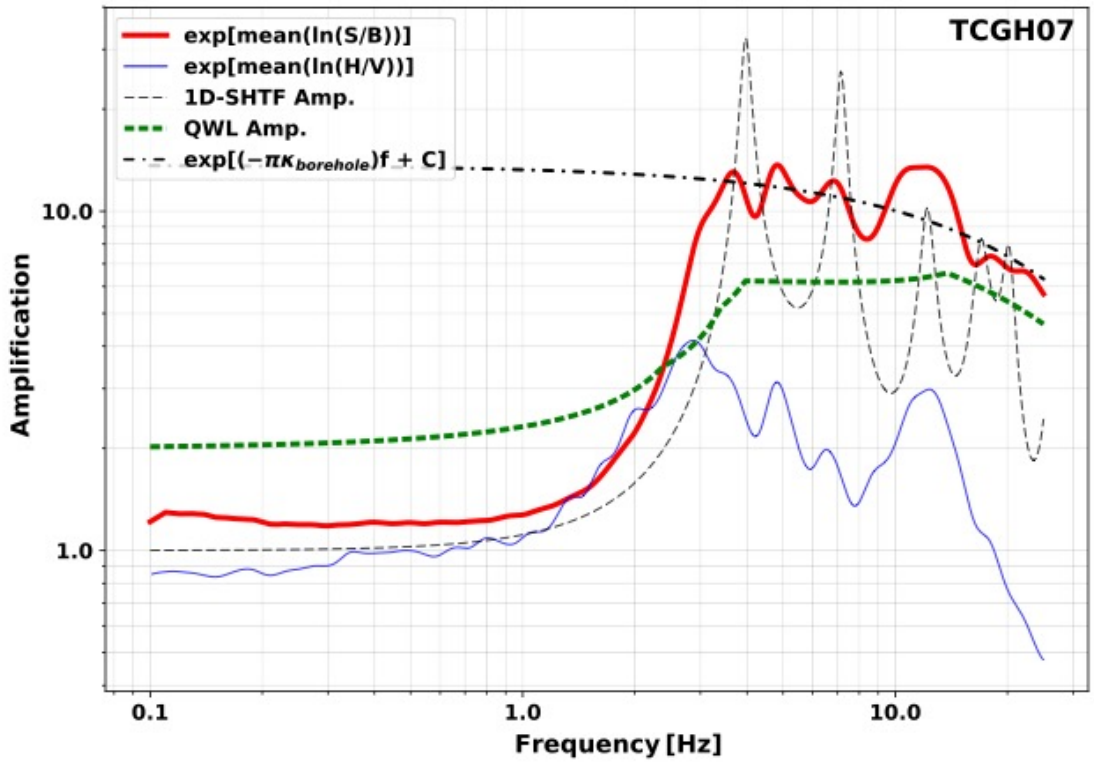

Figure 4.1 – Four site response representations calculated for the site TCGH07 of the KiK-Net Network, Japan. Natural log (ln) mean S/B ratio (BFSR) is represented by the solid red line. The solid blue curve is the ln mean H/V ratio. The uncertainties (± 1 standard deviation) for all amplification functions are shown in Figure C3, Appendix C, of the supplementary material. The dashed green line is the QWL amplification curve computed for the site, using the standard KiK-Net V_S soil profiles. The dashed black line is the 1D-SHTF, computed using the 'outcrop-within' assumption. Both theoretical models include attenuation derived from the BFSR. The light blue curve is the modelled attenuation (Anderson and Hough, 1984), see method section for more details. The 1D-SHTF and the QWL were calculated using the open source OpenQuake Site Response Toolkit (OQ-SRTK). Note that the QWL representation is explicitly outcrop-outcrop and therefore includes a generic free-surface effect (factor of 2, Boore, 2013) to make it comparable at high frequency with the within-outcrop (borehole-surface) interpretation.

Finally, $T(f)$ is the site response model, including the effects of resonance induced amplification and associated high frequency filtering (κ_0, Anderson and Hough, 1984). We represent site amplification using four different models, split evenly between empirical and theoretical (Figure 4.1). For the empirical models we use the surface-to-borehole ratio (S/B) [sometimes referred to as the borehole Fourier spectral ratio (Régnier et al., 2018)] and H/V ratio (Nakamura, 1989). Theoretical models used in

the study include the 1D shear wave (horizontal) transfer function (1D-SHTF) (Kramer, 1996) and square root impedance amplification (Boore, 2013), also known as the quarter wavelength (QWL) amplification.

4.2.1 Site Response Models

Since it is uncommon to have borehole data, we explore the use of methods that do not require this information. To that end, we developed four stochastic models, each utilising a different site response model, with only the first requiring borehole data. This provides an opportunity to discuss the sensitivity of M_L to the site response, but also to probe which representation(s) of the site response is necessary to replicate observed site-effects on M_L.

S/B is the ratio of the Fourier amplitude spectra of acceleration (FAS) from surface and borehole recordings (Figure 4.1). The S/B model contains 'within' motion information, it considers constructive and destructive interference between the surface and borehole sensors. The S/B model depends on the velocity/damping structure of the soil column to dictate which wavelengths will constructively or destructively interfere. The H/V ratio is calculated using FAS from the horizontal and vertical channels, averaged over many seismic events at a single site (Figure 4.1). Other studies have shown strong links between the H/V and S/B (Sardinal and Midorikawa, 2004). This is likely because both ratios are sensitive to the resonance of horizontally polarised S waves (Rodriguez and Midorikawa, 2003).

It is possible to calculate theoretical models of the S/B ratio by utilising 1D material property models of the site, assuming an anelastic half space below the borehole layer. By considering the propagation of vertically incident shear waves (horizontal polarisation, travelling upward and downward) at distinct frequencies we can calculate the total amplitude in any given layer (Knopoff, 1964a). This study utilises open source software, OpenQuake SiteResponseToolkit, to produce all theoretical site models. OpenQuake SiteResponseToolkit is an open source python library of methods for site response analysis developed by the Global Earthquake Model Foundation, it is still currently under development.

QWL amplification is a typical choice when performing stochastic simulations (Boore, 2003, 2013), particularly for computing amplification at generic rock sites (Boore and Joyner, 1997). For details on formulation we refer the reader to Poggi et al. (2012) and Boore (2013). The QWL amplification provides a smooth average through an outcrop-outcrop 1D-SHTF (analogous to a ramp function) that increases to maximum amplification at around the site fundamental frequency (f_0) and then remains constant in a simple single layer over half-space system. In general, the QWL amplification will systematically underestimate peak amplification due to its smooth nature. f_0 can be estimated using the quarter wavelength approximation, $f_0 = \frac{V_s}{4H}$. For use in stochastic simulations, Boore (2013) noted that there should usually be a factor of 2 applied (as in Figure 4.1), to account for amplification related to the free surface effect in cases of within-outcrop amplification. This adjustment is applied here only to make the QWL comparable to within-outcrop motion at higher frequencies (f > 1 Hz).

4.2.2 Anelastic Attenuation

We obtain values of κ_0 (Anderson and Hough, 1984) for a subset of sites in the KiK-Net network from Poggi et al. (2013). They calculate κ_0 using data that extends over two distance ranges (< 50 km and < 300 km), resulting in two values for each site. We only select sites with absolute differences in κ_0 of less than 1% to ensure robustness. We refer the reader to the Poggi et al. (2013) for an in-depth review of the methodology.

Attenuation between the surface and borehole (κ_b) must be separated from κ_0, since κ_0 includes attenuation beyond the borehole/reference rock horizon. We therefore split κ_0 into two parts:

$$\kappa_0 = \kappa_b + \kappa_{rock} \tag{4.5}$$

The value of κ_b depends on the characteristic diminution of the S/B measured at a particular site. The remaining portion (κ_{rock}), will be the contribution where amplification is not calculated (and is likely insignificant) below the borehole sensor. To calculate κ_b we fit a linear decay model to the S/B in log-linear space and extract the high frequency decay term, following the method outlined by Anderson and Hough (1984). κ_b is then mapped to Q_s by extension of a method detailed in Boore (2013):

$$Q_{S_i} = \frac{\left(\frac{H_i}{V_{S_i}}\right)}{\kappa_b / N} \tag{4.6}$$

In Equation 4.6, subscript i indicates site layer number, H is the layer thickness and N is the total number of layers. Note that κ_b itself is a component of site-specific attenuation κ_0 (such that $\kappa_b < \kappa_0$), Equation 4.5. κ_b can be further split linearly into smaller contributions for each layer. Without knowing the exact amount each layer contributes to the total decay we may distribute κ_b evenly across each soil layer. Overall, certain layers may over/underestimate true Q_S, however, the total contribution to attenuation is consistent with the observed S/B ratio by design. The purpose of mapping κ_b to Q_S is to validate our choice of κ_b, by using it as the input attenuation model to calculate the 1D-SHTF. We only choose κ_b when the visual match between the S/B and 1D-SHTF (Figure 1) is optimal. κ_b is usually found after 2-3 iterations of adjusting the fit to the observed decay of the S/B. All of the κ_0 and κ_b values used in this study are compiled in Table C1 (Appendix C).

4.3.3 Stochastic Models for Synthetic Surface and Borehole Records

Five stochastic model definitions are presented here: four with site functions included for the synthetic surface model (Equation 4.7) by replacing $T_b(f)$ with S/B, 1D-SHTF, H/V and QWL; and a reference synthetic borehole model (Equation 4.8).

$$A_{WA_S}(t)_j = \mathcal{F}^{-1}\left[\mathcal{F}\left[N(t)_j\right]E(M_0, f)P(R, f)T_r(f)T_b(f)I_{WA}(f)\right] \tag{4.7}$$

$$A_{WA_B}(t)_j = \mathcal{F}^{-1}[\mathcal{F}[N(t)_j]E(M_0, f)P(R, f)T_r(f)I_{WA}(f)] \tag{4.8}$$

Subscript S and B indicate surface and borehole, respectively. $T(f)$ in Equation 4.3 is modified to separate the site-effects below the borehole, $T_r(f)$, and the amplification/attenuation between the borehole and surface, $T_b(f)$. The site effects up to the borehole are given by $T_r(f) = \exp(-\pi f \kappa_{rock})$ and up to the surface with $T_r(f)T_b(f)$. Subscript j indicates the simulation number: we generate 100 synthetic waveforms with random phase using the surface and borehole definitions. It is necessary to take an average of the peak WA from many simulations because any

individual waveform will deviate from the average (Boore, 2003). The sample mean of peak the Wood-Anderson displacement (at either surface or borehole) is:

$$A_{WA} = \frac{1}{N}\sum_{j}^{J=100} \max\left(A_{WA}(t)_j\right) \tag{4.9}$$

4.3 Sensitivity Testing: Surface and Borehole Simulations for Peak WA Amplitudes

Table 4.1 – Arbitrary site model used for sensitivity testing. This site model is used to generate a collection of QWL amplification curves (variable fundamental frequencies; f_0 = 1-10 Hz).

Layer no.	Thickness (m)	$\boldsymbol{V_s}$ (m/s)
1	25	variable
2	∞	2600

To understand the influence of site-effects on M_L we calculate the difference in peak Wood-Anderson displacement between the surface and borehole:

$$\Delta M_L = \log_{10}\left({A_{WA_S}}/{A_{WA_B}}\right) \tag{4.10}$$

A_{WA_S} / A_{WA_B} are the peak Wood-Anderson amplitudes of the measurements and/or the average of synthetic surface/borehole records respectively. For the surface and borehole, the network attenuation correction ($-\log_{10}(A_0)$ in Equation 4.1) is identical and eliminated. Therefore, differences are driven by systematic site-effects, mapped into the peak Wood-Anderson amplitudes in the time domain. Sensitivity testing of the stochastic simulations was performed to ascertain parameters that are most influential to the change in M_L. We model an arbitrary site, as a single soil layer over half space, with simple structure (Table 4.1). Suites of tests are performed by modifying R_{epi}, Q, **M,** f_0, κ_0 and $\Delta\sigma$ and we highlight tests that showed the most significant changes (Figure 4.2). To modify f_0 we vary the top layer velocity and keep the layer thickness constant quarter wavelength approximation ($f_0 = \frac{V_S}{4H}$).

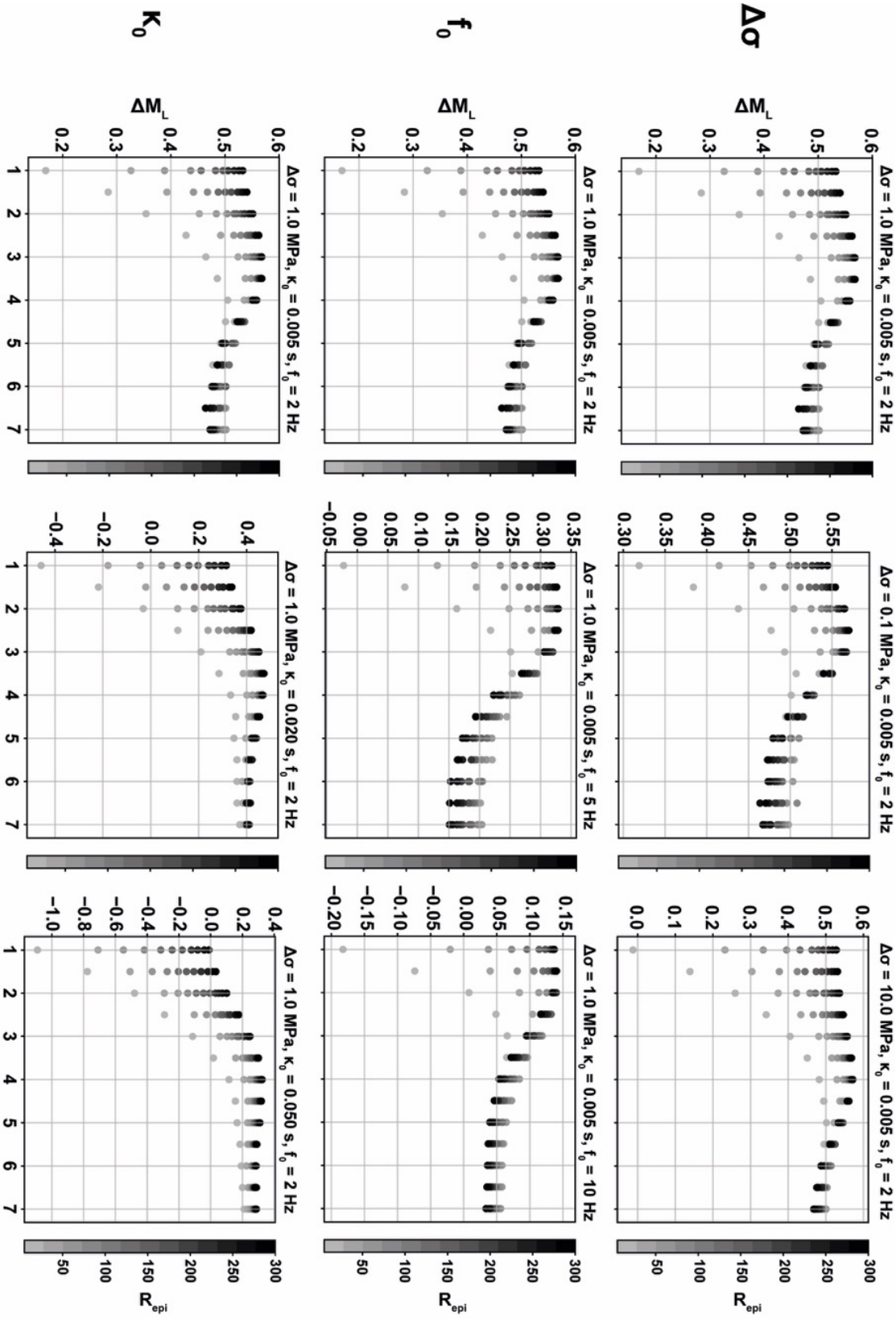

Figure 4.2 - A selection of sensitivity tests chosen to highlight key parameters. The first column shows the same set of curves, used as a base of comparison for discussion. The first row shows the sensitivity to stress drop, the second to changing fundamental frequency and the third to κ_0.

Figure 4.2 shows the difference in local magnitude between a theoretical surface and borehole site. In this stochastic model we use QWL amplification computed using the parameters listed in Table 4.1. Most notably, each model shows a strong dependence of ΔM_L on **M** and the form is consistent between simulations. When moving from large **M** (5 to 6) to small **M** (3 to 4), there is a smooth parabolic increase that reaches a peak at roughly **M** 3 to 4 at all distances. The rate of the decrease below **M** 3 to 4 is distance dependent, whereby close distances see a sharp relative decrease. The rate of fall-off reduces with increasing distance. At larger **M** (> 3), the WA instrument response becomes increasingly dominant as these events have lower source corner frequencies, and the WA transfer function damps long period energy. At this point the source/site interplay is diminished, so ΔM_L is dominated by the trade-off between site amplification and high frequency attenuation. It is important to note that at high **M** both the simulated borehole and surface spectra have the same corner frequency as the WA instrument response (f_{WA}) due to saturation. We make note of the fact that soil non-linearity has not been considered in any of the models. Non-linear response of soils to large magnitude earthquakes **M** (> 6) (e.g. Trifunac and Todorovska, 1996) would potentially break the ΔM_L saturation at large **M**, however the meaning of M_L becomes increasingly redundant as **M** continues to increase above this point due to saturation of the M_L scale.

From Figure 4.2 we observe $\Delta\sigma$, κ_0 and f_0 are all influential to ΔM_L, M_L's dependence on $\Delta\sigma$ and κ_0 is also noted in Deichmann (2006, 2017) and Edwards et al. (2010). The dependence on f_0 has not yet been discussed in direct relation to M_L but indirectly by Stafford et al. (2017), who investigated magnitude sensitivity on pseudo response spectra (to which M_L is related). $\Delta\sigma$ pushes the 'turning point' of the curve toward low **M** for low stress drop and higher **M** for high stress drop. Increasing f_0 to values consistent with rock (5 Hz) or hard rock sites (10 Hz) results in a shortening of the absolute range of $\Delta M_{L,STN}$(**M**) observed at any given site due to the overall reduced amplitude of the amplification function, which in turn lowers the difference between surface and borehole M_L. We still see > 0 convergence of ΔM_L at large **M** for hard rock f_0 (10 Hz). The convergence value of ΔM_L seems to depend on what the amplification of the QWL function is at frequencies close to f_{WA}. Concurrently, however small, the hard rock QWL has > 1 amplitude at frequencies close f_{WA} (see Figure C1, available

in the electronic supplement to this article), explaining the convergence to small ΔM_L (~ 0.05). The QWL amplification, with lower fundamental frequencies, has a greater impact on ΔM_L because it amplifies a broader range of frequency. This has the greatest significance if the peak or plateau of the combined WA - Brune spectrum frequency pass-band aligns with f_0. See Figure C2 (available in the electronic supplement to this article) for a comparison between median ΔM_L and increasing f_0 from 2 – 100 Hz. Implicitly, in all cases, the absolute site amplification (i.e. the amplification factor at any given frequency) is also related to the size of $\Delta M_{L,STN}(\mathbf{M})$. The larger these values are the greater the difference in $\Delta M_{L,STN}(\mathbf{M})$. Finally, the effect of κ_0 is greater for lower magnitude earthquakes, which have higher frequency content and, are more sensitive to damping. As a result, we see that at low **M** in certain scenarios (i.e. short propagation distances), ΔM_L can be negative.

From the sensitivity analysis it is clear that the effect of near-surface amplification on measured M_L is significant. For instance, small magnitude events ($M_L < 2$, as typical in induced seismicity) recorded at short distances (R < 50 km) tend to exhibit much lower amplification effects than typical tectonic seismicity (e.g. $M_L \sim 3$ recorded at 50 – 100 km) at the same site. However, the absolute level of amplification in both cases is strongly controlled by the site conditions (defined by f_0 , κ_0, and the absolute amplification provided).

4.4 Empirical Analysis: Data Selection and Processing

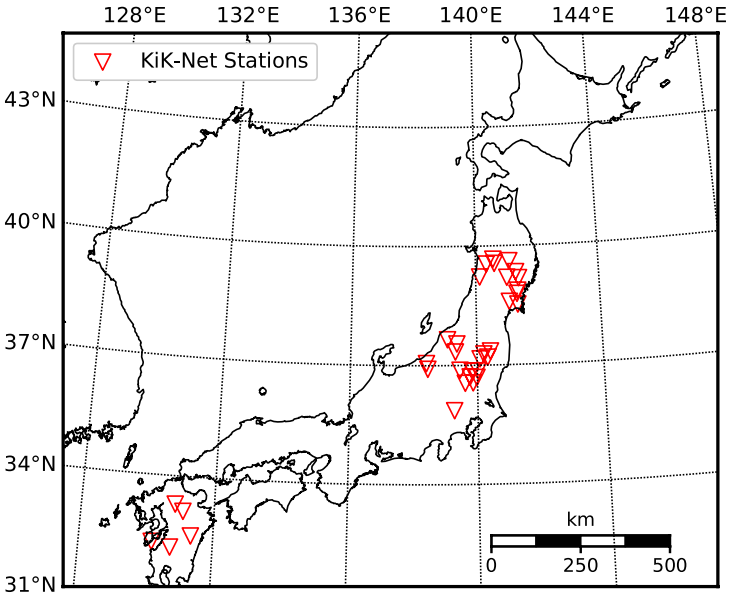

Figure 2.3 - Map of Japan showing the KiK-Net stations used in this study (red inverted triangles). In total the selection was narrowed to 34 stations. The subset was selected by availability and quality of κ_0 values provided by Poggi et al. (2013).

The Japan's KiK-Net network (operated by NEID) is composed of several hundred stations (distributed regularly across the country), each with surface and borehole instrumentation and a basic description of the material properties of the borehole. Generally, borehole depths are around 100 to 200 m depending on soil thickness, however some boreholes can extend to 1000 m in sedimentary basins (Aoi et al., 2004). This provides a unique opportunity to directly observe the effects of amplification and diminution for a range of sites with significant variation in local geology. Choice of target stations were limited by the availability of information about the characteristic high frequency attenuation (κ_0) of the sites; as this is necessary input to the stochastic simulations. Poggi et al. (2013) derived two sets of possible κ_0 values for a large number of KiK-Net stations. We chose a subset of 34 stations where κ_0 values were within 1% of each other (Figure 4.3). The subset stations are grouped into three clusters, the first (northernmost) located in Tohoko, the second (central) nested between Chubu, Kanto and Tohoku and the final cluster (southernmost) in Kyushu.

For each station we choose earthquakes $3.0 < M_{jma} < 6.5$ recorded between $1 < R_{epi} <$ 400 km. The distance range was chosen such that small magnitude records are not overshadowed by noise and additionally to ensure larger magnitudes are statistically well represented. The magnitude range was chosen based on a study by Oth et al. (2010), who show a 1:1 correlation between **M** and M_{jma} in this range. We therefore

take M_{jma} to be a reliable proxy for moment magnitude for $M_{jma} > 3$. We do not consider magnitudes higher than 6.5 due to scale saturation and possible non-linear site effects. The total number of events used at each station are given in Table C1, Appendix C. To pre-process the waveforms, the ObsPy package (Krischer et al., 2015) was utilised. Each acceleration record was converted to WA displacement by convolution with a simulated WA response in the frequency domain (Uhrhammer and Collins, 1990). Prior to convolution a 5% cosine taper was applied in the time domain to reduce edge effects caused by the Fourier transform. Subsequently, ΔM_L were then calculated for each event at all 34 sites (Figure 4.3) using Equation 4.10.

For each site chosen, in a separate processing step, we calculate empirical S/B and surface H/V amplification functions for use in stochastic simulations. Both the S/B and H/V ratios were processed using a range of strong and weak motion data ($2.5 < \mathbf{M} < 6.5$; $0 < R_{epi} < 300$ km). A Konno-Ohmachi filter (Konno and Ohmachi, 1998) with bandwidth parameter b = 80 is applied to smooth the spectra. For each empirical S/B and surface H/V function, the mean and standard deviations (at each frequency) are calculated in log space. Figure C3 (Appendix C) shows all 34 S/B and H/V ratios used in this study.

4.5 Results: Evidence of Magnitude Dependent ΔM_L

ΔM_L is calculated (Equation 4.10) for earthquakes recorded between 1998 and 2016 at all available stations using surface and borehole records (geometric mean of the two horizontal components). In order to model the empirical ΔM_L observed at each of the 34 sites (e.g. Figure 4.4), we perform stochastic simulations (see *section 4.2*). We ran five different stochastic models (four site variable models and one borehole for the ΔM_L), varying model parameters to produce synthetic $\Delta M_{L,STN}$ [$\Delta M_{L,STN}(\mathbf{M})$] for a range of earthquake scenarios at each site. While the observed trends mostly show strong dependence on **M**, there is significant scatter that results from using many different earthquake scenarios. We consider a range of earthquake scenarios by iterating over all combinations of **M** ($2.5 < \mathbf{M} < 7.0$), $\Delta\sigma$ (0.1, 1.0, 10.0 MPa), R_{epi} ($1 < R_{epi} < 400$ km) and κ_{rock} (± 50 %).

Only epicentral distance is considered and we assume events occur at crustal depths (up to roughly 30 km). κ_{rock} is varied by ± 50 % to cover uncertainty in this parameter, accounting for possible path specific attenuation (e.g. 3D heterogeneities). The variability of $\Delta M_{L,STN}(\mathbf{M})$ are represented as box plots at 0.5 magnitude unit intervals. The total variability of $\Delta M_{L,STN}(\mathbf{M})$ predictions is represented by range of the boxplot whiskers, and the centre line is the median prediction. Hence, each boxplot covers the total epistemic variability for all models. A common feature pervasive through all our modelling is that the total variability of the real records cannot be fully explained by $\Delta M_{L,STN}(\mathbf{M})$. However, the degree to which the simulations can account for the observed variability seems to depend strongly on the choice of site amplification model.

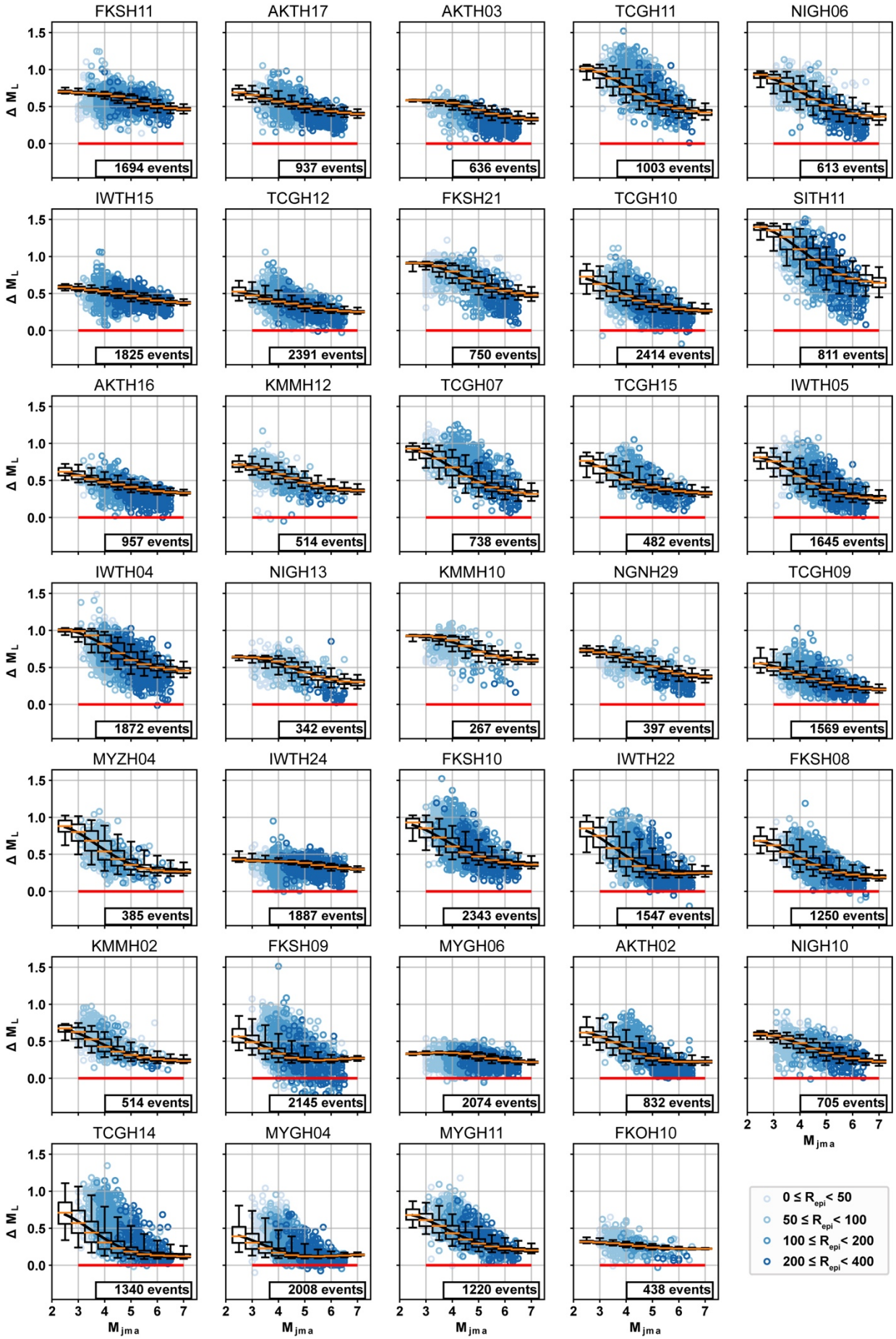

Figure 4.4 – $\Delta M_{L,STN}$ vs $\mathbf{M}(M_{jma})$ for all sites in the study, using the S/B as the site response model. The scatter plot shows the measured difference in Wood-Anderson displacement for the real seismic records ($\Delta M_{L,STN}$). Boxplots show the range (tips) and median (orange line) of predictions of stochastic simulations.

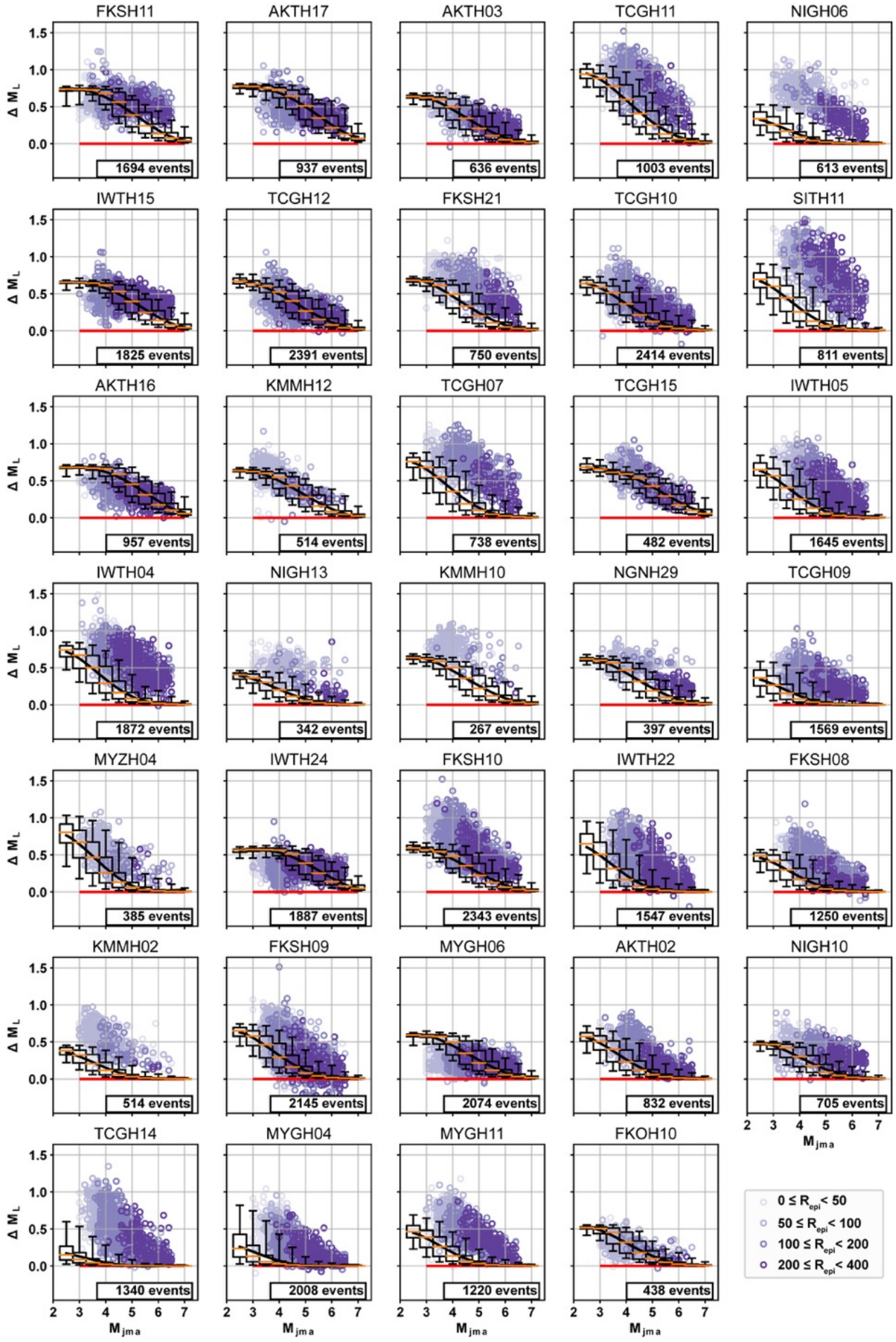

Figure 4.5 - As Figure 4.4 except the site response function is the 1D-SHTF (linear, anelastic).

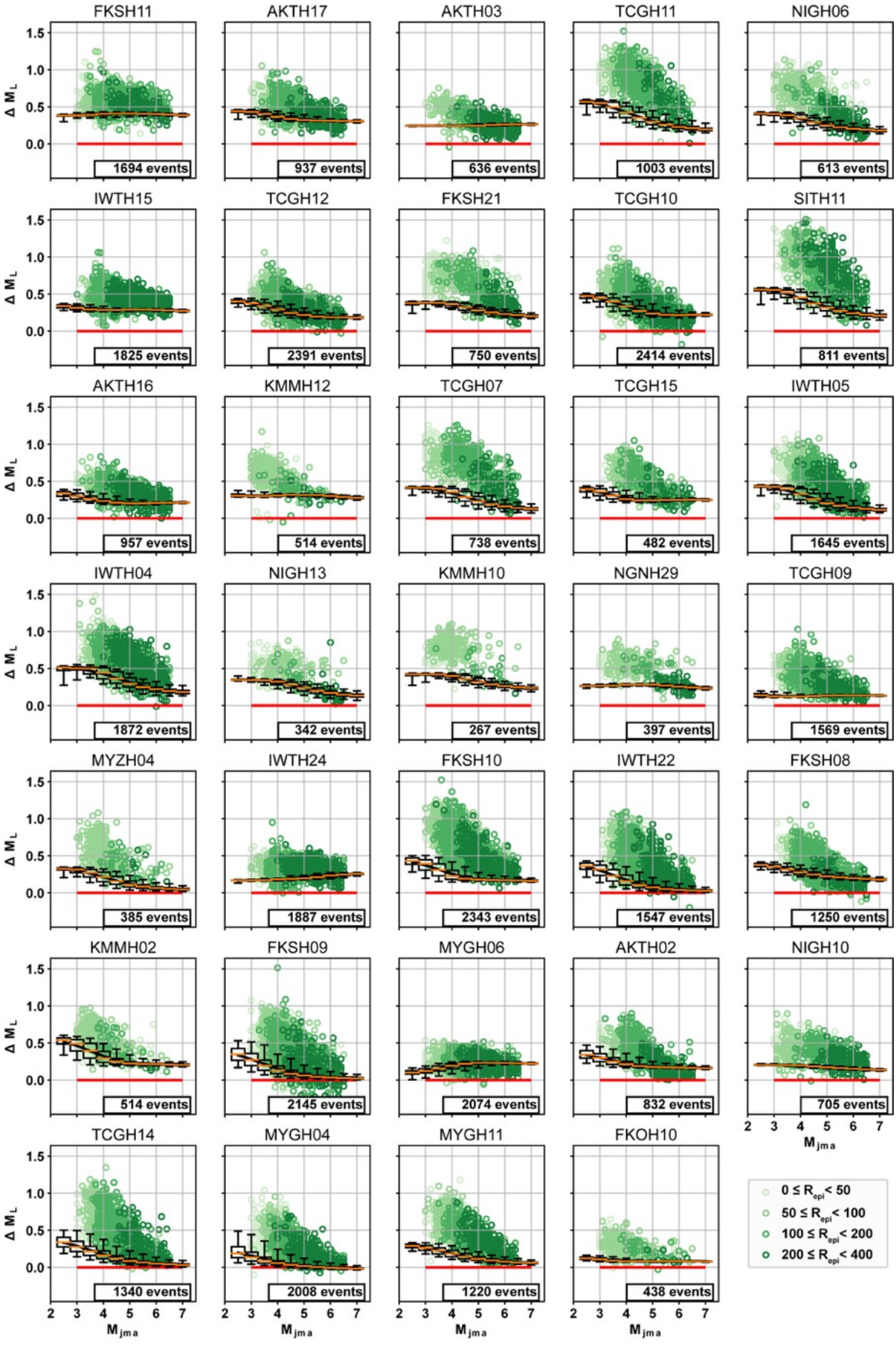

Figure 4.6 – As Figure 4.4 except the site response function is the H/V ratio (geometric mean of horizontal [H] / vertical [Z]component).

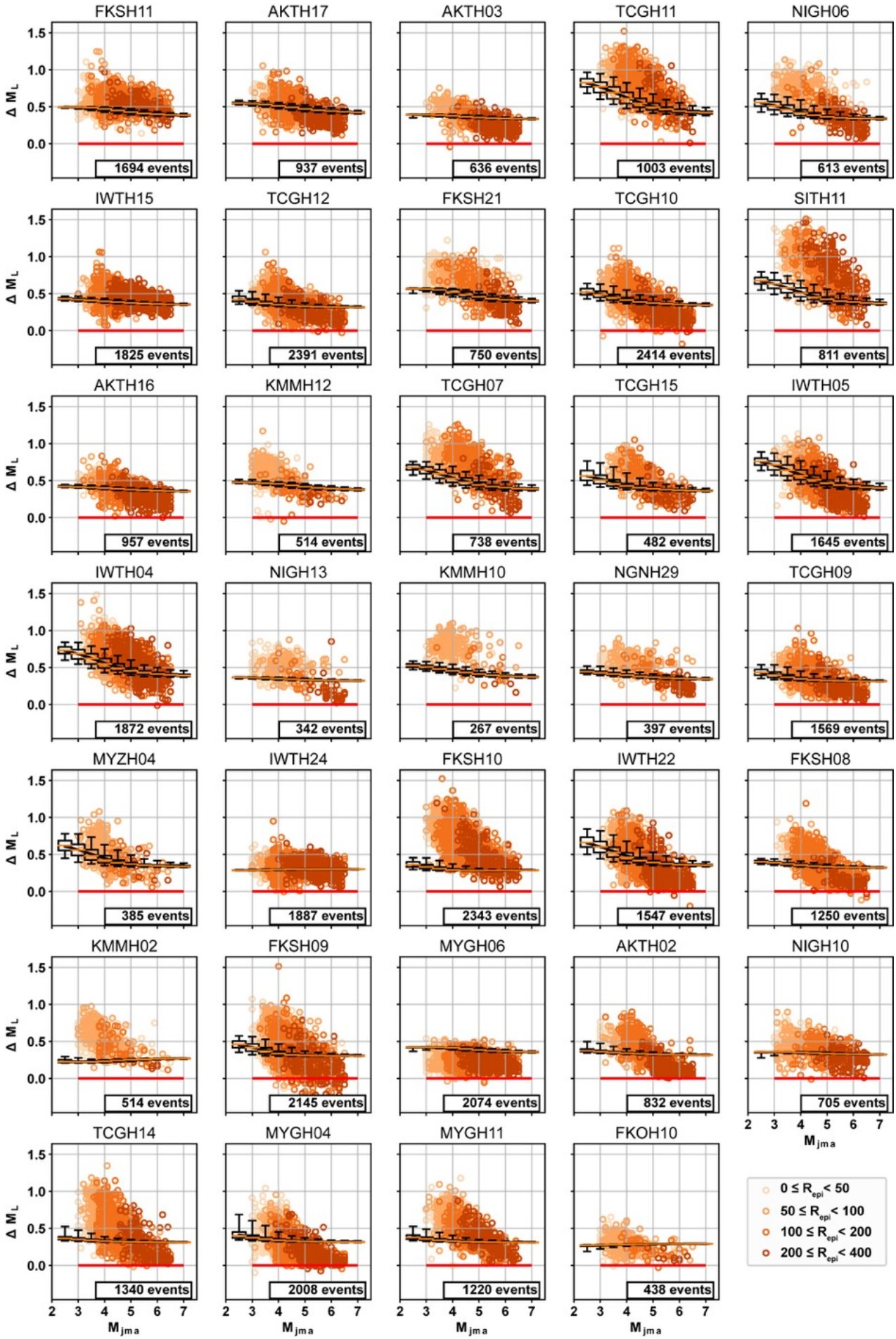

Figure 4.7 - As Figure 4.4 except the site response function is the QWL amplification.

Figure 4.4 displays the real (dots) and synthetic (box plots) ΔM_L for the 34 target sites. In this instance the synthetic data were created using the empirical S/B as the site response model. The curve joining the box plots is a fourth order polynomial fit to the median prediction of the whole suite of $\Delta M_{L,STN}(\mathbf{M})$ predictions for each site. Note that the polynomial has no physical basis and is just a smooth interpolation between median $\Delta M_{L,STN}(\mathbf{M})$ predictions. In most cases the median prediction of all the stochastic models provide a close fit to the centre of each data cloud. Additionally, for a significant proportion of sites, most of the variability may be explained by our choice of parameterisation. Models that fail, only do so at the larger magnitudes ($\mathbf{M} > 6$ to 6.5), as they tend to slightly over-predict the data.

Figure 4.5 shows the stochastic simulations when the 1D-SHTF is used as the site model. Directly comparing to Figure 4.4, the theoretical site model appears to work reasonably well in most cases. The models appear to be more sensitive to **M** than the S/B stochastic models; the trace of the curve is generally less smooth. However, when the models fail there is a tendency to under predict at small magnitudes ($\mathbf{M} < 4$). In general, the 1D-SHTF tends to perform better than the H/V (Figure 4.6) but not the S/B. The total model epistemic uncertainty appears to increase in comparison to the simulations using S/B as the site response metric. These models also all exhibit saturation at large magnitudes, tending toward no change in local magnitude between surface and borehole, as also seen in the sensitivity tests.

Regarding the H/V ratio stochastic simulations, their match to observed data is poor, except for a small number of sites (e.g. TCGH10, TCGH12). It is worth noting that those H/V ratios appear similar to the S/B, however the S/B amplitudes are generally larger (see Figure C3, Appendix C). Mostly, the median models under-predict the observations, performing increasingly poorly at magnitudes below **M** 5, except for a few cases (e.g. KMMH02, MYGH06). Regarding the H/V simulations (Figure 4.6), aleatory variability (as in the variability outside of our error bars) is much greater when compared to Figure 4.4. Finally, Figure 4.7 shows the results when QWL amplification is used as the site response metric. Generally, these simulations fail to match the shape of the empirical data (except for a rare cases). Overall, these stochastic simulations have low variability compared to the other stochastic models. The median model

predictions tend not to follow the unique shape of the site, as the other models do. Instead, mostly the models show weak magnitude sensitivity, except for a couple of sites, where the small magnitudes are almost modelled (e.g. MYZH04). At moderate **M** (4 to 5) most models tend to be in the central portion of the data cloud. See Figure C4, Appendix C, for a closer comparison of four sites we believe broadly represent what is observed in Figures 4.4 – 4.7.

4.6 Discussion

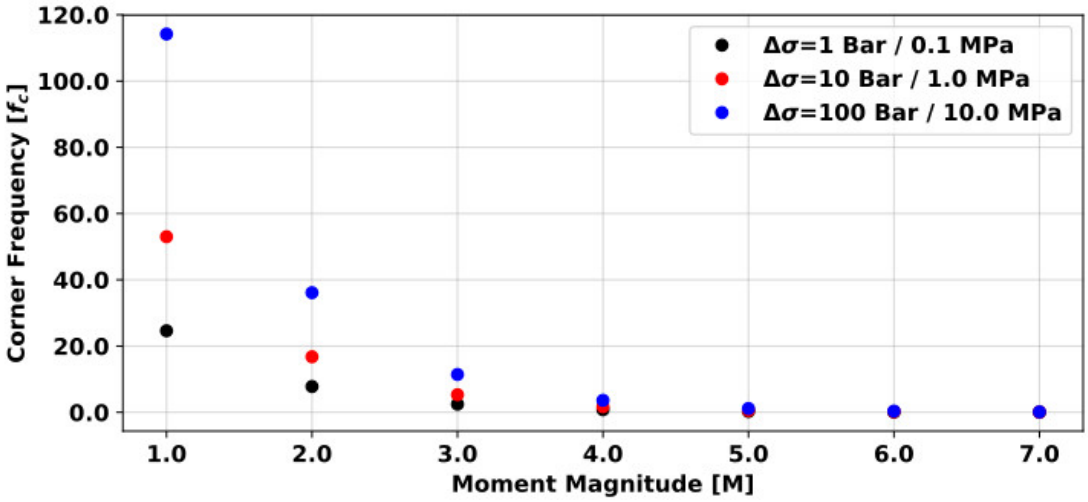

Figure 4.8 - Theoretical corner frequencies for ω^2 Brune source spectrum plotted against **M**. The corner frequencies follow a cubic power law and increase rapidly below **M** 4. This property of the Brune source is significant as the corner frequency shows roughly where the spectral plateau begins. Most of the signal energy in the frequency domain is contained before the corner frequency and explains, in part, why smaller magnitude earthquakes are so sensitive to the κ_0 filter.

The trends in ΔM_L are unique to each site and appear sensitive to the local site response. The empirical S/B (Figure C3, Appendix C) tend to have ramp-like trends leading to f_0 at roughly 8 to 10 Hz, thus, sites amplify over a broad range of frequencies ($2 < f < 25$ Hz). As the corner frequency of smaller events (Figure 4.8) tend towards that of the site f_0 (where amplification > 1 on average), ΔM_L becomes increasingly large for smaller earthquakes. For crustal earthquakes in Japan ($\Delta\sigma \sim 1$ MPa, Oth et al., 2010), the corner frequency of an **M** 4 is approximately 1.7 Hz; this coincides with (1) where the S/B models start to amplify significantly and (2) where ΔM_L begins to increase rapidly (as **M** is reduced). The size of this change depends on the absolute

amplification, the higher the amplification the greater ΔM_L becomes (e.g. SITH11). However, some sites (e.g. IWTH24, MYGH06) show weakly **M**-dependent ΔM_L trends. One possible explanation for this is that level of site amplification, for those sites, is more-or-less constant (usually a factor of 2 or 3). This reasoning is supported we consider how the H/V stochastic models behave in comparison to the S/B. Since the H/V amplification functions are usually 'flatter', they tend to work only for sites with weak **M**-dependence. In those cases, where H/V are almost identical in shape and amplitude to the S/B (e.g. KMMH02) the simulations using H/V work as well as the S/B. There is no clear reason why the S/B and H/V are well matched some cases, but this is beyond the scope of this article and will not be discussed in detail here.

Comparison of the stochastic simulations that used theoretical site models highlight the importance of the particular resonance of each site for $\Delta M_{L,STN}(\mathbf{M})$. Although the QWL and 1D-SHTF are broadly similar, for this application the QWL amplification systematically fails to reproduce the observed ΔM_L. The QWL simulations show reduced sensitivity to all parameters when compared to the other simulations. In sharp contrast, the 1D-SHTF simulations show heightened sensitivity to the parameterisation, which suggests that the resonance peaks of the 1D-SHTF are important and necessary to reproduce the observations. The specific pattern of the observed ΔM_L is matched reasonably well by the 1D-SHTF simulations in nearly all cases. The remaining cases may show a poorer match because either (1) the material property model (e.g. V_S, Q_S) is inadequate or (2) the site features multi-dimensional resonance which is not adequately modelled by the 1D-SHTF or (3) (most likely scenario) a trade-off between (1) and (2).

It is important to note that the event-to-event (inter-event) variability in the empirical amplification functions can be significant, however, we do not consider this in the stochastic models. We chose to do this so there would a fair comparison between stochastic simulations using theoretical and empirical amplification models, because we do not have comparable uncertainty for the theoretical models. It would have been possible to estimate part of the epistemic uncertainty by simulating different incident angles (e.g. Thompson et al., 2012) for site amplification, but we felt this phenomenon was effectively cancelled out in the log-mean empirical amplification functions since

they are derived from many earthquake scenarios. Had we considered the full range of the uncertainty in the empirical amplification functions, it is likely is that more of the variability would have been explained through modelling. Additional variability in site response may be attributed to 3D geometries, topographic focussing effects, and soil non-linearity (Yu et al., 1993).

On Figures 4.4 – 4.7 we plot the observations distinguishing four distance bands (0-50, 50-100, 100-200 and 200-400 km). We note that the distance dependence seems to be unclear in the range $3 < \mathbf{M} < 6$. In our sensitivity tests (Figure 4.2) we also see the minimal distance effect from **M** 6 down to **M** 3 in most cases. It is only lower than **M** 3 that we see a noticeable dispersion caused by distance. For $\mathbf{M} < 3$, attenuation leading to the borehole sensor is much more significant for the smaller, higher frequency earthquakes. Simply, ΔM_L is larger and site amplification has a greater impact at longer distances because the attenuation is more significant before the seismic waves arrive at the borehole. However, it is unlikely you will measure a **M** 1 at 300 km, or even > 100 km, so in practice it is unlikely we would observe the same dispersion as in Figure 4.2, just a decrease across observable distances.

Finally, we address how scenario-dependent station corrections may influence the observed non-linear relationship between **M** and M_L (Hanks and Boore, 1984). Figure 4.9 shows a comparison of **M** - M_L from Goertz-Allmann et al. (2011) (Swiss dataset) and Dost et al. (2018) (Groningen dataset). The Swiss dataset are M_L measurements taken from surface stations and the Groningen M_L come from only borehole records. Both M_L datasets lack the inclusion of station corrections and the magnitudes are averaged over several stations. We expect the Swiss network to experience significant amplification on average. Although several stations in the Swiss networks are placed on hard rock sites, a number of stations (particularly strong-motion) sit on alluvial, low-velocity soils and are certainly affected by complex amplification phenomena. In a few cases 2/3D geometrical effects are also evident (e.g. Michel et al., 2014). Moreover, even for those stations on rock, a non-negligible contribution of the surface geology (surface weathering and fracturing) have been identified (e.g. Poggi et al., 2017). As end members, i.e. broad site effects (Swiss) vs minimal site effects (Groningen), the comparison of these datasets provides an ideal opportunity to

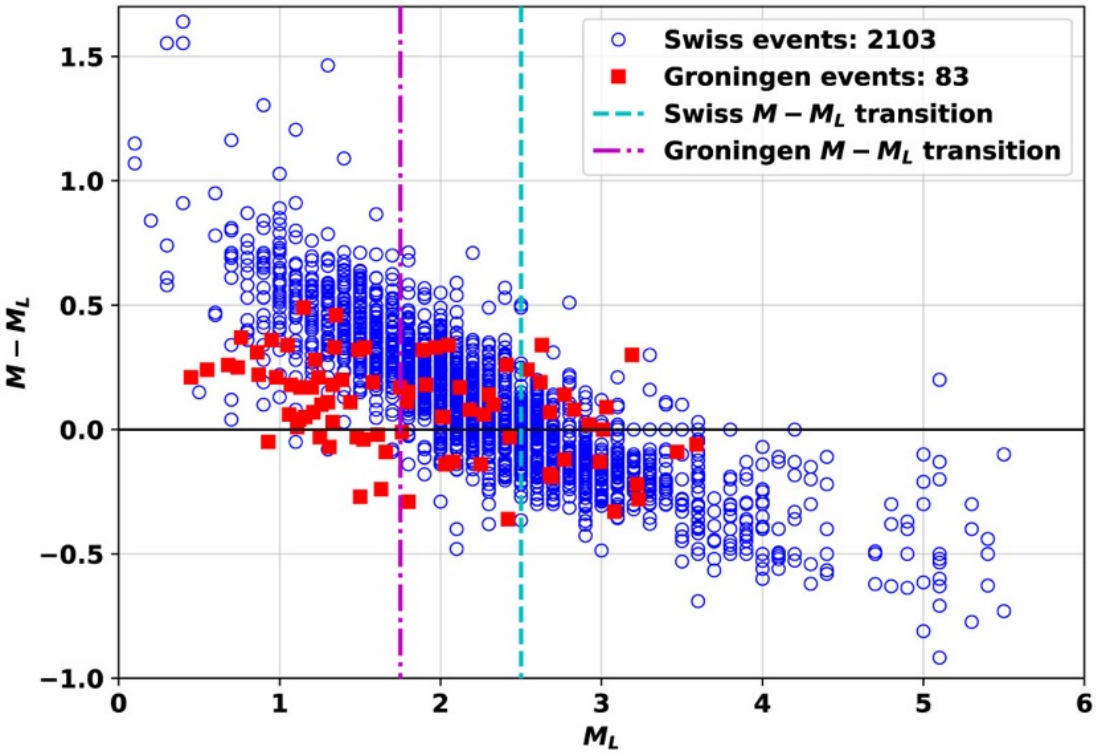

Figure 4.9 - **M** - M_L from Goertz-Allman et al., 2011 (Swiss - blue circles) and from Dost et al. (2018) (Groningen - red squares) showing the non-linear relationship between **M** and M_L. The dashed cyan / dot-dashed lines represents the approximate transition to **M** > M_L for the Swiss / Groningen datasets at M_L ~ 2.5 / 1.75 respectively.

highlight magnitude dependence of site response and that of M_L itself. The non-1:1 scaling of **M** - M_L observed in the Swiss dataset may be explained with our simulations. Although it is unfortunate that our simulations for Japan (e.g Figure 4.4) do not cover the magnitude range of interest (**M** < 3) for this discussion, we note that the simulations in Figure 4.2 and Figure 4.4 are consistent with real data for **M** > 3. We also extended our simulations just outside the data (**M** 2.5) and at a number of sites (e.g. FKSH21, NIGH13, TCGH07). At this small **M** there is a reduction in variance between scenarios and a shallowing of the polynomial slope, suggesting a turning point. This behaviour is also observed in Figure 4.2 for all scenarios. We argue that, for the reasons just stated, the simulations in Figure 4.2 may reasonably represent the observed relationship in the magnitude range of interest for the Swiss and Groningen datasets.

We observed for small earthquakes (**M** < 3), at short distances, there could be a reduction in apparent M_L driven by the site response (Figure 4.2). Since the corner frequency of smaller earthquakes becomes increasingly large (Figure 4.8), the

additional attenuation of the site likely drives the observed behavior in the Swiss dataset, consistent with the findings of Deichmann (2017). For larger earthquakes, in our simulations we observe consistent amplification of M_L induced by the sites, which is also seen in the Swiss dataset. Ideally, the Swiss dataset would look more like the magnitude independent ($M_L > 2$) Groningen dataset (Figure 4.9) after static station corrections are applied. However, this is unlikely, given the clear magnitude dependence of the dataset and magnitude independence of the Swiss station corrections. We postulate that the stochastic simulations developed in this study, ideally those shown in Figure 4.4, may be more suitable than traditional station corrections. For that reason we tentitively term our simulations as magnitude dependent station corrections, $\Delta M_{L,STN}(\mathbf{M})$. However, there is still a magnitude dependence in the Groningen dataset in the magnitude range $M_L < 2$. The Groningen dataset appears to behave closer to that which theory would predict ($\mathbf{M} = M_L$) for $\mathbf{M} > 2$ and $M = (2/3)M_L + C$ (Dost et al. 2018). The difference in Groningen, from most other studies, is that the transition from normal scaling to 2/3 scaling occurs at $1.75 < M_L < 2.00$, rather than between $2 < M_L < 3$ (Swiss transition occurs at $M_L \sim 2.5$). κ_{rock} (attenuation below the borehole) and the path attenuation (Q) is likely still driving $\mathbf{M}$:M_L scaling for small earthquakes, even when measured at depth. However, the transition occurs at a lower than normal M_L, probably due to a lesser whole path attenuation (Edwards et al., 2010; Deichmann et al., 2017). Therefore, an additional attenuation correction would be required, to remove the magnitude dependence at $M_L < 2$ to recover 1:1 scaling. The $\Delta M_{L,STN}(\mathbf{M})$ corrections would only correct as far as we see in the Groningen dataset, such that $\mathbf{M} - M_L = 0$ ($M_L > 2$) and $\mathbf{M} - M_L > 0$ ($M_L < 2$).

4.7 Conclusion

In this study we have explored the role of site response on local magnitude and observed strongly **M** dependent trends between the surface and borehole (assumed bedrock) in real and synthetic data [$\Delta M_{L,STN}(\mathbf{M})$]. In the previous section, we suggested that the stochastic simulations, $\Delta M_{L,STN}(\mathbf{M})$ could tentatively be used as station specific magnitude dependent corrections. A possible approach is summarised in the following steps:

1. Obtain confident values of κ_0 for all sites

   a. The approach of Poggi et al. (2013) can be used to sub-select sites (see *High Frequency Attenuation*)
2. Determine κ_b using iterative approach (see *High Frequency Attenuation*)
   a. κ_b from S/B ratio of earthquake records if possible, otherwise use H/V ratio of earthquake records.
3. Perform stochastic simulations to calculate median/ log(mean) values of $\Delta M_{L,STN}(\mathbf{M})$ for each site (see *Stochastic Models for Synthetic Surface and Borehole Records*)
   a. In order of preference, for the input site response model (used in the stochastic simulations) we suggest using (1) S/B or (2) 1D-SHTF
   b. We do not recommend using the QWL or the H/V to derive $\Delta M_{L,STN}(\mathbf{M})$
4. Estimate network M_L using standard methodology ($M_{L,approx.}$)
5. Convert $M_{L,approx}$ to estimated **M** via scaling relationship
   a. If there is no scaling relationship; if $3 < M_{L,approx} < 5$ take this as equivalent to **M**
6. Re-calculate M_L at each station but account for the site response using the pre-calculated median/log(mean) $\Delta M_{L,STN}(\mathbf{M})$ for that earthquake scenario
7. Calculate the network M_L using new station M_L values
8. Repeat 6-7 until the difference in station corrected M_L values is minimised
   a. Use different values of **M** within the uncertainty bounds of the conversion
   b. If M_L is very similar (after correction) at all stations, then the best possible correction has been found.

We finish by stating some factors about regional M_L scales and station corrections that were important to this study. Firstly, there is some variability in which apriori assumptions are used to derive station terms (e.g. corrections sum to zero, or trusted reference stations). As such, it makes comparison of site effects from different networks difficult, as the calculated station term will depend largely on which assumption was used. This is not ideal because the site term should only be representative of local site conditions. Aside this, station terms derived in this manner do nothing to remove the average site amplification (Pechmann et al., 2007). Finally, there is no simple fix by using only sites with high V_s30 (hard rock), since they still have magnitude dependent trends. Since $\Delta M_{L,STN}(\mathbf{M})$ is derived directly from site effects, the impact of aforementioned points is minimised by deriving site terms using

our proposed methodology. We make note that $\Delta M_{L,STN}(\mathbf{M})$ does not resolve the inequality of **M** - M_L ($M_L < 2$), it would still exist even if most of the site response is removed using $\Delta M_{L,STN}(\mathbf{M})$ station corrections. We would be left with **M** - M_L scaling, similar to that observed in Groningen dataset, since $\Delta M_{L,STN}(\mathbf{M})$ would remove the bulk site response only. An additional attenuation correction would be necessary to recover **M** from M_L in this range since the relationship is controlled by whole path attenuation (not just the site attenuation) for $M_L < 2$.

We were able to show (using real and synthetic data) strong station specific magnitude dependent trends and provide a theoretical framework toward the development of next-generation station/magnitude corrections $\Delta M_{L,STN}(\mathbf{M})$. The corrections reduce the local magnitude to that measured at a borehole station (bedrock), mostly eliminating site effects. This process aims toward reducing the inequality between **M** - M_L and we wish to explore a practical implementation of $\Delta M_{L,STN}(\mathbf{M})$ in future work.

Chapter 5: Conclusions and Future Work

In this section we discuss each chapter, the motivation and how they relate to the project aims in *section 1.1*. We refer back to our aims in a reference-like style. For example, a reference to the first project aim appears like this: (**a1**).

In Chapter 2, all three project goals from *section 1.1* were covered, with an emphasis on **a2**. Utah is an ideal study area because there had already been an effort to produce high quality earthquake catalogues with M_W - M_L and M_C by the UUSS. They had also attempted, in cooperation with the Working Group on Utah Earthquake Probabilities (WGUEP), Utah Geological Survey (UGS), and the United States Geological Survey (USGS), to produce a uniform moment magnitude catalogue to estimate unbiased recurrence rates of earthquakes in and around Utah, for seismic hazard assessment (WGUEP, 2016). This means that UUSS already had an ideal starting dataset and robust scaling relationships that could be used as a reference.

During the study we successfully calibrated the Edwards et al. (2010) method of spectral M_W estimation against UUSS M_W of crustal earthquakes in Utah from moment tensor inversion. We then calculated M_W (and uncertainty, **a2**) using our spectral method and decreased the lower limit of the magnitude range to ~1.5, from ~3.1. Most of this study concerned itself with characterising a local geometrical spreading model that was required to correct the modelled long period spectral levels (from spectral fitting) to the source level. We derived a geometrical spreading model, refined it and provided error bars (by bootstrapping) on the slopes for each piecewise section of the model (**a2**). We discussed the model and attempted to understand it by relating the sections to physical processes such as focussing / defocussing and the influence of body-wave versus surface-wave phases. We addressed issues with near-field geometrical spreading, which are debated (Atkinson, 2012), and were able to show that near-field geometrical spreading can be $< R^{-1}$ (where R is distance in km), contrary to other studies (**a3**). Some studies force $> R^{-1}$ in the near-field (e.g. Malagnini and Herrmann, 2000; Atkinson, 2004; Jeon and Herrmann, 2004), which could potentially introduce uncertainty to correction of near-field records (**a1**). Thereby allowing us to more confidently use near-field recordings and reduce uncertainty on our magnitude

predictions, which becomes increasingly important for smaller earthquake sources (**a2**).

Ultimately, using our new catalogue we were able to re-evaluate and expand the M_W – M_L and M_C scaling relationships (developed by Arabasz et al., 2016) that were used to develop a uniform moment magnitude catalogue (**a3**). We evaluated the scaling relationships using two versions of our M_W dataset for two geometrical spreading models (Holt et al. [O] and [R]). We found bilinear relationships (for which we provide uncertainty on the slope and intercept for each piecewise segment), similar to Staudenmaier et al. (2018). Additionally, our relations also have theoretical basis (e.g. Deichmann, 2017) and support the results of similar studies that find slopes of ~2/3 for M_W – M_L scaling (M_L < 3) empirically. Ultimately, we recommended our Holt et al. [R] geometrical spreading model for Utah, along with related products (**a2** and **a3**).

In Chapter 3 we focus on **a1** and **a3** but also address **a2** by re-evaluating the local magnitude (M_L) scale for the Yellowstone National Park, USA region. We were motivated to do this because a cursory study (looking at station – event magnitudes) in 2007 by UUSS suggested the distance correction might be inappropriate (**a3**) (UUSS, personal comms.). Additionally, when the same analysis was performed, using an updated catalogue (up to October 2018), we achieved a similar result (see *section 3.4*, Figures 3.12a and 3.12b). To address this, we performed a constrained non-parametric inversion (Savage and Anderson, 1995) and found a complex distance correction which was stable over 1000 bootstrap replications. We then compared M_L to trusted M_W solutions from the UUSS and Saint Louis University (SLU) and found our M_L had a better agreement to M_W than the old M_Ls. This was further evidence that suggested that the old distance correction was not adequate to account for attenuation in Yellowstone (**a3**). We also derived new station corrections, for which we provided uncertainty and recalculated M_L (and uncertainty) for ~3950 earthquakes (**a2**).

We then analysed residuals between old (UUSS M_L) and new (YS M_L) local magnitudes. Interestingly, we found that UUSS M_L and YS M_L agreed well (within ~0.01 magnitude units on average) over UUSS M_L 1.0 to 3.6. However, outside of these ranges UUSS M_L could be up to ~0.2 magnitude units (m.u.) smaller on average. Given that our new M_Ls agreed well with M_W, along with the close analysis of the

distance correction (see *section 3.5*), confirmed that: (1) the old M_L scale was underestimating large magnitudes with implications in hazard assessment, and (2) the Richter (1958) distance correction was not appropriate (**a3**).

We suggested that the reason M_L is so well matched (even though the new distance correction is so different) over such a broad range is twofold: (1) the Richter (1958) distance correction was akin to a smooth average of our new distance correction and (2) the station corrections of Pechmann et al. (2007) minimised to correct for the residual difference between actual attenuation and the Richter (1958) distance correction (see *section 3.5*). We hypothesise that because UUSS M_L 1 to 3.5 appears to make up the bulk of data in the catalogue, it is probable that the station corrections mainly minimised to reduce the effects of the distance correction on individual station magnitude estimates in this range. What helped this here was that those earthquakes were large enough to be recorded over a sufficient distance, such that the average M_L had little distance dependence. For earthquakes with UUSS M_L outside of this range, they depended more on specific parts of the distance correction, so the distance dependence would not cancel out. For a similar reason, the previous UUSS station corrections likely only help to cancel out some of distance dependence when many of them, spread out over a wide distance, are used (see *section 3.5*).

Finally, we commented on the fact that this is a weakness in the derivation of station corrections for local magnitude (**a1**). The fact that the station corrections might have been over-correcting undermines the assumption that they should only be related to repeatable site effects. Unfortunately, there are currently no site data that can be used to validate our new station corrections, but we specifically aim to address this problem in a future study. Also, we aim to look at 1D simulations using the Yellowstone velocity model to see if it is possible to reproduce the observed attenuation through modelling.

In Chapter 4 we address our first and final aims (**a1** and **a3**) by developing a new method of deriving station corrections for use with local magnitude using only site information (e.g. surface-to-borehole ratios, H/V ratios, site response modelling etc.). We were motivated by one of our conclusions in Chapter 3, that apriori assumptions about how station corrections are derived (e.g. residual to distance correction) could bias local magnitude.

We hypothesised that derivation of station corrections developed only with site information would reduce the trade-off between the distance correction and station corrections. To that end we developed stochastic models that quantify the difference in M_L at an arbitrary station ($\Delta M_{L,STN}$), between the surface and some reference horizon below the surface (e.g. borehole station in bedrock), beyond which site effects are assumed minimal. We compared our models with $\Delta M_{L,STN}$ (difference between M_L at surface and borehole) from KiK-Net data and found scenario-specific dependence (dominantly magnitude - distance) of ΔM_L influenced by local site response $\Delta M_{L,STN}(\mathbf{M})$. (**a3**) This scenario-dependence may be captured by variability in typical, 'static' station corrections but uncertainty in station corrections are rarely, if at all, used in magnitude calculations. It may be indeed necessary to move away from static station corrections and consider scenario-specific corrections (**a1**), particularly for those stations with strong site effects. It is unfortunate that the National Research Institute for Earth Science and Disaster Prevention (NIED) does not currently use a local magnitude scale like Richter M_L (1958), therefore they have not developed station corrections and a distance correction that we could use to test our new station corrections.

In future work we will test the validity of $\Delta M_{L,STN}(\mathbf{M})$ in network which has a developed local magnitude scale. The ideal network would have surface and borehole sensors and known site attenuation (κ_0) so we can repeat our most successful method of deriving $\Delta M_{L,STN}(\mathbf{M})$. However, we found that 1D site modelling was promising and that a likely the downfall was due to the simplicity of the velocity models provided by NIED. To that end, the network ran by the Swiss Seismological Service (SED) may prove to be an ideal candidate. Firstly, they have developed a local magnitude scale (Goertz-Allmann et al., 2011). Secondly, SED has made a significant effort toward characterising the site response. At many of their stations they provide empirical site amplification models (ESM), H/V ratios, detailed 1D velocity models (Michel et al., 2014) and κ_0 at some sites (Edwards et al., 2015).

In summary, the work covered in this thesis has contributed successfully toward all of our project aims. For Utah, we have provided new magnitude products (seismic catalogues, scaling relationships) with associated uncertainty which may be used for the next seismic hazard assessment in Utah. In Yellowstone we revised the distance

correction which directly resulted in improving M_L for large magnitude earthquakes (large enough to be significant to hazard) where the old scale proved inadequate. We demonstrated how using a distance correction that was not calibrated purposefully, can have negative impact on magnitude and introduce uncertainty to magnitude related products. This bled into the determination of station corrections, adding an additional layer of epistemic uncertainty. We developed a novel framework to derive station corrections independent of the distance correction using only site information. We improved our understanding of how local site effects influence M_L and how our current assumptions may introduce bias to magnitude determination.

Appendix A

Tables

Table A1 – Earthquakes with UUSS M_W used for calibration of the method. The SgH Spectra M_W values were calculated using the Holt et al. [R] (see Table 2.1) apparent geometrical spreading model.

UTC (year-month-day hr:min:sec)	Lat (°)	Lon (°)	Depth (km)	UUSS M_W	SgH Mw	UUSS M_L	UUSS M_C
1998-01-02 07:28:29	38.24	-112.52	9	4.48	-	4.44	4.62
1998-04-10 20:07:16	38.42	-113.00	6	3.78	-	3.87	3.92
1998-06-18 11:00:39	37.99	-112.50	11	4.07	-	3.93	4.21
1999-01-08 15:24:15	38.77	-111.55	5	3.85	-	3.68	4.13
1999-09-09 10:07:41	38.86	-111.98	6	3.80	-	3.53	3.51
1999-09-09 11:38:43	38.86	-111.98	7	3.88	-	3.58	3.74
1999-10-11 22:43:14	38.77	-112.02	5	4.03	-	3.75	4.44
1999-10-22 17:51:15	38.09	-112.74	3	4.15	-	4.11	4.35
1999-12-22 08:03:31	38.76	-111.55	4	3.86	-	3.74	4.09
2000-01-30 14:46:53	41.52	-109.78	1	4.31	-	4.25	4.47
2000-03-07 02:16:04	39.75	-110.84	1	3.92	-	4.16	4.43
2000-05-27 21:58:19	38.30	-108.88	3	3.80	-	4.41	4.38
2000-08-30 08:21:57	42.00	-112.60	6	3.66	3.70	3.63	3.51

2001-02-23 21:43:50	38.73	-112.56	10	4.18	-	3.99	3.92
2001-02-24 10:54:40	38.73	-112.54	9	3.76	-	3.61	3.43
2001-07-19 20:15:33	38.74	-111.55	3	4.30	-	4.17	4.55
2001-11-19 21:36:25	38.55	-112.47	4	3.86	3.77	3.62	3.98
2002-07-28 19:38:40	41.74	-111.38	4	3.67	3.62	3.59	3.68
2003-01-03 05:02:12	41.27	-111.80	14	3.93	3.83	3.62	3.87
2003-04-17 01:04:18	39.51	-111.90	2	4.28	4.44	4.24	4.73
2003-07-12 01:54:40	41.29	-111.61	14	3.54	3.54	3.50	3.84
2003-12-27 00:39:24	39.65	-111.94	9	3.80	3.69	3.64	3.76
2003-12-27 00:40:41	39.64	-111.95	7	3.81	3.69	3.58	3.92
2003-12-27 00:43:23	39.65	-111.96	7	3.85	3.70	3.68	3.52
2004-11-07 06:54:59	38.25	-108.91	1	3.68	3.72	4.09	3.90
2005-06-24 13:01:33	37.52	-112.55	4	3.74	3.56	3.55	3.82
2006-01-27 06:47:12	39.17	-110.88	14	3.59	3.70	3.58	3.99
2006-07-14 17:06:01	42.41	-111.51	9	4.00	4.02	3.96	3.81
2006-09-02 19:54:59	42.41	-111.51	10	3.60	3.59	3.57	3.70

2007-02-25 03:52:20	42.45	-110.69	7	3.97	3.79	3.82	4.07
2007-06-11 01:03:46	37.49	-114.02	8	3.76	3.83	3.93	3.72
2007-08-06 08:48:40	39.46	-111.23	1	4.16	-	3.92	4.48
2007-08-18 13:16:30	38.07	-113.32	6	3.71	3.88	3.93	3.91
2007-09-01 18:32:02	41.64	-112.31	10	3.83	3.82	3.92	3.75
2007-11-05 21:48:00	39.35	-111.65	11	3.82	3.82	3.91	3.96
2008-06-06 20:09:59	37.36	-109.47	13	3.29	3.51	3.66	3.80
2008-07-14 23:50:53	39.72	-111.30	12	3.17	3.34	2.87	2.92
2010-01-04 16:24:03	37.60	-113.04	12	3.91	3.96	4.12	3.89
2010-04-14 18:58:45	38.03	-111.10	16	3.75	3.94	3.92	4.35
2010-04-15 23:59:38	41.70	-111.09	3	4.59	4.60	4.90	4.51
2010-08-18 12:52:31	37.64	-113.22	9	3.66	3.65	3.80	3.67
2011-01-03 12:06:36	38.25	-112.34	5	4.47	4.44	4.56	4.95
2011-01-06 22:31:04	38.26	-112.33	8	3.43	3.59	3.46	3.33
2011-01-07 22:51:07	38.26	-112.33	5	3.39	3.26	3.26	2.98
2011-01-12 08:46:29	38.24	-112.34	3	3.82	3.61	3.58	3.97

2011-01-26 05:10:11	42.42	-111.50	7	3.62	3.69	3.73	3.54
2011-07-22 07:05:35	39.92	-111.80	9	3.65	3.64	3.30	3.55
2011-07-26 03:38:26	42.05	-111.56	7	3.60	3.68	3.65	3.53
2011-09-28 06:31:20	37.91	-112.05	16	3.67	3.61	3.49	3.73
2011-11-10 04:27:45	39.30	-111.15	4	3.96	4.05	3.90	4.51
2012-02-04 11:27:03	40.02	-111.53	9	3.67	3.81	3.63	3.75
2012-02-12 04:18:59	37.86	-112.40	10	3.67	3.61	3.50	3.67
2012-02-12 03:06:09	37.86	-112.40	3	3.53	-	3.18	3.11
2012-04-12 03:29:22	37.81	-112.09	11	4.13	4.24	4.19	4.40
2012-07-13 19:53:16	41.90	-111.92	2	3.71	3.48	3.52	3.44
2012-07-31 10:27:28	39.01	-111.50	1	3.90	4.08	3.67	4.45
2012-08-07 05:07:15	44.75	-111.10	5	3.25	-	3.23	2.97
2012-09-05 22:52:51	44.78	-110.94	10	3.60	3.24	3.49	3.51
2012-11-04 06:04:20	39.45	-111.89	12	3.29	-	3.09	3.17
2013-01-24 04:46:39	38.32	-108.99	4	4.00	4.21	4.33	4.73
2013-02-08 02:47:02	37.77	-113.13	2	3.84	3.74	3.70	4.36

2013-03-01 07:50:22	42.54	-111.08	9	3.93	3.89	3.99	4.26
2013-05-06 03:20:57	42.62	-111.95	14	3.59	3.83	3.50	3.47
2013-09-10 12:46:12	44.32	-110.62	2	4.08	-	3.31	3.24
2013-09-21 13:16:33	42.98	-109.12	80	4.80	-	4.94	4.98
2013-10-17 16:19:20	41.60	-111.68	9	3.77	3.69	3.63	3.72
2014-01-28 16:20:11	37.33	-114.12	11	3.86	3.90	4.11	4.10
2014-03-14 16:03:51	40.56	-111.27	9	3.39	3.40	3.20	3.33
2014-03-30 12:34:39	44.77	-110.68	8	4.83	-	4.72	4.46
2014-04-04 09:38:19	37.35	-113.80	11	3.51	3.32	3.48	3.24
2014-06-12 04:34:04	40.89	-111.68	11	3.34	3.34	3.30	3.31
2014-06-29 00:56:22	39.44	-111.44	5	4.12	4.14	4.15	4.49
2014-12-29 06:08:18	39.66	-111.97	3	3.94	4.01	3.66	4.16
2015-05-23 05:14:28	37.45	-114.18	11	3.41	3.37	3.41	3.39
2015-07-04 16:00:03	37.85	-112.47	4	4.09	3.96	3.91	4.26
1999-08-20 13:50:25	44.79	-112.79	15	4.83	-	5.35	5.00
2001-04-21 17:18:56	42.92	-111.39	9	5.17	-	5.25	4.91

2005-07-26 04:08:36	45.34	-112.61	9	5.49	-	5.73	5.83
2008-02-21 14:16:02	41.15	-114.87	11	5.93	-	6.05	6.06
2010-08-05 00:04:17	43.60	-110.39	8	4.84	-	5.17	5.34
1992-09-02 10:26:21	37.10	-113.51	15	5.36	-	5.96	5.43

Figures

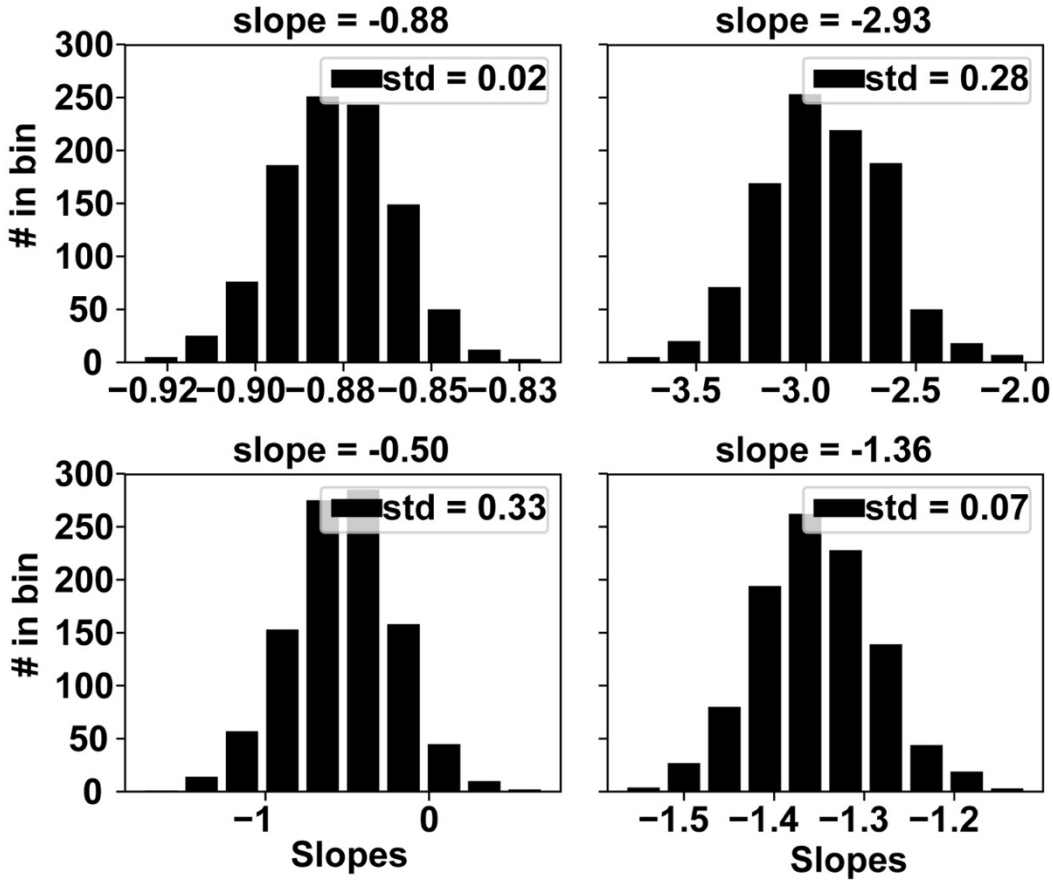

Figure A1 - Bootstrap uncertainty histograms of slopes of the original geometrical spreading model (Holt et al. [O]).

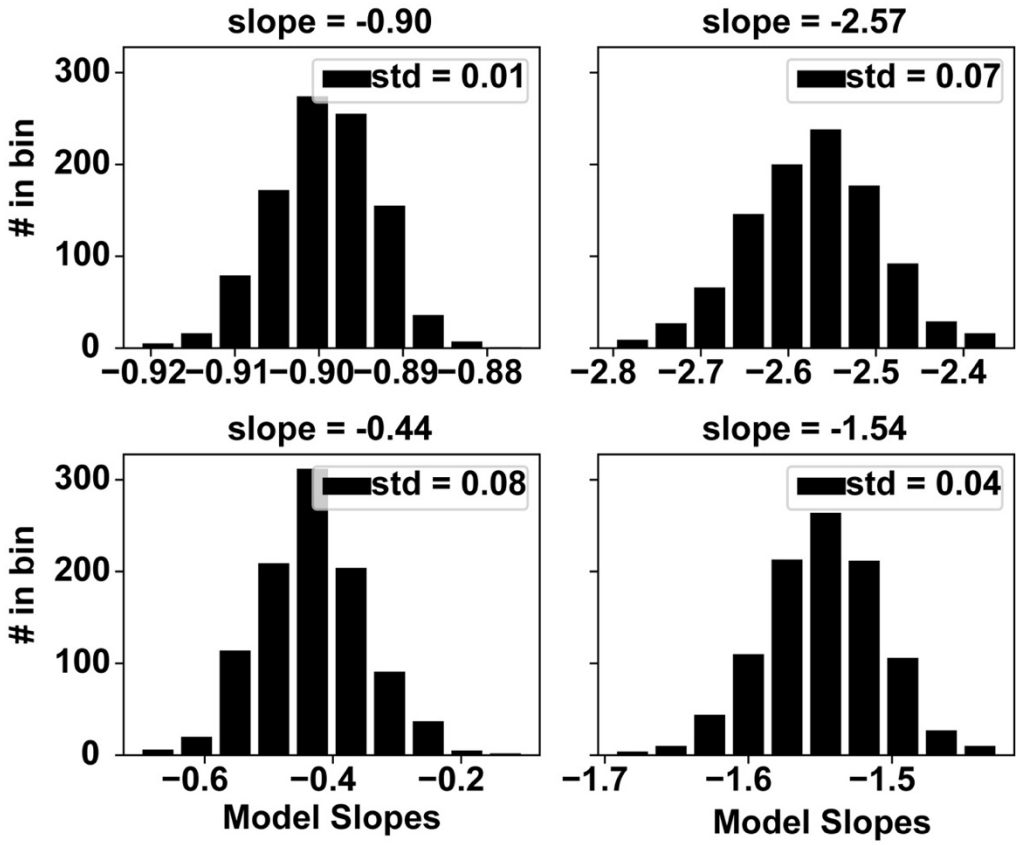

Figure A2 - Bootstrap uncertainty histograms of slopes of the refined geometrical spreading model (Holt et al. [R]).

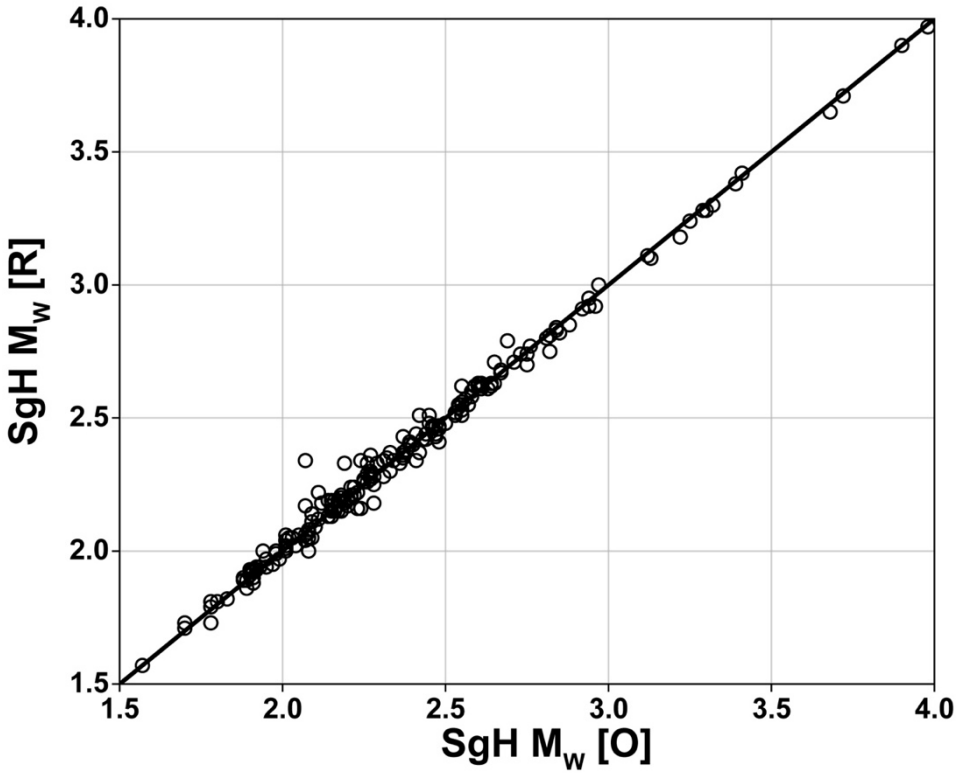

Figure A3 - Comparison between SgH Spectral Mw before [O] and after [R] refinement of the geometrical attenuation model.

Appendix B

Comments

In Chapter 3, section 3.2 (Data and Processing) we mention that records ≤ epicentral distance (R_{EPI}) of 50 km must have well resolved focal depths (h) to be used. In the following we explain why this distance was important. We needed to know at what distance hypocentral distance becomes insensitive to focal depth in the Yellowstone region.

First, consider an arbitrary hypocentral distance, r km, for an earthquake of depth, z km, at epicentral distance, v km such that:

$$r = \sqrt{z^2 + \Delta^2} \tag{B.1}$$

The sensitivity of r to z from equation B.1 is given by the derivative:

$$\frac{dr}{dz} = \frac{0.5}{\sqrt{z^2 + \Delta^2}} 2z = \frac{z}{\sqrt{z^2 + \Delta^2}} = \frac{z}{r} \tag{B.2}$$

We need to know the distance beyond which $\frac{dr}{dz}$ is less than some threshold value. From B.1 this should be a function of focal depth. We assume a focal depth of 10.4 km, the median focal depth (8 km) of the Yellowstone catalogue corrected to the surface by adding the average elevation of 2.4 km, therefore z = 10.4 km (we use z = 10 km for simplicity). From B.1 the hypocentral distance, below which well-constrained focal depths are required are given by (r_c):

$$r_c = {}^{z}\Big/\frac{dr}{dz} = {}^{10}\Big/\frac{dr}{dz} \tag{B.3}$$

Finally, we must define what a sensible value for $\frac{dr}{dz}$ is. Our inversion at minimum is solved at 5 km intervals via linear interpolation; therefore, hypocentral distance needs to be accurate to within 2 to 2.5 km. It seems reasonable to require $\frac{dr}{dz}$ to be less than $\frac{2}{10}$ to $\frac{2.5}{10}$ km, or 0.2 to 0.25. Substituting this range into B.3 yields r_c = 40 to 50 km. We

chose the upper limit of 50 km to be conservative. The corresponding epicentral distance would be $\Delta_c = r^2_c + z^2 = (50^2 + 10^2)^{0.5} \approx 50$ km to the nearest 2 to 2.5 km. Hence, we only use records that have epicentral distance $\Delta < 50$ km if they have a well resolved focal depth.

Equations

Example $\mathbf{d} = \mathbf{G}\cdot\mathbf{m}$ for non-parametric inversion.

$$\begin{bmatrix} \log_{10}(A_{1,1,1}) \\ \log_{10}(A_{1,1,2}) \\ \vdots \\ \vdots \\ \vdots \\ \log_{10}(A_{1,1,J}) \\ \log_{10}(A_{1,2,1}) \\ \log_{10}(A_{1,2,2}) \\ \vdots \\ \log_{10}(A_{1,I,2}) \\ \vdots \\ \vdots \\ \vdots \\ \log_{10}(A_{\widehat{N},I,J}) \end{bmatrix} =$$

$$\begin{bmatrix} a_{1,1,1} & a_{2,1,1} & 0 & \dots & 0 & 0 & 1 & 0 & \dots & 0 & 1 & 0 & \dots & 0 \\ a_{1,1,2} & a_{1,1,2} & \vdots & \dots & \vdots & \vdots & 1 & 0 & \dots & 0 & 0 & 1 & \dots & 0 \\ \vdots & \vdots & \vdots & \dots & \vdots & \vdots & \vdots & \vdots & \dots & 0 & 0 & 0 & \dots & 0 \\ a_{1,I,J} & a_{2,I,J} & 0 & \dots & \vdots & \vdots & 0 & 0 & \dots & 1 & 0 & 0 & \dots & 1 \\ 0 & a_{2,1,1} & a_{3,1,1} & \dots & \vdots & \vdots & 1 & 0 & \dots & 0 & 1 & 0 & \dots & 0 \\ \vdots & \vdots & \vdots & \dots & \vdots & \vdots & 0 & \vdots & \dots & \vdots & 0 & \vdots & \dots & \vdots \\ \vdots & \vdots & \vdots & \dots & \vdots & \vdots & \vdots & \vdots & \dots & \vdots & \vdots & \vdots & \dots & 0 \\ \vdots & a_{2,I,J} & a_{3,I,J} & \dots & \vdots & \vdots & 0 & 0 & \dots & 1 & \vdots & \vdots & \dots & 1 \\ \vdots & 0 & \vdots & \dots & \vdots & \vdots & \vdots & \vdots & \dots & 0 & \vdots & \vdots & \dots & 0 \\ \vdots & \vdots & 0 & \dots & \vdots & \vdots & \vdots & \vdots & \dots & \vdots & \vdots & \vdots & \dots & \vdots \\ \vdots & \vdots & \vdots & \dots & \vdots & \vdots & \vdots & \vdots & \dots & \vdots & \vdots & \vdots & \dots & \vdots \\ 0 & 0 & 0 & \dots & a_{N-1,I,J} & a_{N,I,J} & 0 & 0 & \dots & 1 & 0 & 0 & \dots & 1 \end{bmatrix} \begin{bmatrix} -\log_{10}(A_0)_1 \\ -\log_{10}(A_0)_2 \\ -\log_{10}(A_0)_3 \\ \vdots \\ -\log_{10}(A_0)_{N-1} \\ -\log_{10}(A_0)_N \\ M_{L,1} \\ M_{L,2} \\ \vdots \\ M_{L,I} \\ S_1 \\ S_2 \\ \vdots \\ S_J \end{bmatrix}$$

(B.4)

Tables

Table B1 – Table of Station Corrections used and derived for stations in this study. The station names with * are those that were fixed for the inversion.

Station	Latitude (°)	Longitude (°)	UUSS Sta Corr	YS Sta Corr
AHID*	42.765400	-111.10040	-0.43	-0.43
BOZ*	45.596970	-111.62967	0.17	0.17
BUT*	46.010834	-112.55666	-0.23	-0.23
BW06*	42.766700	-109.55830	-0.15	-0.15
LKWY	44.565200	-110.40000	0.06	0.02
LOHW	43.612400	-110.60380	-	0.01
REDW	43.362400	-110.85180	-	-0.04
YEE	44.485300	-109.89690	-	-0.48
YFT	44.451330	-110.83583	0.20	0.22
YHB	44.750800	-111.19620	0.18	0.03
YHH	44.788330	-110.85050	-	0.15
YHL	44.850900	-111.18300	-	0.23
YHR	44.106000	-110.08160	-	0.10
YMP	44.740170	-110.15600	-	0.14
YMR	44.668670	-110.96500	-0.38	-0.07
YNE	45.007600	-110.00800	-	-0.19
YNR	44.715500	-110.67917	0.35	0.07
YPP	44.271000	-110.80450	-	-0.09
YTP	44.391830	-110.28500	-	0.55
YUF	44.712600	-110.51170	0.61	-0.01

Figures

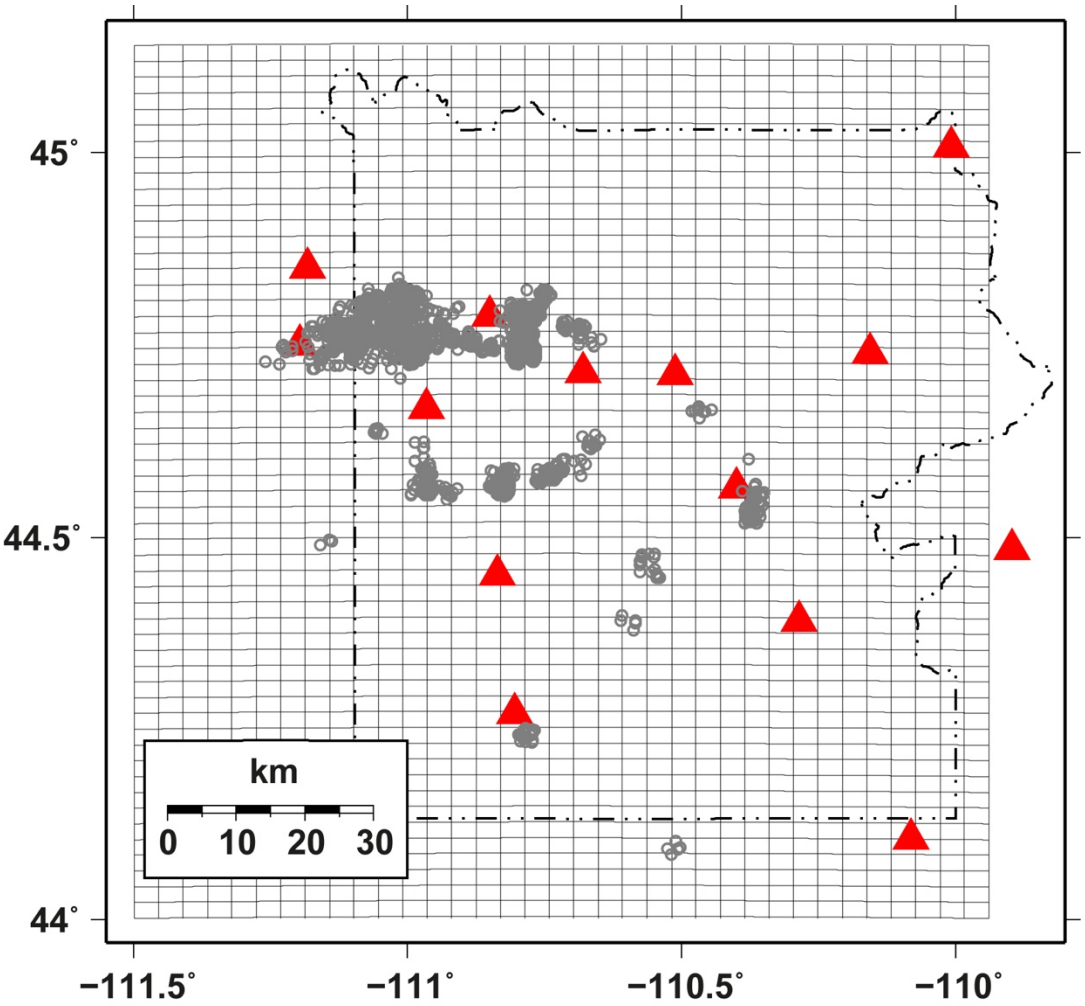

Figure B1 – Map of earthquakes that were removed (grey empty circles) from the catalogue after geographic weighting.

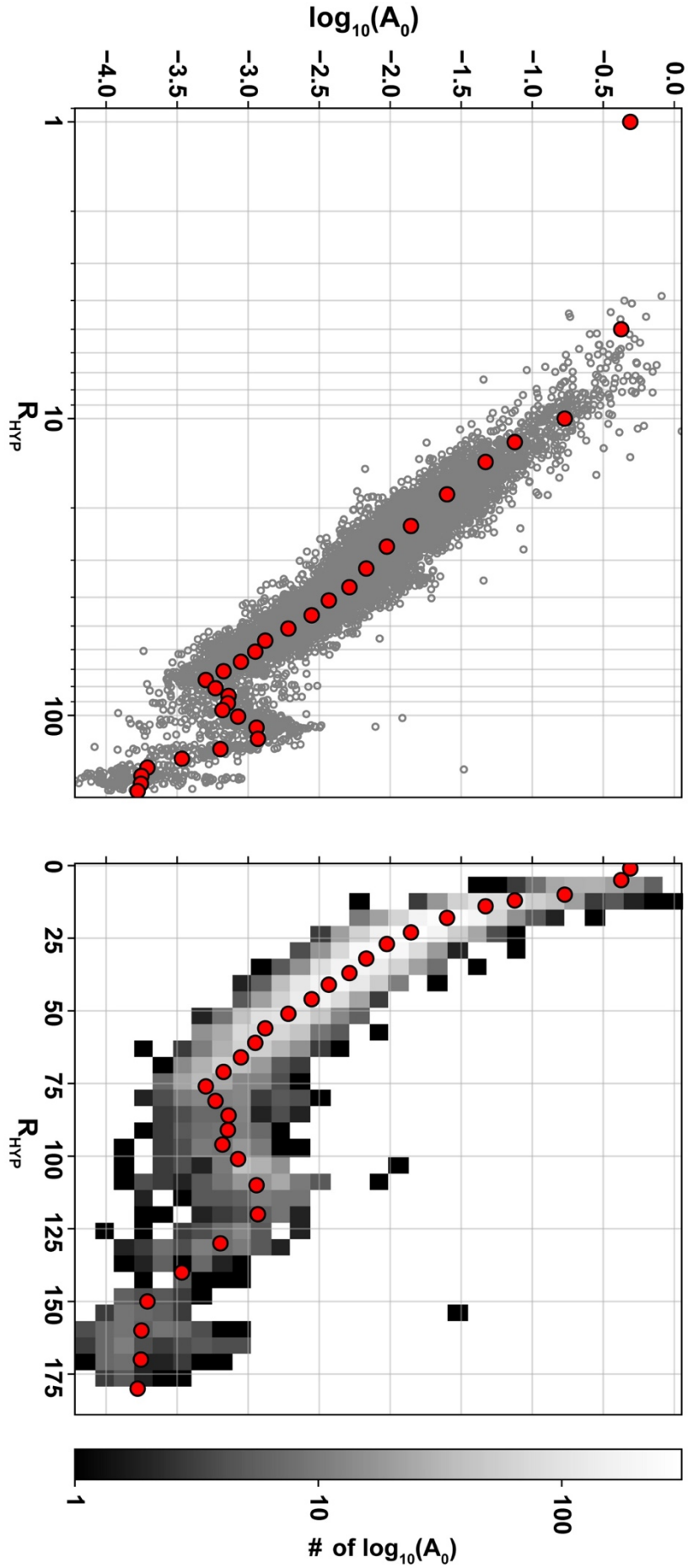

Figure B2 – Final Yellowstone distance correction ($logA_0$;red circles) plotted in log-log (a) and log-lin (b) space. Subplot a) shows the absolute $logA_0$ values (data corrected to $log(A_0)$ by adding M_L and subtracting S_j) as grey circles. Subplot b) shows the $logA_0$ values binned as a 2D histogram.

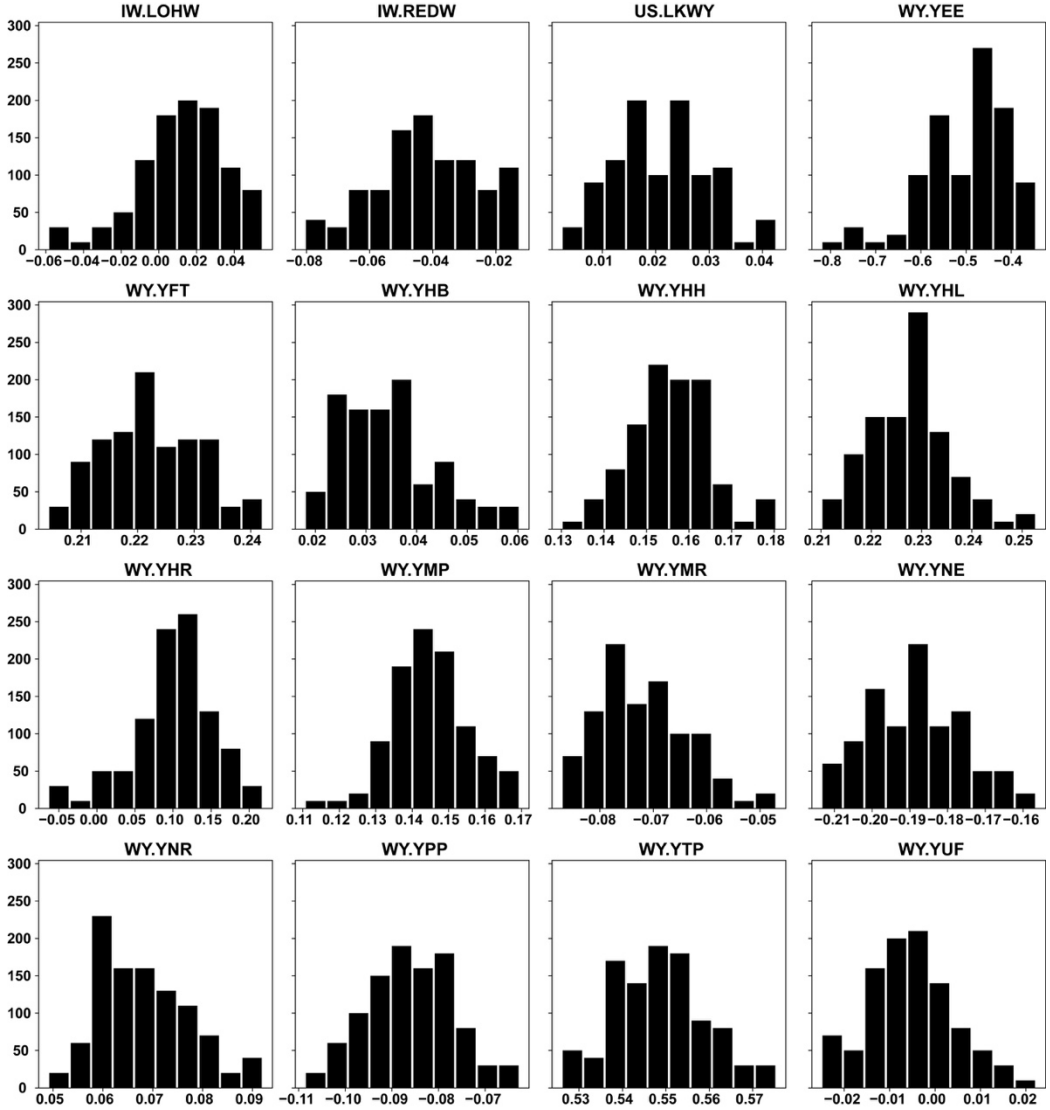

Figure B3 – Histograms of the inverted station corrections (Figure 3.9) for 1000 bootstrap replications with 10% replacement.

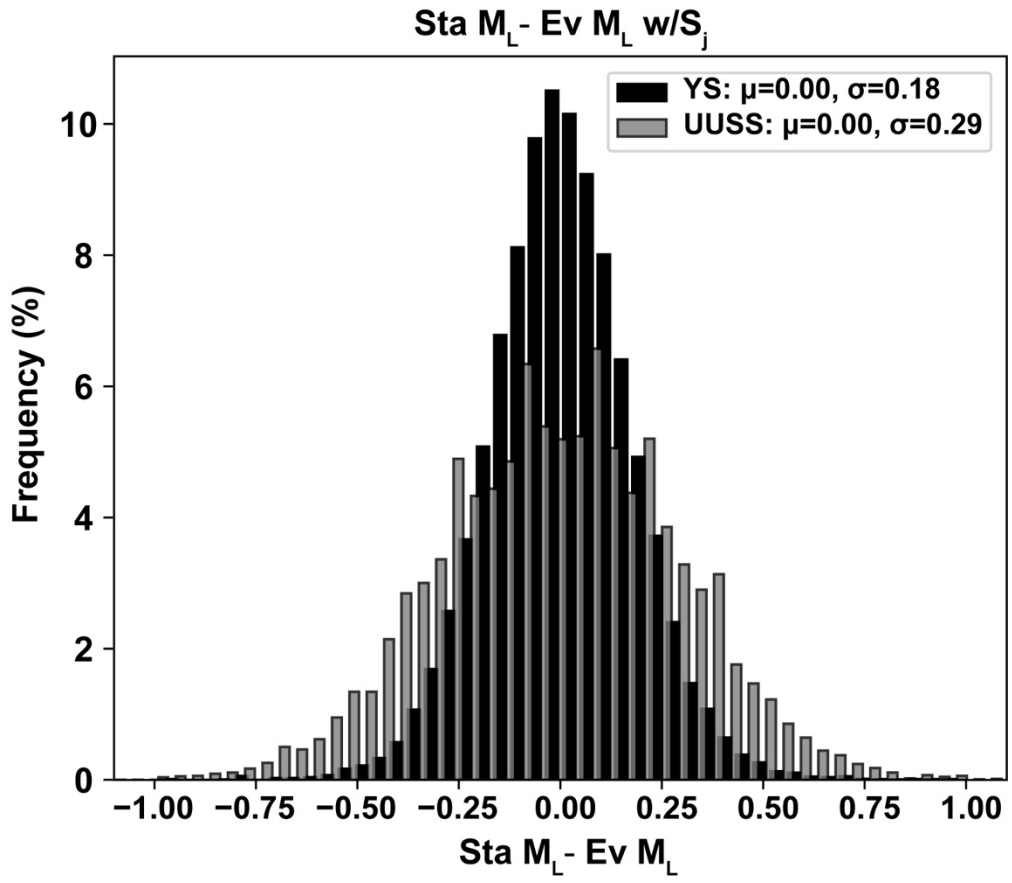

Figure B4 – Distribution of station – event magnitude residuals (using station corrections) for YS M_L (black bars – Figure 3.13d) and UUSS M_L (grey bars - Figure 3.13b).

Appendix C

Tables

Table C1 - Complied station meta data for all 34 KiK-Net stations included in this study

Station	Vs30 (m/s)	κ_0	κ_{rock}	κ_b	Total ΔM_L	Total Record Pairs for S/B	Total Record Pairs used for H/V
AKTH02	620	0.0379	0.0291	0.0088	832	303	353
AKTH03	320	0.055	0.039	0.016	636	276	332
AKTH16	375	0.0313	0.0179	0.0135	957	353	412
AKTH17	289	0.0394	0.0272	0.0122	937	296	351
FKOH10	921	0.0294	0.0111	0.0182	438	413	417
FKSH08	562	0.0374	0.0206	0.0168	1250	353	422
FKSH09	585	0.037	0.0157	0.0213	2145	605	728
FKSH10	487	0.0399	0.0156	0.0242	2343	691	816
FKSH11	240	0.043	0.0311	0.012	1694	500	584
FKSH21	365	0.0261	0.0092	0.0169	750	568	592
IWTH04	456	0.0217	0.0122	0.0095	1872	345	425
IWTH05	429	0.0153	0.0062	0.0091	1645	340	408
IWTH15	338	0.0434	0.0231	0.0203	1825	344	442
IWTH22	532	0.0269	0.0138	0.0131	1547	326	396
IWTH24	486	0.0371	0.0256	0.0115	1887	424	518
KMMH02	577	0.0276	0.0021	0.0255	514	501	505
KMMH10	463	0.0479	0.0277	0.0202	267	258	258
KMMH12	410	0.056	0.0435	0.0125	514	483	490
MYGH04	850	0.0356	0.0269	0.0088	2008	430	511
MYGH06	593	0.0383	0.0238	0.0145	2074	581	670
MYGH11	859	0.0329	0.0157	0.0172	1220	283	315
MYZH04	484	0.0382	0.0229	0.0153	385	303	312
NGNH29	465	0.0537	0.0342	0.0195	397	362	371
NIGH06	336	0.054	0.0374	0.0167	613	506	524

NIGH10	653	0.0272	0.0127	0.0146	705	504	543
NIGH13	461	0.0772	0.0652	0.012	342	346	345
SITH11	372	0.0484	0.0274	0.021	811	191	235
TCGH07	419	0.0318	0.0219	0.0098	738	412	426
TCGH09	468	0.0454	0.0249	0.0205	1569	482	555
TCGH10	371	0.0438	0.0257	0.0181	2414	727	857
TCGH11	329	0.0306	0.0136	0.017	1003	274	298
TCGH12	344	0.0421	0.0242	0.0178	2391	767	867
TCGH14	849	0.0413	0.0311	0.0102	1340	339	383
TCGH15	423	0.0436	0.025	0.0186	482	88	93

Figures

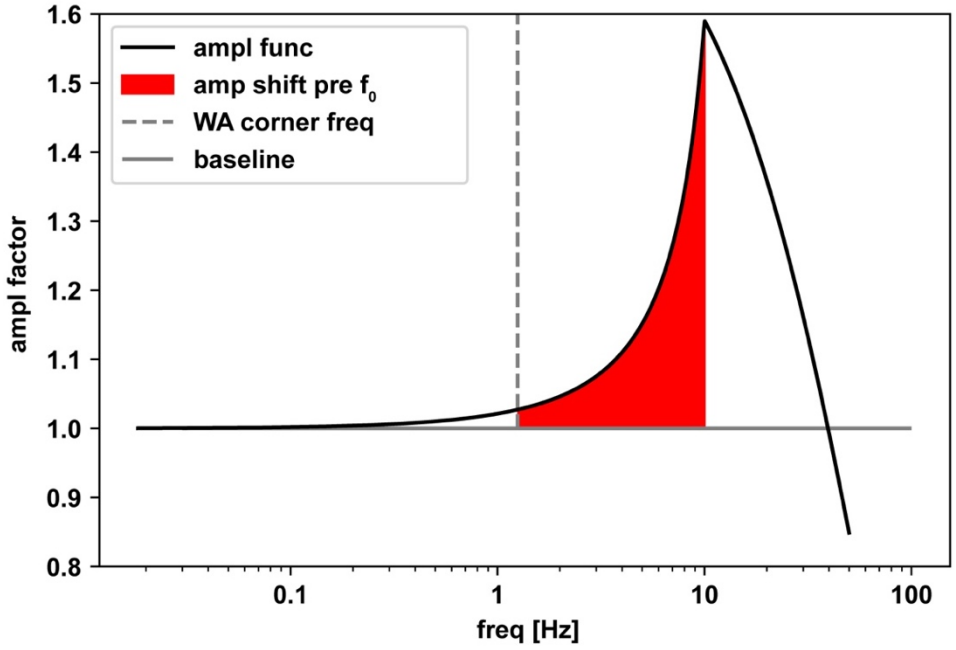

Figure C1 - Hard rock quarter wavelength amplification function (QWL) with fundamental frequency (f_0) of 10 Hz (solid black line). The shaded region is the amplification of the QWL function leading up to f_0. The QWL shown has a κ_0 filter of 0.005 s applied. The approximate WA corner frequency is marked by the grey dashed line.

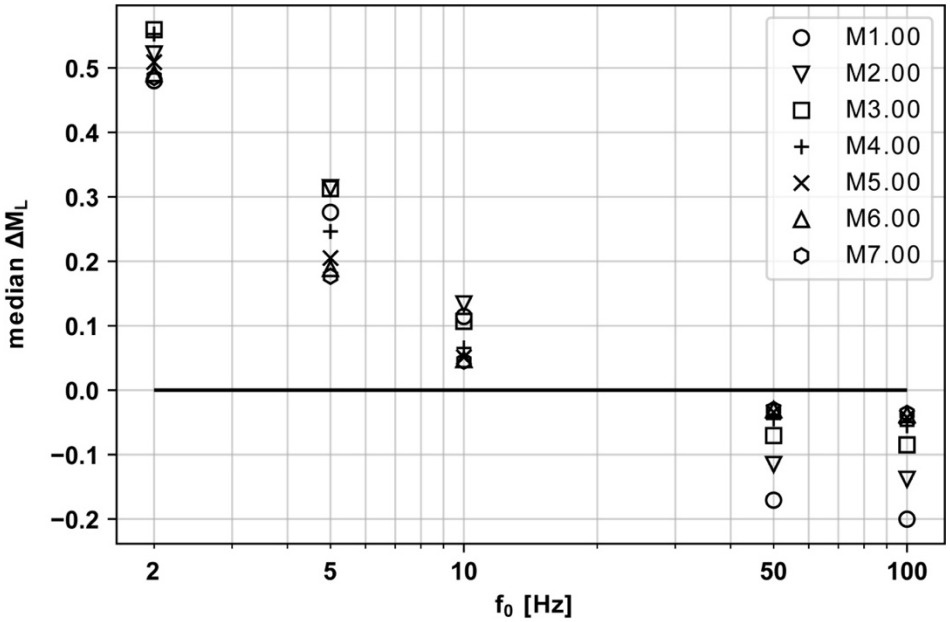

Figure C2 - Median ΔM_L (over all distances) vs site fundamental frequency of simulation for earthquakes with **M** 1-7, with $\Delta\sigma$ = 10 Bar/1 MPa, and κ_0 = 0.005 s.

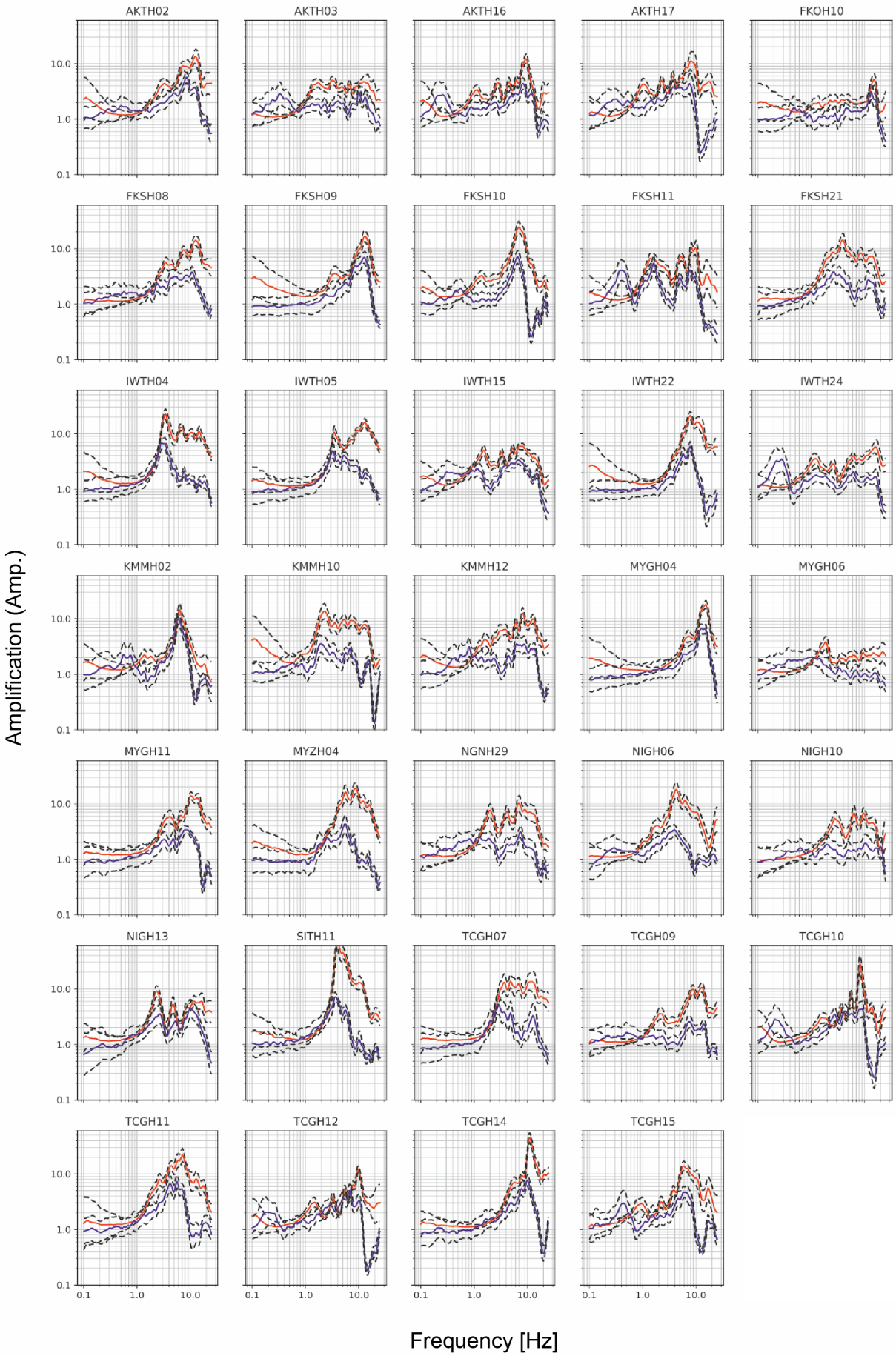

Figure C3 - Comparison of the S/B (solid red) to the H/V (solid blue) for all 34 KiK-Net stations included in this study. The black dashed lines represent one standard deviation (log statistics) of each respective amplification functions. The number of record pairs used to calculate each amplification function for each station can be found in Table C1.

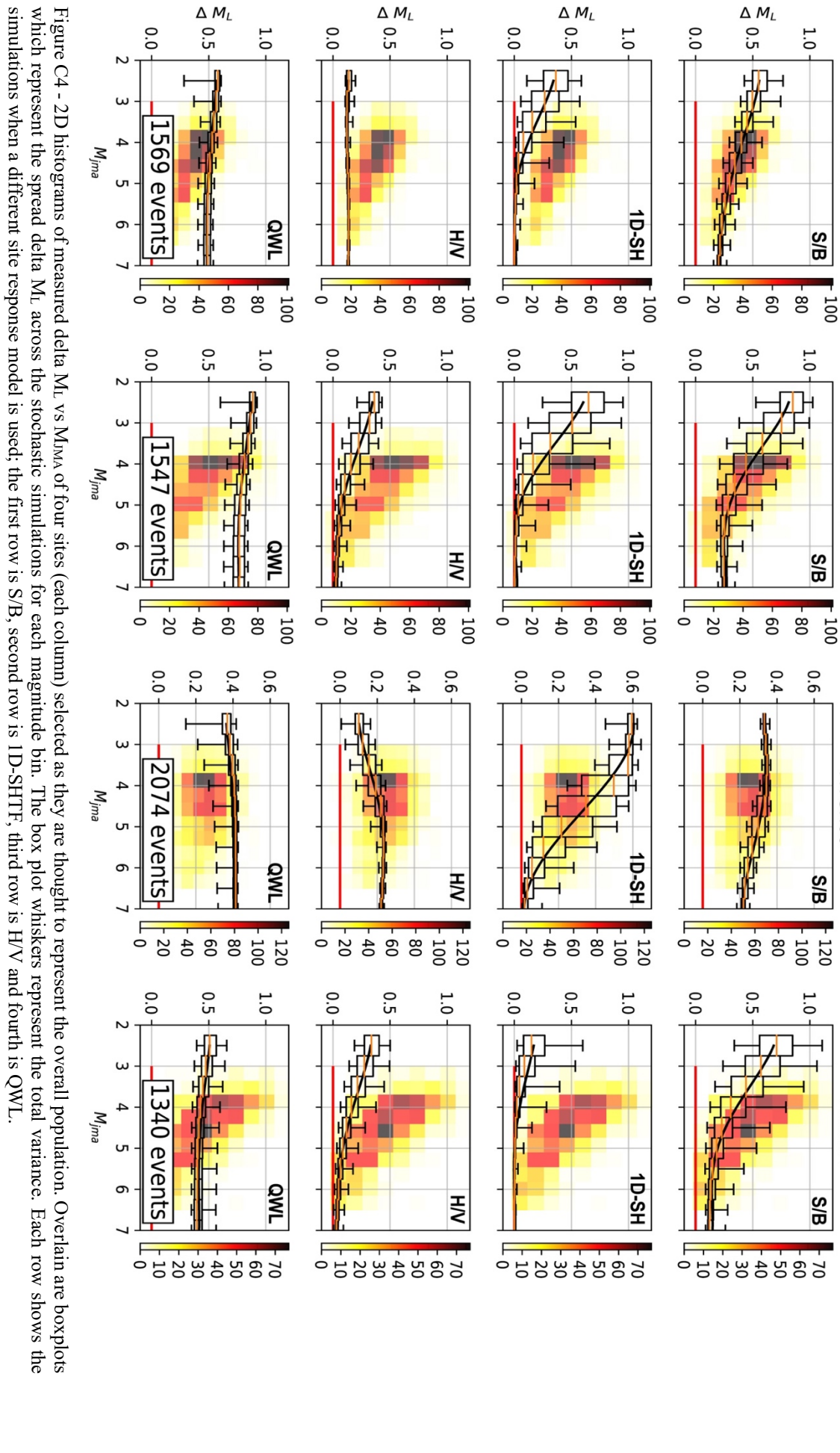

Figure C4 - 2D histograms of measured delta M_L vs M_{JMA} of four sites (each column) selected as they are thought to represent the overall population. Overlain are boxplots which represent the spread delta M_L across the stochastic simulations for each magnitude bin. The box plot whiskers represent the total variance. Each row shows the simulations when a different site response model is used; the first row is S/B, second row is 1D-SHTF, third row is H/V and fourth is QWL.

References

Aki, K. (1967), Scaling law of seismic spectrum, J. Geophys. Res., 72, 1217–1231, doi:10.1029/JZ072i004p01217.

Alsaker, A., L. B. Kvamme, R. A. Hansen, A. Dahle, and H. Bungum (1991). The ML scale in Norway, Bull. Seism. Soc. Am .81, 379–398.

Anderson, J. G., and Hough, S. E. (1984). A model for the shape of the Fourier amplitude spectrum of acceleration at high frequencies. *Bulletin of the Seismological Society of America*, *74*(5), 1969–1993.

Anderson, J. A., and Wood, H. O. (1925). Description and theory of the torsion seismometer. *Bulletin of the Seismological Society of America*, *15*(1), 1-72.

Aoi, S., Kunugi, T., and Fujiwara, H. (2004). Strong-motion seismograph network operated by NIED: K-NET and KiK-net. *Journal of Japan Association for Earthquake Engineering*, *4*(3), 65–74.

Arabasz, W. J., Pechmann, J. C., and Burlacu, R. (2016). A uniform moment magnitude earthquake catalogue and background seismicity rates for the Wasatch Front and surrounding Utah region. Appendix E of Earthquake Probabilities for the Wasatch Front region in Utah, Idaho, and Wyoming: Utah Geological Survey Miscellaneous Publication 16, 3.

Atkinson, G. M. (2004). Empirical attenuation of ground-motion spectral amplitudes in southeastern Canada and the northeastern United States. Bulletin of the Seismological Society of America, 94(3), 1079-1095.

Atkinson, G. M., and McCartney, S. E. (2005). A revised magnitude-recurrence relation for shallow crustal earthquakes in southwestern British Columbia: Considering the relationships between moment magnitude and regional magnitudes. *Bulletin of the Seismological Society of America, 95*(1), 334-340.

Atkinson, G. M. (2012). Evaluation of attenuation models for the northeastern United States/southeastern Canada. Seismological Research Letters, 83(1), 166-178.

Atkinson, G. M., and Boore, D. M. (2013). The attenuation of Fourier amplitudes for rock sites in eastern North America. Bulletin of the Seismological Society of America, 104(1), 513-528.

Atkinson, G. M., and Mereu, R. F. (1992). The shape of ground motion attenuation curves in southeastern Canada. Bulletin of the Seismological Society of America, 82(5), 2014-2031.

Baker, J. W. (2008). An introduction to probabilistic seismic hazard analysis (PSHA). *White paper, version*, *1*, 72.

Bakun, W. H., and W. B. Joyner (1984). The ML scale in central California, Bull. Seism. Soc. Am .74, 1827–1843.

Beauval, C., and Scotti, O. (2004). Quantifying sensitivities of PSHA for France to earthquake catalogue uncertainties, truncation of ground-motion variability, 512 and magnitude limits. Bulletin of the Seismological Society of America, 94(5), 1579–1594.

Benz, H. M., Frankel, A., and Boore, D. M. (1997). Regional Lg attenuation for the continental United States. *Bulletin of the Seismological Society of America*, *87*(3), 606-619.

Bindi, D., Spallarossa, D., Eva, C., and Cattaneo, M. (2005). Local and duration magnitudes in northwestern Italy, and seismic moment versus magnitude relationships. *Bulletin of the Seismological Society of America*, *95*(2), 592-604.

Bindi, D., Picozzi, M., Spallarossa, D., Cotton, F., and Kotha, S. R. (2019). Impact of Magnitude Selection on Aleatory Variability Associated with Ground‐Motion Prediction Equations: Part II—Analysis of the Between‐Event Distribution in Central Italy. Bulletin of the Seismological Society of America, 109(1), 251-262.

Bindi, D., Zaccarelli, R., Strollo, A., and Di Giacomo, D. (2019). Harmonized local magnitude attenuation function for Europe using the European Integrated Data Archive (EIDA). Geophysical Journal International, 218(1), 519-533.

Boatwright, J. (1978). Detailed spectral analysis of two small New York State earthquakes. *Bulletin of the Seismological Society of America*, *68*(4), 1117-1131.

Boggs, P. T., Donaldson, J. R., and Schnabel, R. B. (1989). Algorithm 676: ODRPACK: software for weighted orthogonal distance regression. ACM Transactions on Mathematical Software (TOMS), 15(4), 348-364.

Bommer, J., J., and Crowley, H. (2017). The Purpose and Definition of the Minimum Magnitude Limit in PSHA Calculations. *Seismological Research Letters*, *88*(4), 1097–1106.

Bommer, J., J., Oates, S., Cepeda, J.M., Lindholm, C., Bird, J., Torres, R., Marroquin, G. and Rivas, J. (2006). Control of hazard due to seismicity induced by a hot fractured rock geothermal project. *Engineering Geology*, *83*(4), 287–306.

Bommer, J.J., Stafford, P.J., Edwards, B., Dost, B., van Dedem, E., Rodriguez-Marek, A., Kruiver, P., van Elk, J., Doornhof, D. and Ntinalexis, M. (2017). Framework for a ground-motion model for induced seismic hazard and risk analysis in the Groningen gas field, the Netherlands. *Earthquake Spectra, 33*(2), 481-498.

Boore, D. M. (1983). Stochastic simulation of high-frequency ground motions based on seismological models of the radiated spectra. *Bulletin of the Seismological Society of America*, *73*(6A), 1865–1894.

Boore, D. M. (1989). The Richter scale: its development and use for determining earthquake source parameters. *Tectonophysics*, *166*(1-3), 1-14.

Boore, D. M. (2003). Simulation of ground motion using the stochastic method. *Pure and Applied Geophysics*, *160*(3-4), 635–676.

Boore, D. M. (2013). The uses and limitations of the square-root-impedance method for computing site amplification. *Bulletin of the Seismological Society of America*, *103*(4), 2356–2368.

Boore, D. M., and Joyner, W. B. (1997). Site amplifications for generic rock sites. *Bulletin of the Seismological Society of America*, *87*(2), 327–341.

Bormann, P., and Dewey, J. W. (2012). The new IASPEI standards for determining magnitudes from digital data and their relation to classical magnitudes.

Bowden, D. C., Tsai, V. C., and Lin, F. C. (2017). Amplification and attenuation across USArray using ambient noise wavefront tracking. Journal of Geophysical Research: Solid Earth, 122(12), 10-086.

Brazier, R. A., Miao, Q., Nyblade, A. A., Ayele, A., and Langston, C. A. (2008). Local magnitude scale for the Ethiopian Plateau. Bulletin of the Seismological Society of America, 98(5), 2341-2348.

Brockman, S. R., and Bollinger, G. A. (1992). Q estimates along the Wasatch Front in Utah derived from Sg and Lg wave amplitudes. Bulletin of the Seismological Society of America, 82(1), 135-147.

Brune, J. N. (1970). Tectonic stress and the spectra of seismic shear waves from earthquakes. Journal of Geophysical Research, 75(26), 4997–5009. https://doi.org/10.1029/JB075i026p04997

Brune, J. N. (1971). CORRECTION. Journal of Geophysical Research, 76(20), 5002–and.

Catchings, R. D., and Kohler, W. M. (1996). Reflected seismic waves and their effect on strong shaking during the 1989 Loma Prieta, California, earthquake. Bulletin of the Seismological Society of America, 86(5), 1401-1416.

Cassidy, J. F., Rogers, G. C., and Ristau, J. (2005). Seismicity in the vicinity of the SNORCLE corridors of the northern Canadian Cordillera. *Canadian Journal of Earth Sciences*, *42*(6), 1137-1148.

Castello, B., Olivieri, M., and Selvaggi, G. (2007). Local and duration magnitude determination for the Italian earthquake catalogue, 1981–2002. *Bulletin of the Seismological Society of America*, *97*(1B), 128–139.

Chapman, M. C., and Godbee, R. W. (2012). Modeling geometrical spreading and the relative amplitudes of vertical and horizontal high-frequency ground motions in eastern North America. Bulletin of the Seismological Society of America, 102(5), 1957-1975.

Chatterjee, S. N., Pitt, A. M., and Iyer, H. M. (1985). Vp/Vs ratios in the Yellowstone national park region, Wyoming. Journal of Volcanology and Geothermal Research, 26(3-4), 213-230.

Christiansen, R. L., Lowenstern, J. B., Smith, R. B., Heasler, H., Morgan, L. A., Nathenson, M., ... and Robinson, J. E. (2007). Preliminary assessment of volcanic and hydrothermal hazards in Yellowstone National Park and vicinity. *U. S. Geological Survey*.

Clawson, S. R., Smith, R. B., and Benz, H. M. (1989). P wave attenuation of the Yellowstone caldera from three-dimensional inversion of spectral decay using explosion source seismic data. Journal of Geophysical Research: Solid Earth, 94(B6), 7205-7222.

Dahm, T., and Kruger, F. (2014). Moment tensor inversion and moment tensor interpretation. *New Manual of Seismological Observatory Practice*, *2*, 1-37.

Di Bona, M. (2016). A local magnitude scale for crustal earthquakes in Italy. Bulletin of the Seismological Society of America, 106(1), 242-258.

Deichmann, N. (2006). Local magnitude, a moment revisited. Bulletin of the Seismological Society of America, 96(4A), 1267-1277.

Deichmann, N. (2017). Theoretical basis for the observed break in ML/Mw scaling between small and large earthquakes. Bulletin of the Seismological Society of America, 107(2), 505–520.

Deichmann, N. (2018). The relation between M E, M L and M w in theory and numerical simulations for small to moderate earthquakes. Journal of Seismology, 22(6), 1645-1668.

Dewberry, S. R., and Crosson, R. S. (1995). Source scaling and moment estimation for the Pacific Northwest seismograph network using S-coda amplitudes. *Bulletin of the Seismological Society of America*, *85*(5), 1309-1326.

Dost, B., Edwards, B., and Bommer, J. J. (2018). The relationship between **M** and ML: A review and application to induced seismicity in the Groningen gas field, the Netherlands. Seismological Research Letters, 89(3), 1062-1074.

Douglas, J., and Edwards, B. (2016). Recent and future developments in earthquake ground motion estimation. *Earth-Science Reviews*, *160*, 203-219.

Edwards, B., Rietbrock, A., Bommer, J. J., and Baptie, B. (2008). The acquisition of source, path, and site effects from microearthquake recordings using Q tomography: Application to the United Kingdom. *Bulletin of the Seismological Society of America*, *98*(4), 1915-1935.

Edwards, B., and Rietbrock, A. (2009). A comparative study on attenuation and source-scaling relations in the Kantō, Tokai, and Chubu regions of Japan, using data from Hi-Net and KiK-Net. Bulletin of the Seismological Society of America, 99(4), 2435-2460.

Edwards, B., Allmann, B., Fäh, D., and Clinton, J. (2010). Automatic computation of moment magnitudes for small earthquakes and the scaling of local to moment magnitude. Geophysical Journal International, 183(1), 407-420.

Edwards, B., Fäh, D., and Giardini, D. (2011). Attenuation of seismic shear wave energy in Switzerland. Geophysical Journal International, 185(2), 967-984.

Edwards, B., Kraft, T., Cauzzi, C., Kästli, P., and Wiemer, S. (2015). Seismic monitoring and analysis of deep geothermal projects in St Gallen and Basel, Switzerland. Geophysical Journal International, 201(2), 1022-1039.

Edwards, B., Ktenidou, O. J., Cotton, F., Abrahamson, N., Van Houtte, C., & Fäh, D. (2015). Epistemic uncertainty and limitations of the κ 0 model for near-surface attenuation at hard rock sites. *Geophysical Journal International*, *202*(3), 1627-1645.

Efron, B. (1987). Better bootstrap confidence intervals (with discussions). Jour. Amer. Stat. Assoc. 82, 171-200.

Eyre, T. S., and van der Baan, M. (2015). Overview of moment-tensor inversion of microseismic events. *The Leading Edge*, *34*(8), 882-888.

Farrell, J., Husen, S., and Smith, R. B. (2009). Earthquake swarm and b-value characterization of the Yellowstone volcano-tectonic system. Journal of Volcanology and Geothermal Research, 188(1-3), 260-276.

Farrell, J., Smith, R. B., Husen, S., and Diehl, T. (2014). Tomography from 26 years of seismicity revealing that the spatial extent of the Yellowstone crustal magma reservoir extends well beyond the Yellowstone caldera. Geophysical Research Letters, 41(9), 3068-3073.

Frankel, A., A. McGarr, J. Bicknell, J. Mori, L. Seeber, and E. Cranswick (1990). Attenuation of high-frequency shear waves in the crust: Measurements from New York State, South Africa, and southern California, J. Geophys. Res .95, 17,441–17,457.

Giardini, D., Gruenthal, G., Shedlock, K., and Zhang, P. (2003). The GSHAP global seismic hazard map. In International Handbook of Earthquake & Engineering Seismology (Chapter 71, Vol. 81B, pp. 1233-1239). Academic Press.

Gilbert F. , 1970. Excitation of the normal modes of the earth by earthquake sources, *Geophys. J. R. astr. Soc. , 22*, 223–226.

Goertz-Allmann, B. P., Edwards, B., Bethmann, F., Deichmann, N., Clinton, J., Fäh, D., and Giardini, D. (2011). A new empirical magnitude scaling relation for Switzerland. *Bulletin of the Seismological Society of America*, *101*(6), 3088–3095.

Griscom, M., and W. J. Arabasz (1979). Local magnitude (ML) in the Wasatch Front and Utah region: Wood–Anderson calibration, coda- duration estimates of ML, and ML versus Mb, in Earthquake Studies in Utah, 1850 to 1978 , W. J. Arabasz, R. B. Smith, and W. D. Richins (Editors), Special Publication, University of Utah Seismograph Stations, Salt Lake City, Utah, 433–443.

Grünthal G. Wahlstrom R., and Stromeyer D. 2009. The unified catalogue of earthquakes in central, northern, and northwestern Europe (CENEC)-updated and expanded to the last millennium, *J. Seismol*. 13, 517–541.

Gutenberg, B., and Richter, C. F. (1954). Seismicity of the earth and related phenomena. Princeton (NJ).

Hanks, T. C. (1979). b values and ω− γ seismic source models: Implications for tectonic stress variations along active crustal fault zones and the estimation of high-frequency strong ground motion. *Journal of Geophysical Research: Solid Earth, 84*(B5), 2235-2242.

Hanks, T. C., and Boore, D. M. (1984). Moment-magnitude relations in theory and practice. Journal of Geophysical Research: Solid Earth, 89(B7), 6229–6235.

Havskov, J., and Ottemöller, L. *Routine Data Processing in Earthquake Seismology*. Springer, Dordrecht, 2010.

Herrmann R. B. Benz H. Ammon C. J. (2011). Monitoring the earthquake source process in North America, *Bulletin of the Seismological Society of America,* 101, 2609–2625.

Holmgren, J. M., and Atkinson, G. M. (2018). Effect of uncertainty in source parameters on ground-motion variability for potentially induced earthquakes in the Central United States. *Seismological Research Letters*, *89*(2A), 702-711.

Holt, M. M., Koper, K. D., Yeck, W., D'Amico, S., Li, Z., Hale, J. M., and Burlacu, R. (2019). On the Portability of ML–M c as a Depth Discriminant for Small

Seismic Events Recorded at Local Distances. Bulletin of the Seismological Society of America. https://doi.org/10.1785/0120190096

Huang, H. H., Lin, F. C., Schmandt, B., Farrell, J., Smith, R. B., & Tsai, V. C. (2015). The Yellowstone magmatic system from the mantle plume to the upper crust. Science, 348(6236), 773-776.

Hutton, L. K., and D. M. Boore (1987). The ML scale in southern California, Bull. Seism. Soc. Am .77, 2074–2094.

Illsley-Kemp, F., Keir, D., Bull, J. M., Ayele, A., Hammond, J. O., Kendall, J.-M., et al. (2017). Local earthquake magnitude scale and b-value for the Danakil region of northern Afar. *Bulletin of the Seismological Society of America*, *107*(2), 521–531.

Jeon, Y. S., and Herrmann, R. B. (2004). High-frequency earthquake ground-motion scaling in Utah and Yellowstone. Bulletin of the Seismological Society of America, 94(5), 1644-1657.

Johnson, T., and Molnar, P. (1972). Focal mechanisms and plate tectonics of the southwest Pacific. *Journal of Geophysical Research*, *77*(26), 5000-5032.

Jost, M. U., and Herrmann, R. B. (1989). A student's guide to and review of moment tensors. *Seismological Research Letters*, *60*(2), 37-57.

Kanamori, H. (1977). The energy release in great earthquakes. Journal of Geophysical Research, 82(20), 2981–2987.

Kanamori, H. (1983). Magnitude scale and quantification of earthquakes. *Tectonophysics*, *93*(3-4), 185-199.

Kanamori, H., and Jennings, P. C. (1978). Determination of local magnitude, ML, from strong-motion accelerograms. *Bulletin of the Seismological Society of America*, *68*(2), 471–485.

Keir, D., Stuart, G. W., Jackson, A., and Ayele, A. (2006). Local earthquake magnitude scale and seismicity rate for the Ethiopian rift. *Bulletin of the Seismological Society of America*, *96*(6), 2221-2230.

Kishida, T., Derakhshan, S., Muin, S., Darragh, R. B., Bozorgnia, Y., Kuehn, N., and Kwak, D. Y. (2018). Multivariate Conversion of Moment Magnitude for Small-to-Moderate-Magnitude Earthquakes in Iran. Earthquake Spectra, 34(1), 313-326.

Knopoff, L. (1964a). A matrix method for elastic wave problems. *Bulletin of the Seismological Society of America*, *54*(1), 431–438.

Knopoff, L. (1964b). Q. *Rev Geophys*, *2*(4), 625–660.

Koper, K. D., Pechmann, J. C., Burlacu, R., Pankow, K. L., Stein, J., Hale, J. M., ... and McCarter, M. K. (2016). Magnitude-based discrimination of man-made seismic events from naturally occurring earthquakes in Utah, USA. Geophysical Research Letters, 43(20), 10-638.

Konno, K., and Ohmachi, T. (1998). Ground-motion characteristics estimated from spectral ratio between horizontal and vertical components of microtremor. *Bulletin of the Seismological Society of America*, *88*(1), 228–241.

Kramer, S. L. (1996). Geotechnical earthquake engineering. in prentice–Hall international series in civil engineering and engineering mechanics.

Krischer, L., Megies, T., Barsch, R., Beyreuther, M., Lecocq, T., Caudron, C., and Wassermann, J. (2015). ObsPy: A bridge for seismology into the scientific Python ecosystem. Computational Science and Discovery, 8(1), 014003.

Křížová, D., Zahradník, J., and Kiratzi, A. (2013). Resolvability of isotropic component in regional seismic moment tensor inversion. Bulletin of the Seismological Society of America, 103(4), 2460-2473.

Langston, C. A., R. Brazier, A. A. Nyblade, and T. J. Owens (1998). Local magnitude scale and seismicity rate for Tanzania, east Africa, Bull. Seism. Soc. Am .88, 712–721.

Lawrence, J. F., and Prieto, G. A. (2011). Attenuation tomography of the western United States from ambient seismic noise. Journal of Geophysical Research: Solid Earth, 116(B6).

Lees J., M. and Park J., 1995. Multiple-taper spectral analysis: a stand-alone C subroutine, Comput. Geosci. , 21, 199–236.

Lolli, B., Gasperini, P., Mele, F. M., and Vannucci, G. (2015). Recalibration of the distance correction term for local magnitude (ML) computations in Italy. *Seismological Research Letters*, *86*(5), 1383-1392.

Luckett, R., Ottemöller, L., Butcher, A., and Baptie, B. (2018). Extending local magnitude ML to short distances. *Geophysical Journal International*, *216*(2), 1145-1156.

Madriaga, R., Dynamics of an expanding circular fault, *Bulletin of the Seismological Society of America*, 66, 639-666, 1976.

McNamara, D. E. (2000). Frequency dependent Lg attenuation in south-central Alaska. Geophysical research letters, 27(23), 3949-3952.

Miao, Q., and Langston, C. A. (2007). Empirical distance attenuation and the local-magnitude scale for the central United States. *Bulletin of the Seismological Society of America*, *97*(6), 2137–2151.

Michel C., Edwards B., Poggi, V., Burjánek J., Roten D., Cauzzi C. and Fäh D., 2014. Assessment of site effects in Alpine regions through systematic site characterization of seismic stations. *Bulletin of the Seismological Society of America*, *(104)*6, 2809-2826

Mignan, A., Broccardo, M., Wiemer, S., and Giardini, D. (2017). Induced seismicity closed-form traffic light system for actuarial decision-making during deep fluid injections. *Scientific Reports*, *7*(1), 13607.

Minson, S. E., and Dreger, D. S. (2008). Stable inversions for complete moment tensors. Geophysical Journal International, 174(2), 585-592.

Munafò, I., Malagnini, L., and Chiaraluce, L. (2016). On the relationship between Mw and ML for small earthquakes. Bulletin of the Seismological Society of America, 106(5), 2402-2408.

Malagnini, L., and R. B. Herrmann (2000). Ground motion scaling in the region of the 1997 Umbria-Marche earthquake (Italy), Bulletin of the Seismological Society of America. 90, 1041-1051.

Malagnini, L., and Munafò, I. (2018). On the Relationship between ML and M w in a Broad Range: An Example from the Apennines, Italy. Bulletin of the Seismological Society of America, 108(2), 1018-1024.

Mayeda, K., and W. R. Walter (1996). Moment, energy, stress drop, and source spectra of western United States earthquakes from regional coda envelopes, *J. Geophys. Res. 101*, 11,195-11,208.

Nakamura, Y. (1989). A method for dynamic characteristics estimation of subsurface using microtremor on the ground surface. *QR Railway Tech. Res. Inst.*, *30*(1), 25–33.

Oth, A., Bindi, D., Parolai, S., and Di Giacomo, D. (2010). Earthquake scaling characteristics and the scale-(in) dependence of seismic energy-to-moment ratio: Insights from KiK-net data in Japan. *Geophysical Research Letters*, *37*(19).

Ottemöller, L., and Havskov, J. (2003). Moment magnitude determination for local and regional earthquakes based on source spectra. *Bulletin of the Seismological Society of America*, *93*(1), 203-214.

Pasyanos, M. E., Matzel, E. M., Walter, W. R., and Rodgers, A. J. (2009). Broad-band Lg attenuation modelling in the Middle East. *Geophysical Journal International*, *177*(3), 1166-1176.

Pechmann, J. C., Bernier, S. J. Nava, and F. M. Terra (2006), Correction of systematic time-dependent coda magnitude errors in the Utah and Yellowstone National Park region earthquake catalogs, 1981–2001, Appendix C, in *Integrated Regional and Urban Seismic Monitoring—Wasatch Front Area, Utah and Adjacent Intermountain Seismic Belt*, edited by W. J. Arabasz et al., Final Tech. Rep., 137 pp., U.S. Geological Survey Cooperative Agreement 04HQAG0014. [Available at http://earthquake.usgs.gov/research/external/reports/0

Pechmann, J. C., Nava, S. J., Terra, F. M., and Bernier, J. C. (2007). Local magnitude determinations for intermountain seismic belt earthquakes from broadband digital data. Bulletin of the Seismological Society of America, 97(2), 557-574.

Pechmann, J. C., and Whidden, K.M., 2013, The relation of University of Utah local and coda magnitudes to moment magnitudes: The sequel [abs.]: Seismological Research Letters, v. 84, no. 2, p. 299.

Poggi, V., Burjánek, J., Michel, C., and Fäh, D. (2017). Seismic site-response characterization of high-velocity sites using advanced geophysical techniques: application to the NAGRA-Net. *Geophysical Journal International. Volume 210, Issue 2*, 645-659.

Poggi, V., Edwards, B., and Fäh, D. (2012). The quarter-wavelength average velocity: a review of some past and recent application developments. *Proceedings of the 15th World Conference on Earthquake Engineering* (No. 4242).

Poggi, V., Edwards, B., and Fäh, D. (2013). Reference S-wave velocity profile and attenuation models for ground-motion prediction equations: Application to Japan. *Bulletin of the Seismological Society of America*, *103*(5), 2645–2656.

Régnier, J., Bonilla, L.-F., Bard, P.-Y., Bertrand, E., Hollender, F., Kawase, H., Sicilia, D., Arduino, P., Amorosi, A., Asimaki, D., et al. (2018). PRENOLIN:

International Benchmark on 1D Nonlinear Site-Response Analysis—Validation Phase Exercise. *Bulletin of the Seismological Society of America*.

Reiter, L. (1991). *Earthquake hazard analysis: issues and insights*. Columbia University Press.

Rhoades, D. A. (1997). Estimation of attenuation relations for strong-motion data allowing for individual earthquake magnitude uncertainties. *Bulletin of the Seismological Society of America*, *87*(6), 1674-1678.

Richter, C. F. (1935). An instrumental earthquake magnitude scale. *Bulletin of the Seismological Society of America*, *25*(1), 1-32.

Richter, C. F. (1958). Elementary Seismology , W. H. Freeman and Co., San Francisco, California, 768 pp.

Rietbrock, A. (2001). P wave attenuation structure in the fault area of the 1995 Kobe earthquake. *Journal of Geophysical Research: Solid Earth*, *106*(B3), 4141-4154.

Ristau, J., Harte, D., and Salichon, J. (2016). A revised local magnitude (ML) scale for New Zealand earthquakes. *Bulletin of the Seismological Society of America*, *106*(2), 398–407.

Ristau, J., Rogers, G. C., and Cassidy, J. F. (2003). Moment magnitude–local magnitude calibration for earthquakes off Canada's west coast. *Bulletin of the Seismological Society of America*, 93(5), 2296-2300.

Rodriguez, V. H., and Midorikawa, S. (2003). Comparison of spectral ratio techniques for estimation of site effects using microtremor data and earthquake motions recorded at the surface and in boreholes. *Earthquake Engineering and Structural Dynamics*, *32*(11), 1691–1714.

Savage, M. K., and Anderson, J., G. (1995). A local-magnitude scale for the western Great Basin—eastern Sierra Nevada from synthetic Wood– Anderson seismograms, Bull. Seism. Soc. Am .85, 1236–1243.

Sardinal, V., and Midorikawa, S. (2004). Site Classification Based on Spectral Amplification Patterns for Microtremor H/V Ratios. In *13th World Conference on Earthquake Engineering Vancouver*.

Shemata, J.E. (1989). New analysis of three-component digital data for aftershocks of the 1983 Borah Peak earthquake, central Idaho—Source parameters and refined hypocenters: Salt Lake City, University of Utah, unpublished M.S. thesis, 126 p.

Smith, R. B., Arabasz, W. J., Slemmons, D. B., Engdahl, E. R., Zoback, M. D., and Blackwell, D. D. (1991). Seismicity of the intermountain seismic belt. Neotectonics of North America, 1, 185-228.

Stafford, P. J., Rodriguez-Marek, A., Edwards, B., Kruiver, P. P., and Bommer, J. J. (2017). Scenario Dependence of Linear Site-Effect Factors for Short-Period Response Spectral Ordinates. *Bulletin of the Seismological Society of America*, *107*(6), 2859–2872.

Staudenmaier, N., Tormann, T., Edwards, B., Deichmann, N., and Wiemer, S. (2018). Bilinearity in the Gutenberg-Richter Relation Based on ML for Magnitudes

Above and Below 2, From Systematic Magnitude Assessments in Parkfield (California). *Geophysical Research Letters*, *45*(14), 6887-6897.

Stein, S., and Wysession, M. (2003). An introduction to seismology. *Earthquakes, and Earth*.

Thompson, E. M., Baise, L. G., Tanaka, Y., and Kayen, R. E. (2012). A taxonomy of site response complexity. *Soil Dynamics and Earthquake Engineering*, *41*, 32–43.

Trifunac, M., and Todorovska, M. (1996). Nonlinear soil response—1994 Northridge, California, earthquake. *Journal of Geotechnical Engineering*, *122*(9), 725–735.

Udías, A., Vallina, A. U., Madariaga, R., and Buforn, E. (2014). Source mechanisms of earthquakes: Theory and practice. *Cambridge University Press*.

Uhrhammer, R. A., and E. R. Collins (1990). Synthesis of Wood–Anderson seismograms from broadband digital records, Bull. Seism. Soc. Am . 80, 702–716.

Uhrhammer, R. A., Hellweg, M., Hutton, K., Lombard, P., Walters, A. W., Hauksson, E., and Oppenheimer, D. (2011). California Integrated Seismic Network (CISN) local magnitude determination in California and vicinity. *Bulletin of the Seismological Society of America*, *101*(6), 2685-2693.

Utsu, T. (2003)a. Statistical Features of Seismology. In International Handbook of Earthquake and Engineering Seismology (Chapter 43, Vol. 81A, pp. 719-732). Academic Press.

Wesley Greig, D., Yenier, E., Baturan, D., and Karimi, S. (2018). Determination of local magnitude distance corrections for northern Oklahoma. Seismological Research Letters, 89(5), 1786-1795.

Whidden, K. M., and Pankow, K. L. (2012). A catalogue of regional moment tensors in Utah from 1998 to 2011. Seismological Research Letters, 83(5), 775-783.

Woessner, J., and Wiemer, S. (2005). Assessing the quality of earthquake catalogues: Estimating the magnitude of completeness and its uncertainty. Bulletin of the Seismological Society of America, 95(2), 684-698.

Working Group on Utah Earthquake Probabilities (WGUEP), 2016, Earthquake probabilities for the Wasatch Front region in Utah, Idaho, and Wyoming: Utah Geological Survey Miscellaneous Publication 16-3, 164 p., 5 appendices.

Wu, S. M., Ward, K. M., Farrell, J., Lin, F. C., Karplus, M., and Smith, R. B. (2017). Anatomy of Old Faithful from subsurface seismic imaging of the Yellowstone Upper Geyser Basin. Geophysical Research Letters, 44(20), 10-240.

Yenier, E., and Atkinson, G. M. (2014). Equivalent point-source modelling of moderate-to-large magnitude earthquakes and associated ground-motion saturation effects. *Bulletin of the Seismological Society of America, 104(3),* 1458-1478.

Yu, G., Anderson, J. G., and Siddharthan, R. (1993). On the characteristics of nonlinear soil response. *Bulletin of the Seismological Society of America*, *83*(1), 218–244.

Zandieh, A., and Pezeshk, S. (2010). Investigation of geometrical spreading and quality factor functions in the New Madrid seismic zone. *Bulletin of the Seismological Society of America*, *100*(5A), 2185-2195.